University of Bergen


Department of Physics and Technology

Master thesis

---

# Performance study of the J/$\psi$ reconstruction after the ALICE LS2 upgrade

---

*Author: Andreas Mikalsen*

*Supervisor: Dieter Röhrich*

*Co-supervisors: Ingrid Mckibben Lofnes and Jon-Are Sætre*

May 31, 2023

# Acknowledgements

I want to thank my supervisor Professor Dieter Röhrich for giving me the opportunity to work in this field of physics. Your courses in data handling and nuclear and particle physics were a large part of why I chose this direction for my thesis. My co-supervisors, Ingrid Mckibben Lofnes and Jon-Are Sætre, thank you for all the time you have spent mentoring me. All of your explanations, advice, and constant feedback have been invaluable. I feel truly honored to have had the privilege of working under the supervision of all three. I am also grateful for the opportunity to be a part of the Norwegian analysis group. The whole year has been a fantastic learning experience.

Thank you to my family for their unwavering support, encouragement, and understanding throughout this endeavor. Thank you to all the fantastic people I have lived with, shared office with, played video games with, and otherwise interacted with for the past 5 years. A special shoutout to DK, EE, EF, JS, KB, KS, OS, and SI for both helping me through my studies and being a huge part of my life. Thank you all!

Andreas Mikalsen

# Abstract

This thesis presents a performance study of the first Run 3 data recorded by ALICE in 2022. The experimental setup of ALICE underwent multiple upgrades during the Long Shutdown 2. The primary motivation behind the upgrades was to handle the large increase in data with better tracking performance, without suffering significant losses in Particle Identification (PID). A small test sample of proton-proton collisions at $\sqrt{s}$ = 13.6 TeV has been studied to assess the new detector's performance. These test samples only contain 1.7e+07 events in total, and there are currently no available Monte Carlo simulations to go along with them. The analysis work was performed using the Run 3 analysis framework $O^2$. J/$\psi$ mesons are used as a probe because of their sensitivity in terms of both PID and momentum resolution. The first signal extractions performed did not show any peaks in the resonance area. This was improved by adding post-calibrations for the PID performance and space charge distortion corrections to the momentum resolution. The J/$\psi$ peaks are now visible, with the characteristic narrow resonance area around 3 GeV/$c^2$, sharp dropoff towards higher masses, and tail distribution towards lower invariant mass. The tracking performance is then studied by analyzing the impact parameter resolution. The measured values are found to be slightly worse than the projected resolution for Run 3 but still a considerable improvement from Run 2.

# Contents

# List of Figures

# Chapter 1

# Strongly interacting matter

The four fundamental forces that govern the universe are called gravity, the weak force, the strong force, and the electromagnetic force. Gravity is responsible for many interactions, such as planets moving in our solar system but is negligible in particle interactions because of how weak it is between small masses. The three remaining forces allow interactions between even the most fundamental particles, called fermions, using exchange bosons. Electromagnetic force affects all particles with an electric charge, such as electrons or quarks. The force is carried using massless photons and is responsible for most interactions between atoms. The weak force interacts with all fermions without dependents on any charge. Instead of massless photons, the weak force interacts through heavy bosons called $W^{\pm}$ and $Z^0$. The high mass of these bosons is why the force is called weak, despite having a similar coupling constant to electromagnetism. This chapter is an introduction to the strong interaction, with a focus on its corresponding strong coupling constant $\alpha_s$. The Quark-Gluon Plasma (QGP) is then introduced together with its role in both the phase diagram of QCD matter and in heavy-ion collisions. At last, the following chapters are outlined together with the motivation behind the thesis work.

## 1.1 Quantum Chromodynamics

Quantum Chromodynamics (QCD) [22] provides a mathematical description of the interactions between colored quarks and gluons, analogous to how Quantum Electrodynamics (QED) describes interactions between charged particles and photons. QCD is a non-Abelian gauge field theory, where the charge is labeled by an index called "color" charge. All quarks are distinguished by their color charge, which can be labeled as red (r), green (g), blue (b), or their corresponding anti-colors. These colored quarks combine in such a way as to produce particles that have no net color charge, which is referred to as color-neutral composite particles. In QCD, every observable particle must be in a color singlet state, meaning that it has no net color charge. This is where the terms "chromo" and "color" originates from. The process of combining both color and anti-color charges, as well as all three possible colors, to produce a color-neutral composite particle is analogous to how paint colors combine on paper to create a new color. For example, the combination of red, blue, and green produces white, while any color with its corresponding anti-color also produces white or a color-neutral state.

Like their QED counterpart photons, the gluons are massless with a spin of 1. However, there are some important differences between QED and QCD. Unlike photons, gluons themself carry both color and anti-color charges in a non-neutral state. From three colors with their respective anti-colors, it is possible to arrange nine different gluon states. The combination $r\bar{r} + b\bar{b} + g\bar{g}$ is color-neutral, known as the color singlet state. While the other eight, the color octet, correspond to different gluon color states. The quarks interact via the exchange of these colored gluons, but since the gluons carry charge, they can also interact with other gluons. This self-interaction leads to a dependence on the distance between the interacting quarks, affecting their interaction's strength. Specifically, the distance is inversely proportional to the momentum transfer $Q^2$. This means that large momentum transfer results in small distances and therefore weaker interactions. At some point, the interactions become so weak that the particles experience what's called asymptotic freedom, behaving as if they didn't interact strongly at all.

The properties of QCD can be described mathematically with the following Lagrangian:

$$\mathcal{L} = \bar{\psi}[i(\gamma^\mu D_\mu) - m]\psi - \frac{1}{4} G^a_{\mu\nu} G^{\mu\nu}_a. \tag{1.1}$$

Here, $\psi$ represents the quark field, $m$ is the quark mass, $D_\mu$ is the covariant derivative which ensures gauge invariance for SU(3) transformations, and $G_{\mu\nu}$ is the gluon field strength tensor and $a$ is the color index. The gluon field strength is given by:

$$G^a_{\mu\nu} = \partial_\mu A^a_\nu - \partial_\nu A^a_\mu + g f^{abc} A^b_\mu A^c_\nu. \tag{1.2}$$

Here, $A^a_\mu$ is the gluon field, $f^{abc}$ is the SU(3) structure constant, and $g$ is the dimensionless coupling constant, also known as $\alpha_s$ for strong interactions.

The strong interaction has the property that the force changes at different distances, meaning the coupling constant is not constant at all [23]. Instead the coupling $\alpha_s$ depends on the momentum transfer $Q^2$ and is given by:

$$\alpha_s(Q^2) = \frac{\alpha_s(\mu^2 c^2)}{1 + \frac{33-2N_f}{12\pi}\alpha_s(\mu^2 c^2) ln(\frac{Q^2}{\mu^2 c^2})}, \tag{1.3}$$

where $\mu$ is the scale mass and $N_f$ represents the number of flavors. For three quark colors and six possible flavors, $\alpha_s$ decreases with $Q^2$. Different from the energy dependence of the QED coupling constant, which slightly increases for increasing momentum transfer. This difference stems from the self-interaction between gluons in QCD, which does not appear between photons in QED. At large momentum transfers $\alpha_s$ becomes small, and it is possible to calculate QCD processes perturbatively.

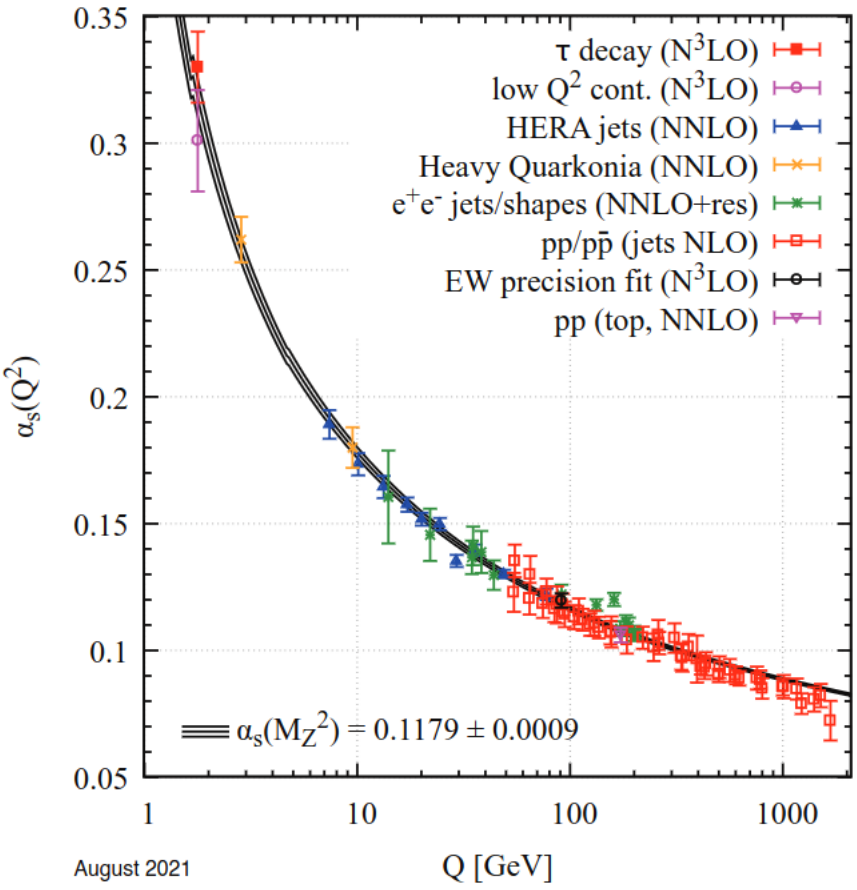


*Figure 1.1: Measurments of the running coupling constant of QCD as a function of the energy scale Q. The number of degrees of perturbation theory used when extracting $\alpha_s$ is indicated in brackets. Next-to-leading order (NLO),next-to-next-to-leading order (NNLO), NNLO with a resummed calculation (NNLO+res), and next-to-NNLO (NN$^3$LO)[1].*

The Cornell potential gives the potential energy for a bound system of heavy quarks in QCD [24]:

$$V = -\frac{4}{3}\frac{\alpha_s}{r} + \sigma r, \tag{1.4}$$

where $r$ is the distance between quarks, $\alpha_s$ is the running coupling in QCD and $\sigma$ is the QCD string tension. When increasing the distance, the linear term grows and becomes dominant. This term gives origin to the confinement of quarks into color singlet states. The force between the quarks as they are moved apart resembles a rubber band, increasing proportionally to the distance. When the quarks are moved far apart, their potential energy becomes sufficient to create a new quark pair, combining with the original quarks into new hardons. This process called fragmentation explains why there are no free quarks and is shown in figure 1.2.

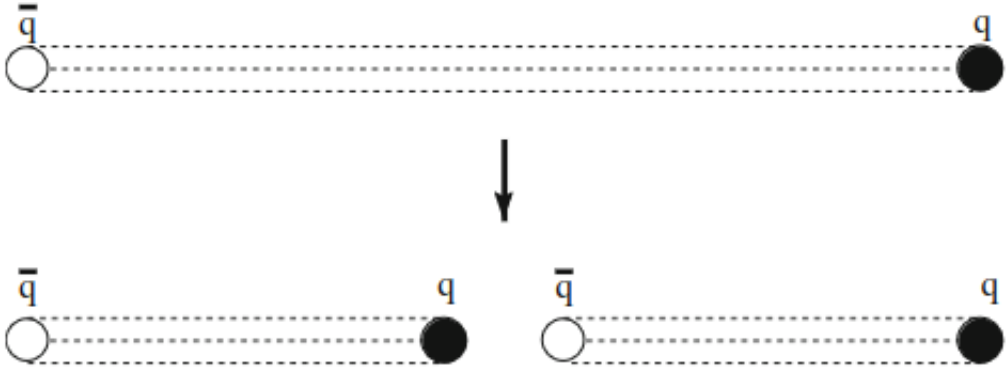


*Figure 1.2: Figure shows two quarks at a sufficient distance where the potential energy between them is enough to create a new quark pair which then hadronizes with the original quarks into new quark pairs. This process makes it impossible to separate a quark from its bound state [2].*

On the other hand, it was realized that as the quarks move incredibly close to each other, they behave in a quasi-free manner. At this range, they experience asymptotic freedom. Figure 1.1 shows how this occurs due to the vanishing coupling constant at very high momentum transfer.

## 1.2 Quark-Gluon Plasma

The idea of asymptotic freedom leads to the possibility of a new deconfined phase of matter called Quark-Gluon Plasma (QGP) [4]. This state is characterized by its extreme temperature and density, where quarks and gluons behave as quasi-free particles. Studying such systems gives a unique possibility to gain insight into the strong interaction. "QCD condensed matter" can be produced from extreme energy density, currently only achievable in heavy-ion collisions. A system with zero baryon density require temperatures exceeding 150-160 MeV or roughly $10^{12}$ K before transitioning into QGP. It is believed that at the beginning of the universe, for approximately ten picoseconds after the big bang, the universe consisted entirely of this phase of matter. Because of the short lifetime of the QGP, it is impossible to detect directly. Instead, different indirect observables are examined to determine whether or not the creation of QGP occurred. One of these observables is the suppression (and regeneration) of quarkonium states such as the J/$\psi$, which will be discussed further in section 2.3.

### 1.2.1 Phases of QCD matter

The QGP can be reached at very high temperatures and/or pressure. This is the equivalent of increasing the energy and decreasing the distance between the constituents. The phase diagram shown on the right side of figure 1.3 shows a sketch of how the matter transitions for different temperatures and pressures. While the baryon-chemical potential $\mu_B$ is not the same as pressure, it indicates the imbalance between particles and antiparticles and can be related to pressure through the net baryon density. The normal atomic nucleus exists at low temperatures and at pressures around $\mu_B = 1$. The solid lines indicate transition values between states through a first-order phase transition,

while the dashed line indicates the crossover region. At the intersection between the crossover transition and first-order phase transition, there might exist a critical point that would be analogous with the triple point in the phase diagram of water, marked with a black dot on the left side of figure 1.3. The early universe state of extreme temperatures and vanishing baryon density is also indicated with an arrow. The last state shown, called color superconductivity, occurs at low temperatures and very high baryon density. As the name suggests, it is analogous to the superconductivity in electromagnetism. This phase state might exist inside neutron stars where gravitational pressure increases the density so much that the color charges are deconfined.

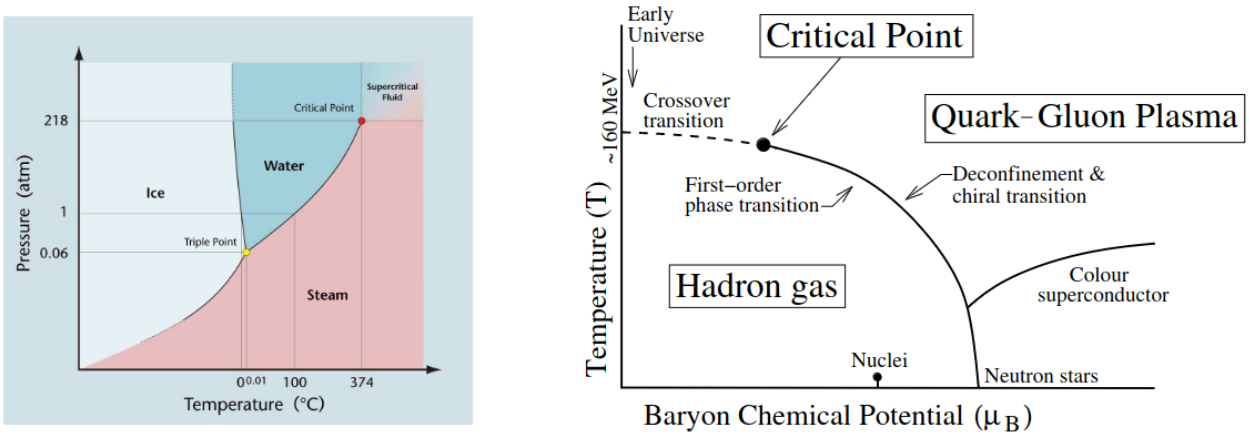


*Figure 1.3: Left shows the phase diagram of water, and right shows the phase diagram of QCD. On the QCD phase diagram is the atomic nucleus existing at low temperatures and $\mu_B$ around 1, marked with a small black dot. Solid lines indicate transition values for first-order phase transitions between states, while dashed lines indicate transition regions. The intersection where the lines meet is marked with a black dot indicating a critical point similar to the triple point for water [3].*

Predictions about phase transitions are a complicated problem. Studying the full QCD is necessary since both equilibrium and phase transitions involve long-distance scales for quark and gluon interactions, meaning a region where it is not possible to use perturbative calculations. Instead, a method to perform calculations on a lattice has been created. Lattice QCD defines quarks at lattice sites with gluons connecting them as links. Space-time is discretized on the lattice with finite size. Since this method works on non-perturbative problems, it is well suited to study partonic systems such as the QGP. Estimating thermodynamic properties with lattice QCD requires a lot of computational power. With calculations done assuming vanishing baryon chemical potential and employing so-called (2+1) flavored QCD with realistic mass values for up, down, and strange quarks, it is possible to find the temperature dependence of quantities such as pressure, energy, or entropy [25]. These values describe the equation of state for a given quantum system and are found to evolve into a deconfined state when the temperature surpasses roughly 155 MeV. This transition into a deconfined state is still an active field of research.

### 1.2.2 Evolution of heavy-ion collisions

The Quark-Gluon Plasma can be created in laboratories from heavy-ion collisions. These collisions can be described as a series of stages.

First, the initial state, where projectiles defined by their respective wave functions collide. These nuclei will be very Lorentz contracted as indicated in figure 1.4. The distance between the center of colliding nuclei is called the impact parameter $b$. The amount of nuclei participating in the interaction is labeled $N_{\text{part}}$ while the number of binary collisions is $N_{\text{coll}}$. These values are related so that if $b$ is small, $N_{\text{part}}$ and $N_{\text{coll}}$ will be large.

After the collision, the system enters a pre-equilibrium phase. Multiple hard scatterings take place between partons from incoming nuclei. This is the stage where different high-momentum particles and heavy quarks get created. Particles created in this stage can be studied as probes of the QGP phase.

The system evolves towards thermal equilibrium as a result of rescattering among the partons. If the energy density and therefore temperature of the system surpass the critical values, it forms a QGP.

The QGP expands from the pressure of the system relative to the surrounding vacuum. The expansion reduces the energy density of the system, meaning the system will reach a temperature where the nuclear matter is no longer deconfined. Quarks and gluons start forming hadrons, but exactly how these hadrons are formed is not well known.

The hadrons still interact elastically, expanding the matter further. The matter now consists only of hadrons which only stop scattering when the particles are too far away from each other to interact. At this point, the system has reached freeze out meaning that the hadrons decouple with fixed momenta. These hadrons can be detected in experiments such as ALICE, further described in chapter 3.2. Further reading on the evolution of collisions can be found here [26].

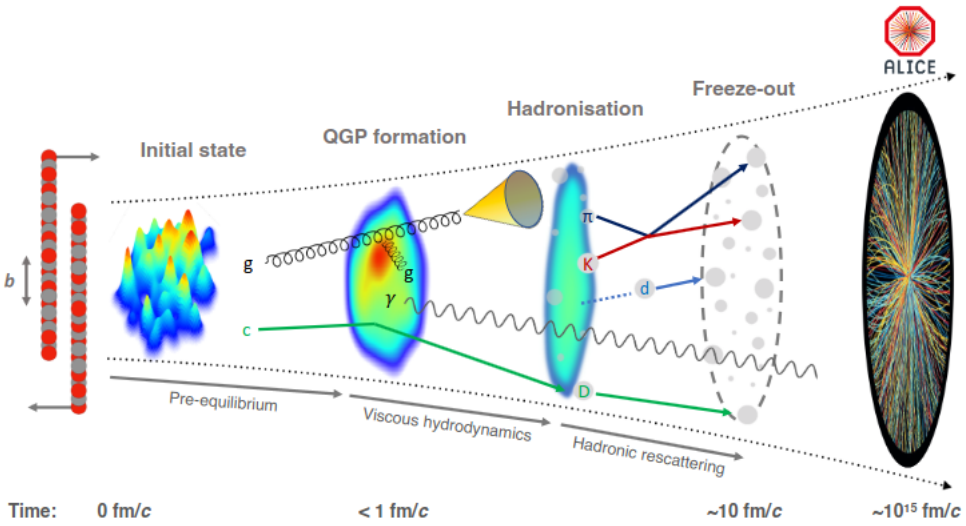


*Figure 1.4: The evolution of heavy-ion collision. Starting from nuclei in a Lorentz contracted initial state on the left. After collision heavy quarks are formed and if the temperature is above the threshold QGP can form. The expansion of the system cools it down below the deconfinement threshold and hadronization occurs, eventually, the entire system is hadrons. When the distance between hadrons is large enough they are deconfined from the system with fixed momentum, the system reaches freeze out and the hadrons can be detected in detectors such as ALICE [4].*

.

## 1.3 Outline of the thesis

This thesis is a part of the early quality analysis of Run 3 data produced by the ALICE detector from the research group at CERN. The experimental setup of ALICE underwent upgrades during the Long Shutdown 2 to match the increased performance of the LHC. The upgrade purpose is for ALICE to handle more data with a better tracking resolution while maintaining its previous Particle Identification (PID) capabilities. The most relevant upgraded components for this thesis are listed below.

- The Inner Tracking System (ITS) now consists of seven-pixel layers which improve tracking and momentum performance, at the cost of no longer performing PID in the ITS.
- The Time Projection Chamber (TPC) now uses Gas Electron Multiplier (GEM) technology as it allows for continuous readout of data without the dead time which limited the old gating grid system when handling large amounts of data quickly.
- The Online-Offline ($O^2$) framework handles both the online data readout and the following offline data processing. It is both able to store the increased amount of data that is recorded during Run 3 efficiently and is also the analysis framework used in this thesis.

This thesis will focus on signal extraction and impact parameter studies as benchmarks to investigate if there are improvements in tracking performance and proper handling

of increased data. The available datasets that have been used are small parts of the total data, they only contain proton-proton collisions, and there are currently no Monte Carlo (MC) simulations available.

The production of quarkonium or J/$\psi$ in particular plays an important role in the study of QCD, as it can be used to probe QGP. The J/$\psi$ decaying through the lepton channel has a clear signal peak. For this reason, the J/$\psi$ was chosen as a good candidate for the performance studies in this thesis. The J/$\psi$ signal will be extracted and the resonance peaks compared to Run 2 data and used as an indicator of the data quality and detector performance.

Chapter 2 discusses the production mechanism of quarkonia, which are bound states of heavy quark and anti-quark pairs. Several models describing the production mechanism are presented. These models provide an interesting interplay between perturbative and nonperturbative calculations. A further explanation of the importance of the J/$\psi$ meson and its role in QGP studies is also provided. In chapter 3 the ALICE detector is described, with a focus on detailing the upgrades made during the shutdown between Run 2 and Run 3. The mechanisms to determine particle tracks and to perform Particle Identification (PID) are also introduced. Chapter 4 describes the analysis framework used, the available datasets, the cuts applied to remove low-quality or unwanted tracks, and the process of determining the background in signal extraction. The signal extraction process is then done in chapter 5 with a focus on the improvements in post-calibrations and corrections performed on the data. An early look at impact parameter studies is shown, with a focus on the obtained resolution as this is a good indicator of the tracking performance. The sixth and final chapter reviews the performance results while providing a discussion on future prospects, both for similar analysis and ALICE in general.

# Chapter 2

# Quarkonia

Bound states of a quark and an anti-quark where the quark mass surpasses the QCD scale $\Lambda_{QCD} \sim 255$ MeV [27] are called quarkonia. The QCD scale, or the renormalization scale of QCD, determines roughly when the coupling constant becomes large. The three heaviest quarks, charm, bottom, and top, with masses $m_c = 1.27\ GeV/c^2$, $m_b = 4.18\ GeV/c^2$ and $m_t = 172.9\ GeV/c^2$ respectively, all fulfill this condition. However, due to the extremely high mass of the top quark, the lifetime is smaller than the hadronization time, meaning no $t\bar{t}$ pairs are found. Therefore quarkonia consist of bound $c\bar{c}$ and $b\bar{b}$ states, referred to as charmonium and bottomonium, respectively. One difference between quarkonium and light flavor hadrons such as protons is where its mass originates from. The proton mass is mainly attributed to the binding energy in the system, while the quarkonium mass dominantly comes from the heavy quark masses themself. The Cornell potential given by equation 1.4 can be used to predict the mass spectrum of the different states of quarkonium. The mass spectrums of charmonium and bottominum are shown in 2.1 and 2.2, respectively.

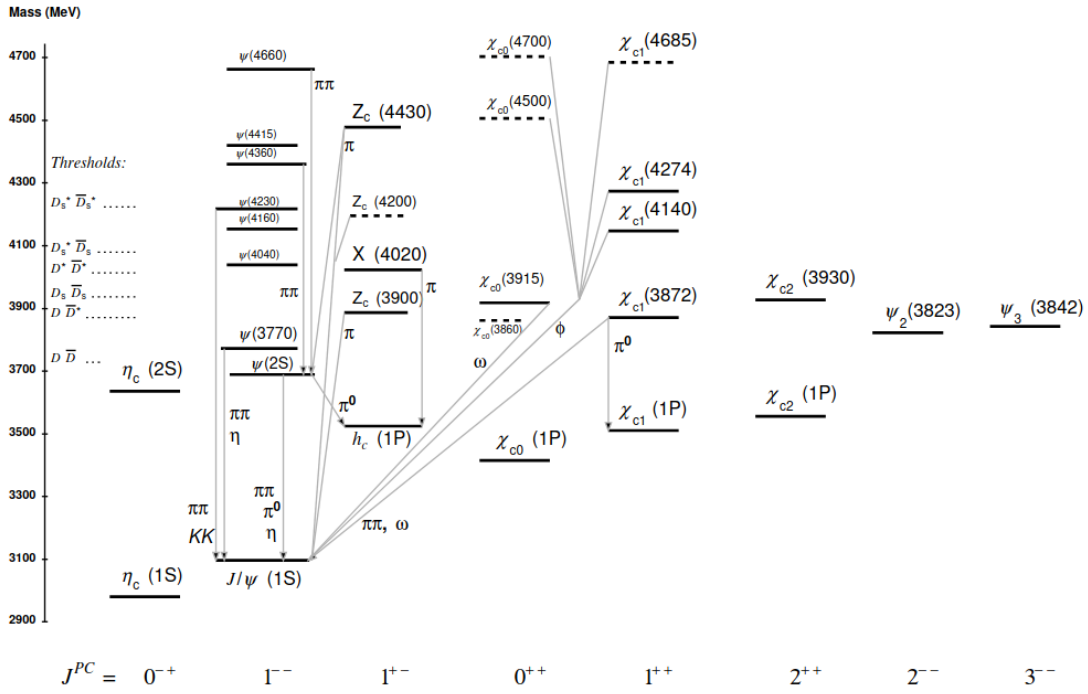


*Figure 2.1: The mass spectrum of bound $c\bar{c}$ experimentally established [1].*

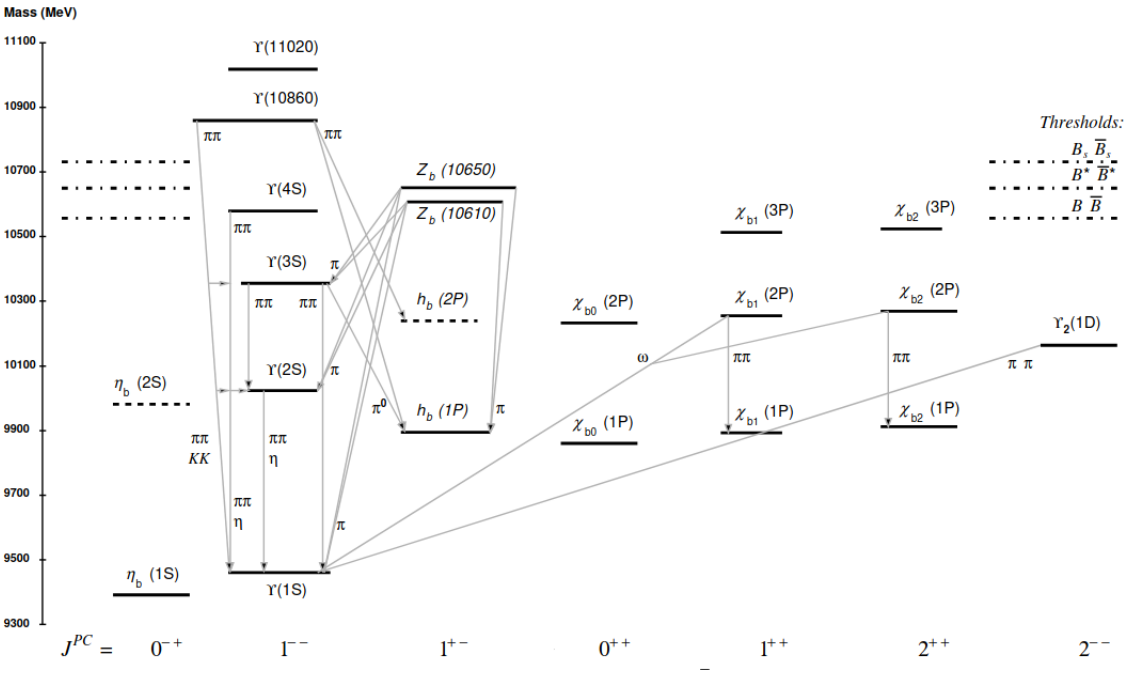


*Figure 2.2: The mass spectrum of bound $b\bar{b}$ experimentally established [1].*

## 2.1 The J/$\psi$ meson

The first charmonium state was independently discovered by research groups from Brookhaven National Laboratory [28] and SLAC-Berkely [29] in November 1974. The state is named J/$\psi$ and with a mass of $m$ = 3096.9 MeV/$c^2$ and lifetime of $\tau = 7.2 \times 10^{-21}$ s [1]. Figure 2.1 shows that the J/$\psi$ meson is charmonium ground state of spin-1 with odd parity and charge parity, allowing for leptonic decays. The narrow decay width ($\Gamma = 92.9 \pm 2.8$ KeV [1]) is a result of suppression of decay through the strong interaction. First, the mass of J/$\psi$ is below the threshold for strong decay into mesons pairs consisting of Charm and lighter quarks combinations such as D-mesons. This means the only option is decay through $c\bar{c}$ annihilation. The J/$\psi$ and all other color singlet states can't decay through a single gluon because of color conservation. Further, conservation of parity requires an odd number of gluons meaning the first possible decay channel is through three gluons. A large portion of J/$\psi$ decays, therefore, happens through electromagnetic interactions, which is significantly weaker than the strong interaction, providing a much longer lifetime for its heavy mass.

It is normal to divide J/$\psi$ into two categories based on their production channel. Prompt J/$\psi$ is produced directly during the initial scattering or from the decay of higher-state charmonium. Non-prompt J/$\psi$ refers to J/$\psi$ produced from the weak decay of hadrons containing bottom quarks, often called b-hadrons. This means that during collision experiments, the production vertex for non-prompt J/$\psi$ is different from the primary vertex of the collision where prompt J/$\psi$ is produced. When talking about both categories simultaneously, they are typically called inclusive J/$\psi$. These distinctions are made because of the different theoretical models used to predict the production rate of prompt J/$\psi$, which can not be used to describe non-prompt J/$\psi$. On the other hand, modeling the decay of b-hadrons can be used for non-prompt J/$\psi$ production.

## 2.2 Quarkonia production

The description of quarkonia production requires the interplay of both perturbative and non-perturbative QCD calculations. Therefore the process is divided into two steps. First the production of two quarks, then the evolution into a bound state. Initial heavy quarks are primarily produced at a perturbative momentum scale $p$, defined by large momentum transfer $Q^2$. At TeV energies such as at the LHC, gluon fusion is the typical mechanism behind $c\bar{c}$ production, i.e., $gg \rightarrow c\bar{c}$. This is because, in this Bjorken x range, the gluon Parton Distribution Function (PDF) dominates. While gluon fusion is the Leading Order (LO) process, charm production also gets an important contribution from Next to Leading Order (NLO) $gg \rightarrow gg$ processes. An example of both processes is shown in figure 2.3.

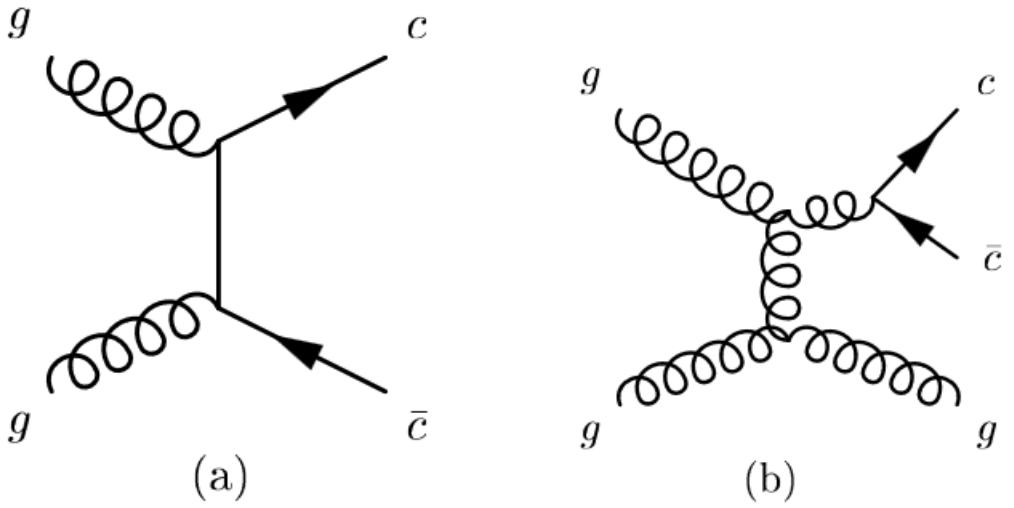


*Figure 2.3: Illustration of a) leading order and b) next to leading order $c\bar{c}$ production [5].*

The proceeding evolution into a bound state requires that the quark pair travels at a relatively low momentum compared to the quark mass. If the momentum is too high, the quarks won't be able to interact with each other, and as a result, perturbative methods can't be used to fully explain production models. Figure 2.4 shows an example of quarkonium production. The collision between two partons with a given parton distribution function (PDF) creates a heavy quark pair during the collision, which can be calculated perturbatively. Next, the quark pair evolution into a bound state H can be described by different models, here represented by non-relativistic QCD (NRQCD) factorization.

Explaining quarkonia production with this intuitive picture requires that it is actually possible to separate the perturbative and non-perturbative calculations completely. This separation, called "factorization, " is performed by expressing the amplitude or cross-section as a sum of products of short-distance coefficients with long-distance operator matrix elements [30]. The matrix elements contain non-perturbative physics and can only be determined phenomenologically or through lattice simulations. There are different models describing the evolution from a pair of quarks into a bound color-singlet system. The most notable are the Color-Singlet Model (CSM), the Color-Evaporation Model (CEM), and the earlier-mentioned NRQCD factorization. They are introduced in the following subsections, and an overview can be found in [30].

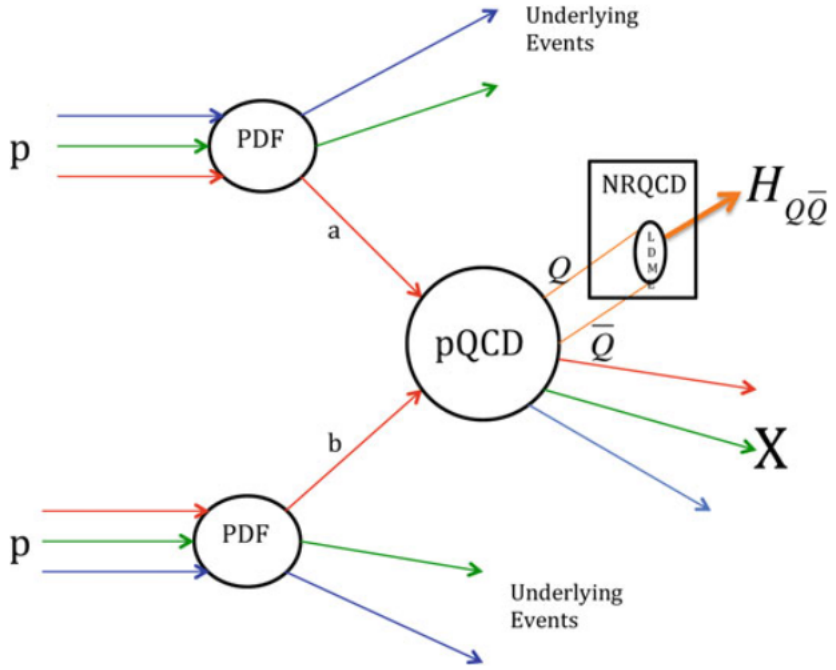


*Figure 2.4: Sketch of quarkonium production. Partons a and b collide with enough momentum to produce quark pair $Q\overline{Q}$, which then evolves into bound state H. This evolution can be described using different models, here represented by NRQCD [6].*

### 2.2.1 The Color Evaporation Model

The CEM [31–33] model assumes that the cross-section for quarkonium production must be proportional to the cross-section of the quark-antiquark pair it consists of. Every quark pair will then evolve into some bound quarkonium state if the pair is below the threshold required to produce any other open flavor mesons. The probability of producing a specific quarkonium state is assumed to be independent of the original $Q\overline{Q}$ pairs color charges and not required to be in a color-singlet state. Instead, the color and spin are randomized from various soft interactions that occur after production and are unrelated to the quantum numbers at the moment of creation.

The probability for a quark pair to eventually end in a color-singlet state is 1/9, the total cross section is therefore given as in [31]:

$$\sigma_{onium} = \frac{1}{9}\int_{2m_Q}^{2m_{\bar{q}Q}} dm \frac{d\sigma_{Q\overline{Q}}}{dm}. \tag{2.1}$$

The total cross section is found by integrating between twice the quark mass up to twice the open flavor threshold. The probability for a given quarkonium state $H$ to be produced is assumed to be a given constant $f_H$.

$$\sigma_H = f_H \sigma_{onium}. \tag{2.2}$$

The constant $f_H$ is found from experimental data and is independent of the production process, energy, and momentum. This means the model cannot explain the observed

variation for different processes for charmonium state production since said probability only depends on quarkonium type. Figure 2.5 shows the comparison between predicted values from CEM and the cross-section measured for inclusive J/$\psi$ at ALICE [7].

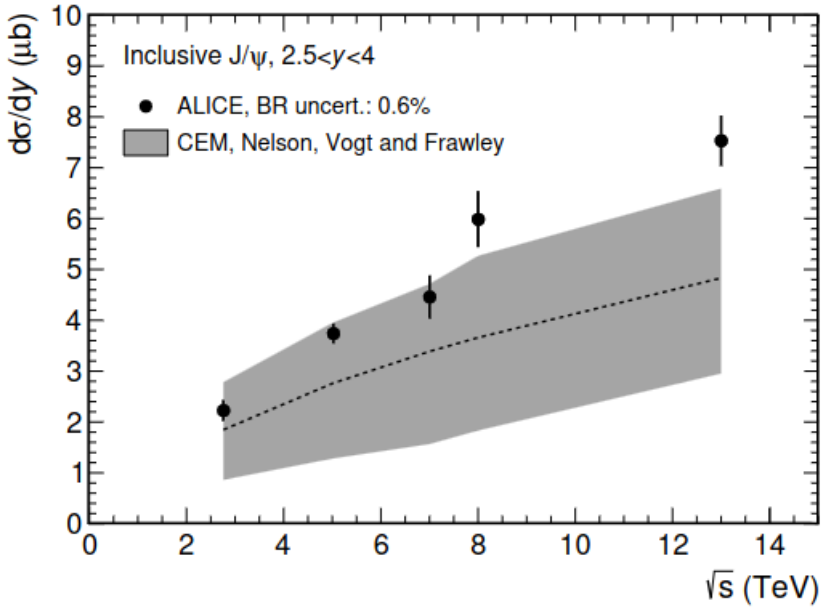


*Figure 2.5: Energy dependence of cross-section for the production of inclusive J/$\psi$ measured by ALICE versus data predicted by the CEM model from [7].*

### 2.2.2 The Color-Singlet Model

The CMS [34; 35] model assumes that the initial quark pair does not change the color quantum numbers during its transition into a bound quark system. In the end, the bound quarkonium must be in a color singlet state, meaning the initial quark pair must also be in a color singlet state. The same is true for the quantum numbers for the spin and angular momentum of the emerging quarkonium.

The production rate of any quarkonium state depends on the absolute value of the wave function of the quark pair and its derivatives, evaluated by assuming a vanishing distance between the quarks. These quantities are found by comparing with experimental measurements, which leaves the model without free parameters. Evaluation of the model at a certain energy level still gives the model predictive power at other energy levels.

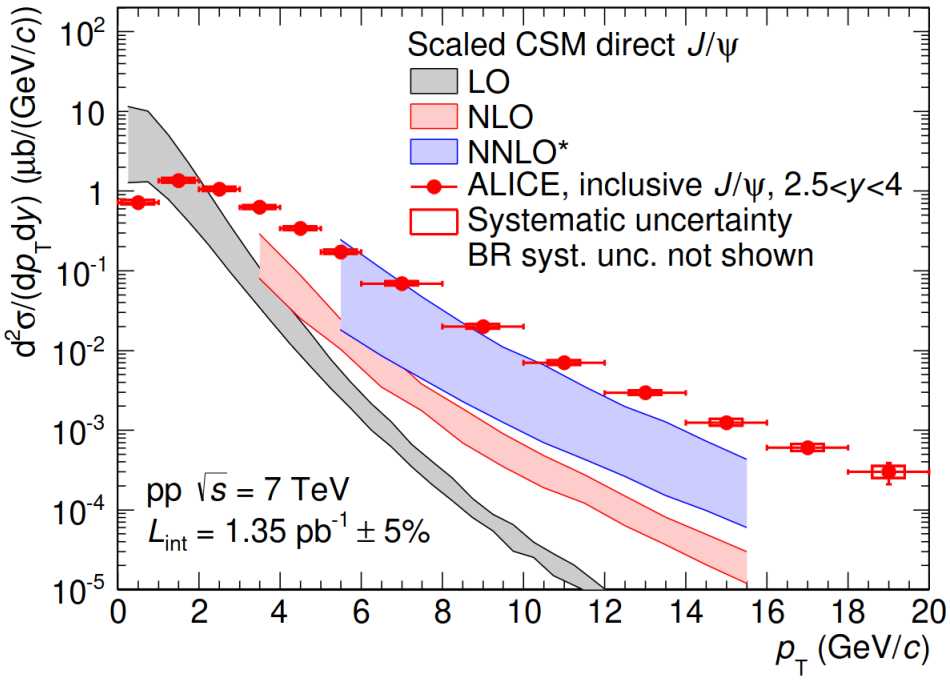


*Figure 2.6: Cross-section of J/ψ production calculated as a function of transverse momentum for proton-proton collisions at $\sqrt{s}$ = 7 TeV. Data is taken by ALICE, compared with predictions made from the Color Singlet Model at leading order (LO), next-to-leading order (NLO), and with next-to-next-to-leading-order contributions (NNLO*) [8] .*

At low collision energies, the predicted cross-section from the CMS model aligns reasonably well with measured data. Still, it underestimates the measured production more and more as the energy increases [36]. Figure 2.6 shows a comparison between the predicted production cross section against ALICE data measured at $\sqrt{s} = 7$ TeV. Including higher-order expansions of $\alpha_s$ to the leading order predictions introduce corrections in the form of next-to-leading order (NLO) and next-to-next-to-leading order (NNLO), which is in better agreement with measured data. Still, the model fails to describe the experimental values fully, and the improvements lead to an increase in theoretical uncertainties and/or more parameters that must be fitted to the data. It should also be noted that figure 2.6 shows directly produced J/$\psi$, which have been scaled to inclusive production channel data.

### 2.2.3 The NRQCD factorization approach

The most effective model to describe quarkonium production is the Non-Relativistic QCD (NRQCD) factorization approach [37; 38]. Where the CSM only considers quark pairs in an already color-singlet state, NRQCD also allows for a color-octet state. Since this increases the number of initial states considered, the model predicts a higher amount of production. This also means that any quark-antiquark pair that initially exists in a color-octet state must radiate gluons until they are color neutral for it to be possible to form a bound state between them. This radiation might be detectable in the form of angular correction of J/$\psi$ mesons or hadrons occurring during the hadronization of said gluons. In NRQCD, the heavy quark mass means that the evolution into a

bound state is treated non-relativistically, with a finite ultra-violet cutoff for the mass of the heavy quark that excludes relativistic states.

The model considers three different highly relevant energy scales. The heavy quark mass $m$, its momentum $Mv$, and its energy inside the quarkonium $Mv^2$. The probability that a quark pair evolves into quarkonium can be expressed using the matrix elements of the NRQCD operators. The infinite number of possible matrix elements can be limited by expanding in terms of the heavy quark velocity $v$, shortening the series for some fixed order of $v$. The remaining matrix elements can then be fixed around experimental data. This means that the total NRQCD cross-section becomes an expansion around both the strong coupling constant $\alpha_s$ and the heavy quark velocity $v$. The production cross-section for a given quarkonium state $H$ can be expressed using the sum of the remaining matrix elements:

$$\sigma(H) = \sum_n \sigma_n(\Lambda)\langle \mathcal{O}_n^H(\Lambda)\rangle. \tag{2.3}$$

Here, $\Lambda$ represents the earlier mentioned ultra-violet cutoff of the theory, and $\sigma_n$ represents the cross-section of the heavy quark pair production with an expansion in $v$. The remaining element $\langle \mathcal{O}_n^H(\Lambda)\rangle$ describes the following transition into the given bound quarkonium state $H$ using the NRQCD long-distance matrix elements. The summation is here performed for the quantum numbers color, spin, and orbital-angular momentum $n$ of the initial pair. When the NRQCD approach is used on only color-singlet states and $v$ is shortened around LO, the model simplifies into the CSM.

The long-distance matrix elements given by $\langle \mathcal{O}_n^H(\Lambda)\rangle$ can be fixed using fits to experimental data. These matrixes are assumed to be universal, but it is unknown if this will hold true. The model's predictive power is also limited by how valid the shortening of the matrix series around $v$ truly is. Since the $\sigma_n$ only consists partly of short-distance quantities, it is unknown how valid the perturbative calculations are for the quark pair cross-section. Still, NRQCD has proven itself more able to predict experimental data when compared with both CSM and CEM.

When comparing the model with ALICE data measurements, both prompt and non-prompt J/$\psi$ are taken into account. In the left panel of figure 2.7, the three different calculations that are used is prompt J/$\psi$ predictions from Next-to-Leading-Order NRQCD in gray, Leading Order NRQCD with a Color Glass Condensate (CGC) employed to calculate at a lower $p_{\mathrm{T}}$ is shown in blue and calculations of non-prompt J/$\psi$ from a Fixed-order-next-to-leading Logarithm (FONLL) is shown in red. The right panel shows the predicted inclusive J/$\psi$ production cross section as a combination of NRQCD and FONLL predictions.

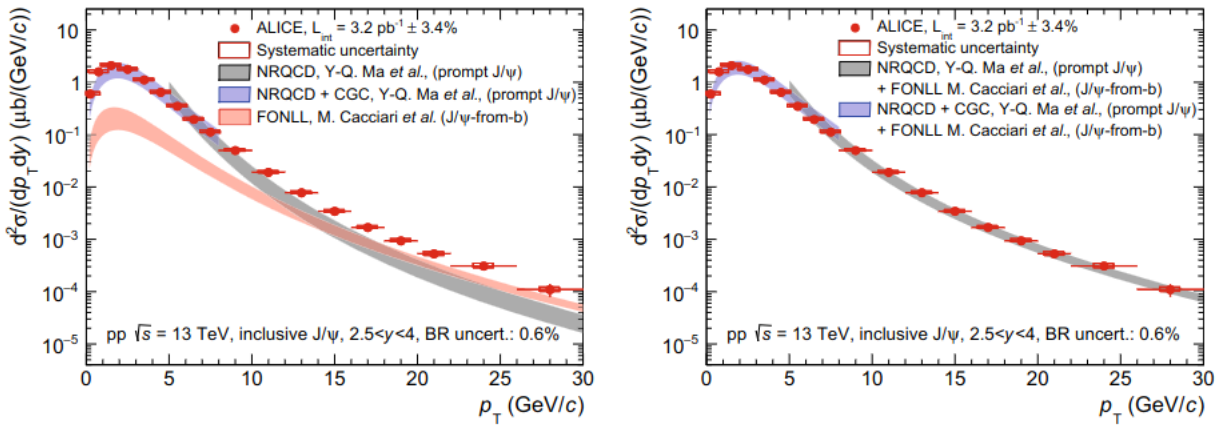


*Figure 2.7: Left panel shows predictions for J/ψ cross section calculated using NLO NRQCD in grey(prompt), LO NRQCD coupled with CGC in blue (prompt), and FONLL in red (non-prompt) against inclusive J/ψ data from pp collisions at $\sqrt{s}$ = 13 TeV. The right panel shows summed calculations of prompt and non-prompt J/ψ compared to the same data [8].*

## 2.3 Probing the Quark Gluon Plasma

While the production mechanism of J/ψ and other quarkonia is an important testing tool for QCD, it can also be used to probe the QGP. Heavy quark production requires a large momentum transfer which is only achieved during the initial stages of the collision. As these produced quarkonium states are affected by the strong force, they will experience the complete evolution of the system and interact with it. The idea that quarkonia yield is modified by some color screening effect, similar to Debye screening in plasma affecting electromagnetic fields, was proposed by Matsui and Satz in 1986 [39]. They suggested that the high density of free color charges would break up bound quark pair states, which would result in fewer quarkonia states. The varying degrees of suppression observed in different quarkonium states can be indicative of the medium's temperature as it relates to the distinct sizes of these bound states [40; 41]. This phenomenon, known as sequential suppression or melting, involves less tightly bound quarkonia disappearing at lower temperatures. Due to the sensitivity of this melting process to the system's temperature, it can serve as a thermometer for the medium.

Amongst all the different quarkonia, J/ψ is the most prominent probe used in QGP suppression studies because of its relative abundance and tight bound state. Experimental data has revealed that in addition to suppression, J/ψ also exhibits signs of regeneration when transitioning from lower energy collisions, such as those at RHIC with gold ions at center-of-mass energies per nucleon pair of up to 200 GeV, to higher energies at the LHC. During the process of chemical freezeout, quarks possess the capability to combine randomly with adjacent quarks. In a hotter medium, the abundance of heavy quarks in the deconfined matter rises, thereby increasing the likelihood of statistical recombination resulting in the formation of quarkonium states. An augmentation of quarkonium production was observed when comparing the cross section at LHC to RHIC energies. This enhancement was attributed to the additional charmonium production via statistical production at the boundary between phases or through the merging

of heavy quarks in the plasma.

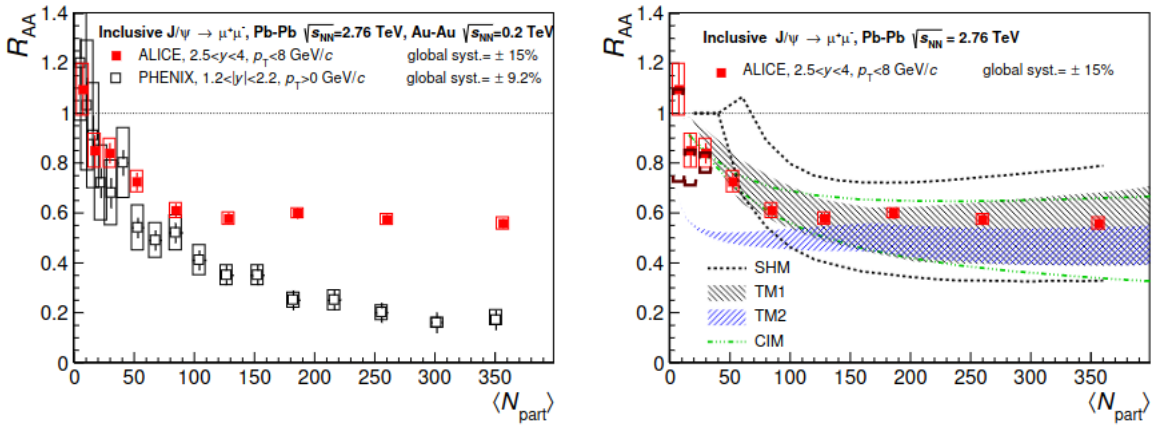


*Figure 2.8: Left shows J/ψ production ratio between heavy-ion and proton-proton collisions ($R_{AA}$) as a function of event multiplicity in ALICE and PHENIX. The right side shows the ALICE data against different model predictions [9].*

In figure 2.8, the left panel compares data from the Pioneering High Energy Nuclear Interaction eXperiment (PHENIX) at RHIC and ALICE at LHC. The nuclear modification factor $R_{AA}$ is defined from the ratio of production yields between heavy-ion and proton-proton collisions. Here the production ratio of J/ψ is plotted as a function of the number of nucleons involved in the collision. A larger number of participants will in general produce higher event multiplicities. Both LHC and RHIC data show J/ψ suppression in heavy-ion collisions from color screening. However, the observed suppression at LHC is smaller when compared with data from RHIC. This comes from the larger amount of charm-anticharm production in higher energy collisions, which results in a higher statistical chance of recombination. The recombination effect helps offset the suppression from the medium and helps explain why the suppression increases with event multiplicity at RHIC but levels off at LHC.

The right side of figure 2.8 compares the same ALICE data with theoretical models. The models shown are a Statistical Hadronization Model (SHM) [42], two Transport Models (TM1, TM2) [43; 44], and the Comover Interaction Model (CIM) [45]. SHM assumes that the system is deconfined, in thermal equilibrium, and that hadronization will occur on a statistical basis at the phase boundary of the QGP. Both transport models are based on transporting the quarkonia through a deconfined system, with the difference coming from the equations used to calculate the rate of suppression and recombination of J/ψ. The last model CIM assumes that the quarks exhibit coherent motion within the partonic medium. All models take recombination into account to some degree, describe the suppression of J/ψ due to interacting with quasi-free color charges in some way, and all are in reasonably good agreement with the ALICE data. A more in-depth discussion of the models in the corresponding references and the comparison to data is discussed in the reference. Without diving deeper into the different models, it shows that J/ψ can be used as a smoking gun signature of the deconfined state.

# Chapter 3

# Experimental setup

## 3.1 The Large Hadron Collider

The Large Hadron Collider (LHC) [46] is a state-of-the-art particle accelerator currently considered the most powerful in the world. After undergoing upgrades and maintenance, it has recently resumed its operation. The LHC is a circular loop spanning a distance of 27 kilometers, buried underground at the border of France and Switzerland. Within the LHC, beams of protons travel in opposite directions and collide at energies as high as 13.6 trillion electron volts (TeV) in four distinct locations, where advanced detectors are precisely positioned for specific purposes.

The protons in the LHC are guided by a strong magnetic field, which is generated by superconducting electromagnets. These magnets are a significant limiting factor for increasing the energy of the particle beams, requiring extremely low temperatures of 1.9 K to maintain superconductivity. Even a small amount of energy escaping into the magnets can cause them to warm up, resulting in the loss of superconductivity in a phenomenon known as a quench.

To ensure the proper functioning of the superconducting magnets, they must undergo a training process before use. This involves slowly increasing the current in the magnet until it quenches and then restarting the process. Over time, the magnet becomes capable of handling higher currents. However, attempting to retrain the magnets to reach the maximum energy levels achieved in the past would be time-consuming and impractical. Instead, the magnets are trained to a lower energy level, higher than their previous level but lower than the maximum energy achieved. All magnets in the LHC have been trained up to 14 TeV, but retraining them to reach that level again would require a significant amount of time, which could impede research efforts [47]. The LHC, together with the different detectors, underwent maintenance and upgrades for the second time in its lifetime. The third data-taking period, named Run 3, started in July 2022 after the Long Shutdown 2. The LHC will now run for four more years with a central collision energy of 13.6 trillion electronvolts (TeV).

High-energy collisions enable the production of particles that are typically not observed in free space. This is possible thanks to Einstein's equation, $E = mc^2$, which describes the interchangeability of energy and mass. However, merely having the required en-

ergy for particle production is insufficient for observation. The probability of a particular particle production occurring is measured by its cross-section, expressed in units of barns. Some particle productions have extremely low cross-sections, such as the Higgs boson, which is in the order of one billionth of a barn.

Luminosity measures the number of particles passing through a given area over a given time period [48]. However, these particles are not guaranteed to collide, and higher luminosity simply implies that more particles are in a position to do so. The rate at which a particular process is anticipated to occur can be estimated by multiplying the luminosity with the cross-section of that process.

The protons in the LHC are not transported as a continuous beam but are rather bunched together. The luminosity is therefore determined by the number of bunches interacting per second and the number of protons in each bunch. Currently, bunches collide at a rate of 40 MHz, or every $25 \times 10^{-9}$ seconds, with each bunch containing $1.8 \times 10^{11}$ protons. The goal for the end of Run 3 is to achieve $2.3 \times 10^{11}$ protons per bunch [49].

The Large Hadron Collider (LHC) features four distinct locations where advanced detectors with specific purposes are situated, namely ALICE, ATLAS, CMS, and LHCb. Figure 3.1 illustrates their relative locations.

A Toroidal LHC Apparatus (ATLAS) [50] and the Compact Muon Solenoid (CMS) [51] are general-purpose detectors designed with slightly different technical solutions and magnet systems. They are constructed to investigate rare processes and possess the ability to handle high luminosity and cover a large phase space.

LHC beauty experiment (LHCb) [52] is a dedicated detector for heavy flavor physics. Running at lower luminosity, LHCb examines CP violations that occur in heavy flavor hadron decays.

The final detector, A Large Ion Collider Experiment (ALICE) [53], focuses on heavy-ion collisions and warrants further discussion compared to the other detectors.

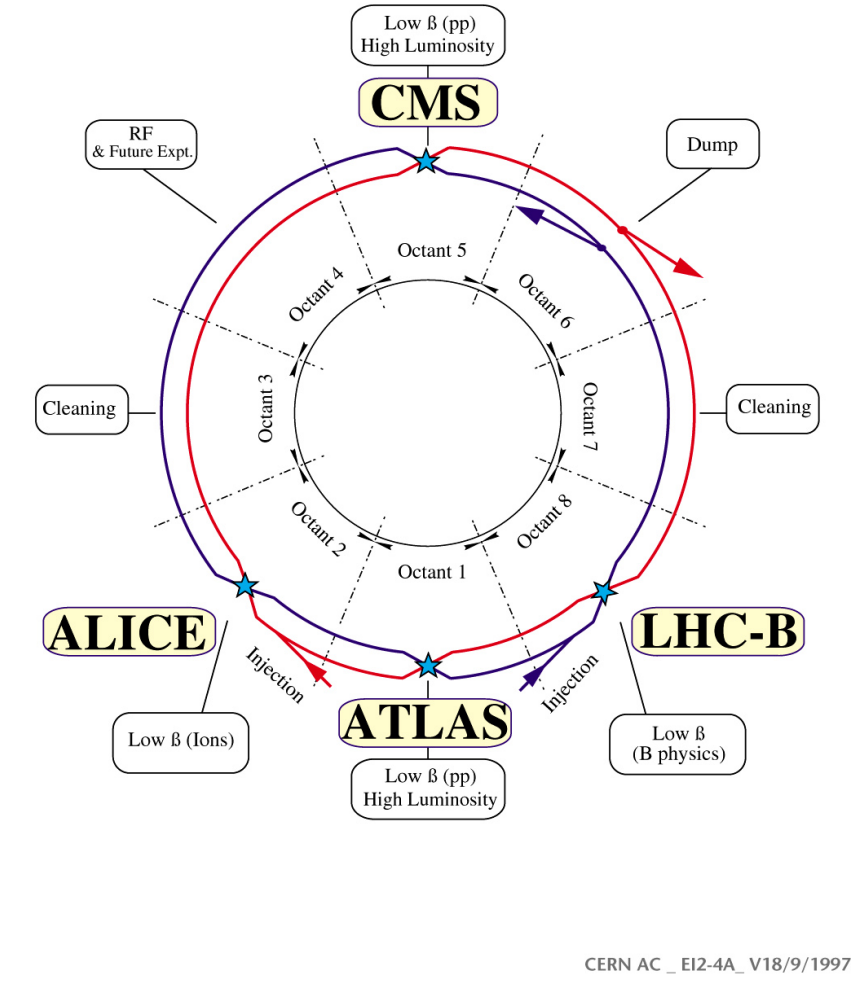


*Figure 3.1: An overview of the LHC layout [10].*

## 3.2 ALICE

A Large Ion Collider Experiment (ALICE) is designed to investigate the physics of strongly interacting matter, with a particular focus on Quark-Gluon Plasma (QGP), through collisions of protons, nuclei, and heavy ions accelerated in the LHC. Low-momentum particles such as heavy-flavor hadrons, low-mass dileptons, and quarkonia are measured in these collisions. Measurements in Pb-Pb data often have a low signal-to-background ratio, necessitating large amounts of statistics and un-triggered running (minimum-bias data).

In order to keep up with the increase in performance from LHC during run 3, the ALICE experiment also underwent upgrades during the Long Shutdown 2 (LS2). The upgrades were selected from the following requirements: I) Track reconstruction improvements. The spatial precision and efficiency for particle tracks are improved, allowing for better recognition of decay vertices of heavy-flavor mesons and baryons. II) Increase the

amount of data that can be handled simultaneously. The luminosity of Pb-Pb collisions increased, eventually reaching an interaction rate of 50 kHz, corresponding to an instantaneous luminosity of $\mathcal{L} = 6 \times 10^{27}$ cm$^{-2}$s$^{-1}$. The ALICE detector accumulated and read out more than 10 nb$^{-1}$ of Pb-Pb collisions, which is around $10^{11}$ interactions. III) Maintain the particle identification capabilities, which are crucial for detecting and selecting low-momentum quarkonium and other heavy-flavor signals [21].

The ALICE detector weighs approximately 10,000 tons and has dimensions of $16 \times 16 \times 26$ m$^3$. It consists of 18 sub-detectors that work together with different specifications [54]. The detectors can be divided into two categories based on their placement: detectors in the central barrel and detectors in the forward direction, as shown in table 3.1. The entire detector is shown in figure 3.2 together with the subdetector placements. Sub-detectors most relevant to this thesis will be described in detail in the next sections.

| Central Detectors | Forward Detectors |
|---|---|
| Inner Tracking System (ITS) | Zero Degree Calorimeter (ZDC) |
| Time-Projection Chamber (TPC) | Photon Multiplicity Detector (PMD) |
| Transition Radiation Detector (TRD) | FIT |
| Time-of-Flight (TOF) | Muon Spectrometer |
| High Momentum Particle Identification-Detector (HMPID) | |
| Photon Spectrometer (PHOS) | |
| Electromagnetic Calorimeter (EMCAL) | |
| ALICE Cosmic RAY Detector (ACORDE) | |

*Table 3.1: The different ALICE subdetectors.*

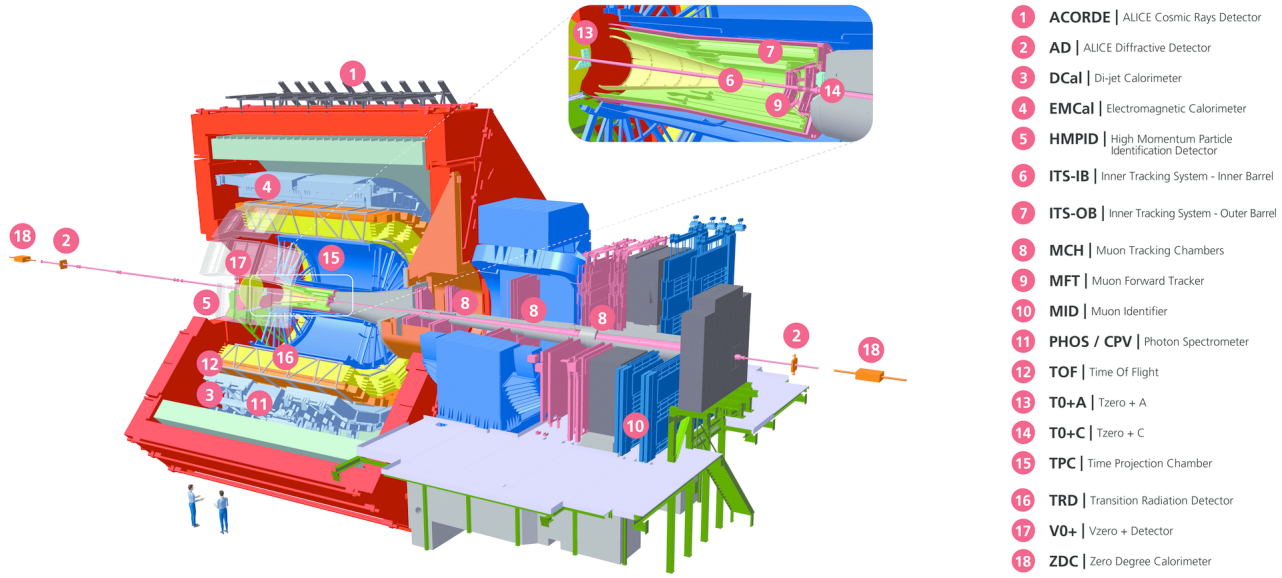


*Figure 3.2: Schematic of ALICE layout [11].*

### 3.2.1 Inner Tracking System

The Run 2 configuration of the Inner Tracking System (ITS) consisted of six layers of silicon detectors arranged cylindrically around the beam pipe, spanning a radial range of 39 mm to 430 mm and covering a pseudo-rapidity range of $|\eta| = 0.9$. The innermost layer was positioned as close to the beamline as possible, while the outermost layer was positioned at a radius that allowed for optimal matching with tracks from the Time Projection Chamber (TPC). The four outermost layers provided similar readout capabilities that allowed for Particle Identification (PID) via dE/dx measurements. Efforts were made to minimize the material budget, resulting in a radiation length of approximately 1.1% $X_0$ per layer, the lowest among all LHC experiments. The major limitation of the Run 2 ITS configuration was the maximum readout rate of 1 kHz. In scenarios where a suitable trigger could not be applied, the 8 kHz of Pb-Pb collisions that ALICE provided under run 2 could not be fully utilized. During LS2 the following relevant upgrades were therefore done to ITS:

- Reduction of beam pipe diameter, allowing for detection layer closer to the beamline where the collision takes place. A seventh layer has been included and the radii of the layers now are between 22 mm to 430 mm. A schematic of the new ITS is seen in figure 3.3.
- Material budget has been further reduced allowing for significant improvements in tracking and momentum performance. This is mostly done using new Monolithic Active Pixel Sensors (MAPS), using seven times less silicon per layer when compared to the old ITS pixel layers. They also reduce the power density by around two, thanks to optimizations in read-out architecture, further reducing the material budget used for signal cables and electrical power. Combined with improvements in cooling, mechanics, and other detectors all contribute to a radiation length of 0.3 % per layer for the three inner layers and 0.8% per outer layer.
- All seven layers of the ITS2 consist of pixel detectors. This means that the new

ITS no longer measures ionization in its silicon layers. The benefits of PID did not outweigh the cost in read-out times and material budget.

- The old maximum readout of 1kHz has been significantly increased up to 100 kHz for Pb-Pb and 400 kHz for pp, roughly twice the requirements.

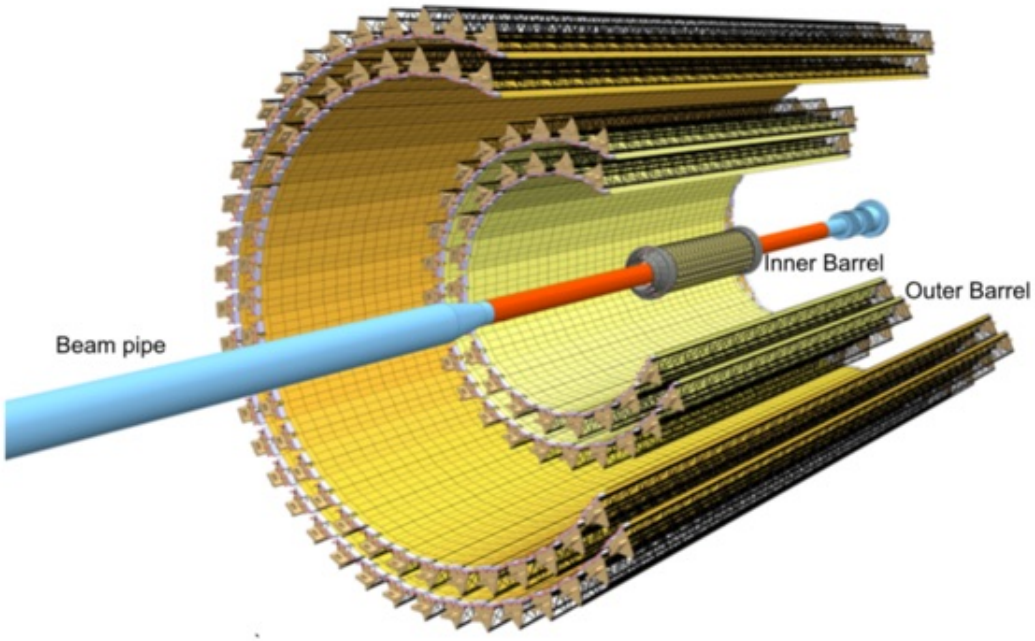


*Figure 3.3: Schematic of the ITS2 [12].*

The tracking efficiency of ITS 2 can be compared to that of a combination of the old ITS and TPC, while also performing effectively at lower momenta. The momentum resolution of the new Silicon trackers is approximately 4% up to 2 GeV/$c$ and remains below 6% up to 20 GeV/$c$. The hit resolution is around 5 $\mu$m [55].

### 3.2.2 Time Projection Chamber

The ALICE Time Projection Chamber (TPC) is the largest detector of its kind, with an active volume of 90 m$^3$. The cylindrical field cage contains a central high-voltage electrode (400 V/cm) and readout planes on each endplate as can be seen in the TPC schematic in 3.4. It covers the full azimuth in $|\eta| = 0.9$ and tracks charged particles over a wide range of transverse momentum ($p_{\mathrm{T}}$). The inner radius is located approximately 85 cm from the beam line, and the outer radius extends to cover the full pseudo-rapidity range. The field cage is filled with a gas mixture of $Ne - CO_2 - N_2$ (90-10-5). Charged particles passing through the gas mixture will ionize the gas creating free electrons. Free electrons are accelerated by the drift voltage and move towards the endcaps, where they are detected at the readout plane. Tracking of charged particles and particle identification using energy loss through ionization ($\mathrm{d}E/\mathrm{d}x$) is performed using 152 different pad rows placed along the trajectory to measure the ionization. The resolution in proton-proton (pp) and lead-lead (Pb-Pb) collisions is approximately 5.5% and 7%,

respectively. Topological reconstruction of weak decays is also used for particle identification.

The Run 2 configuration of the TPC had readout planes consisting of 72 MultiWire Proportional Chambers (MWPC), totaling approximately 550,000 readout cathode pads. These chambers operated using an active bipolar Gating Grid (GG) to protect the amplification region against unwanted ionization from the drift region, using an alternating voltage after a maximum drift time of 100 $\mu s$. This gating caused a dead time of around 280 $\mu s$, limiting the TPC rate to approximately 3.5 kHz. Achieving the 50 kHz goal was impossible with such gates, and an equivalent mechanism was required. Back-drifting ions led to ion charge densities and drift distortions in the TPC, making precise measurements impossible. For Run 3 a new readout chamber based on multistage Gas Electron Multiplier (GEM) technology is applied. GEMs can operate at high rates reliably and provide intrinsic ion blocking, allowing the TPC to operate continuously at the 50 kHz collision rate while retaining the old $p_{\mathrm{T}}$ range [56].

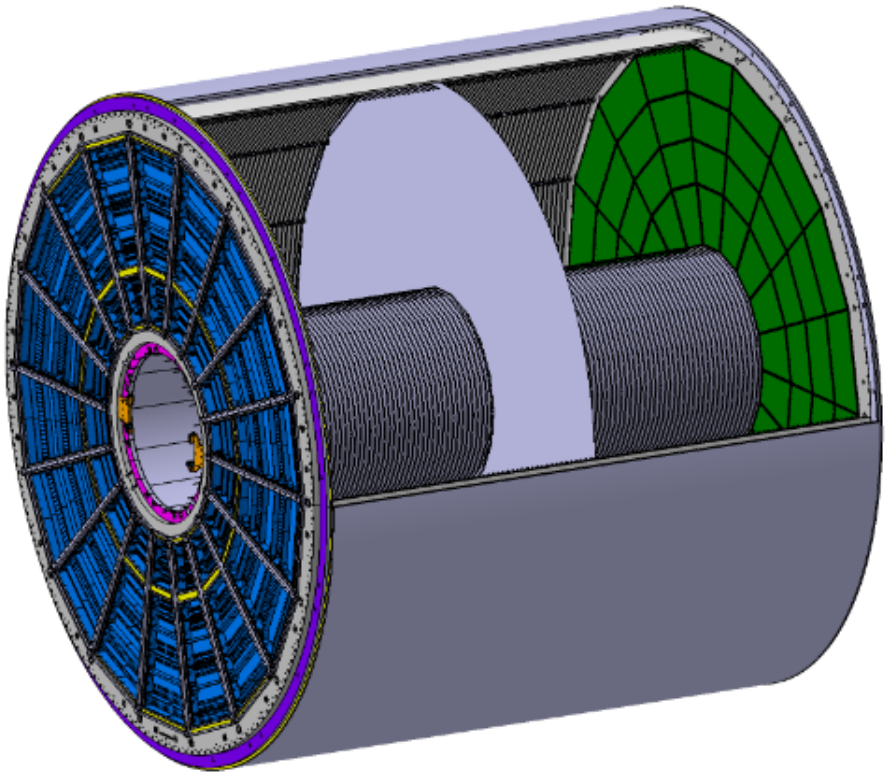

*Figure 3.4: Schematic of the TPC [13].*

## 3.3 Fast Interaction Trigger

During Long Shutdown 2 (LS2) at CERN's ALICE experiment, the legacy V0, T0, and Forward Replacement Detector (FMD) were replaced by the new Fast Interaction Trigger (FIT). It will provide both the minimum bias trigger and event selection based on

recorded multiplicity. FIT also rejects events caused by the beam colliding with the remains of gas in the beam pipe, called the LHC background. During some collisions without forward activity, FIT can serve as a veto tool. It can also serve as a tool to determine the event plane, z vertex, and collision time. Last, FIT also is used to determine the luminosity, which gives LHC information it can use to tune its beam in real-time [57].

There are three different detectors in the FIT. FV0, FT0 and FDD which can be seen in figure 3.5. They boast a >99% efficiency and a time resolution of less than 30 ps for Pb-Pb collisions. This high time resolution is utilized to select the collision vertex with a 1 cm resolution and to provide a start time for the Time-Of-Flight (TOF) detector. This new detector system offers improved performance and capabilities compared to the legacy detectors it replaced, providing ALICE with enhanced sensitivity and precision in its particle physics experiments.

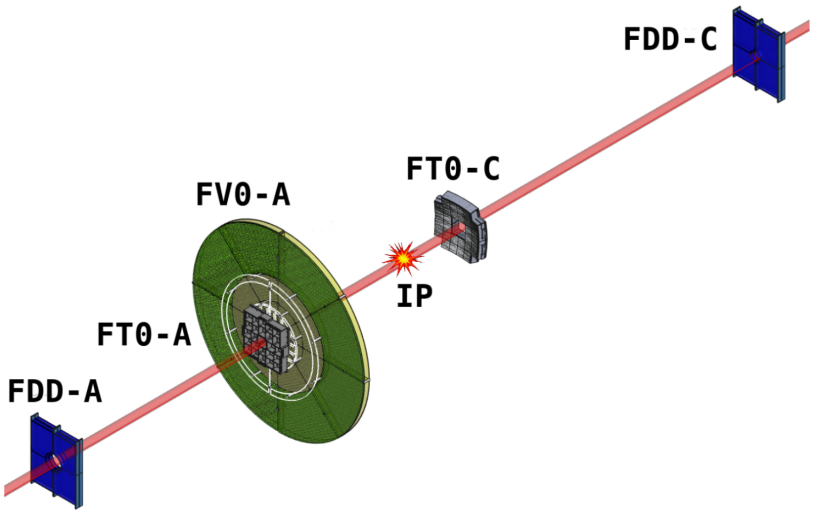


*Figure 3.5: Schematic of the FIT detectors [14].*

## 3.4 Tracking and vertexing

The different sub-detectors collect information about the particles traversing the detector, such as hit positions, charge deposits, and timing. From this information, it is possible to reconstruct the collision vertex and particle tracks. The interaction vertex is determined by the inner layer of ITS from these clusters, which finds the point where the maximum number of tracks converge. Next, the Kalman filter technique is utilized for track reconstruction using an inward-outward-inward scheme.

Inside the TPC, the first inwards stage commences by generating 152 clusters from the 152 pad rows. A track is drawn using the two first TPC clusters at the outer edge of the TPC, starting from a large radius away from the vertex point. This process is repeated using the first three clusters without the vertex. The procedure continues, adding clusters one by one if they are considered suitable candidates for the track. These early

tracks are regarded as seeds, and a specialized algorithm avoids utilizing the same clusters for different seeds beyond a specific limit. The worst seed of the two is dropped based on different quality parameters. The seeds that propagate to the inner TPC radius with a minimum of 20 clusters are accepted and utilized as seeds in the outermost ITS layers.

In the ITS, the process continues, tracking along clusters until reaching the innermost layer. The process then reverses, starting at the smallest radius in ITS, creating new seeds that propagate outwards through ITS and TPC, as before, and are used to match with tracks detected in TOF and TRD. Finally, refitting is performed, starting again at the outer TPC boundary and moving inwards. These last tracks are used to recalculate the collision vertex more accurately [54].

## 3.5 Particle identification

In addition to serving as the primary tracking device, the Time Projection Chamber (TPC) also provides vital information for particle identification (PID). When a high-energy particle travels through matter, it undergoes a series of inelastic Coulomb interactions with the electrons in the material, losing small amounts of kinetic energy by exciting or ionizing the atoms in the gas mixture. By calculating the charge and momentum of particle tracks and measuring the specific energy loss ($\mathrm{d}E/\mathrm{d}x$) at each cluster, it is possible to differentiate between various particles. The Bethe-Bloch formula is used to parameterize the energy loss and is given by [15]:

$$f(\beta\gamma)\frac{P_1}{\beta^{P_4}}(P_2-\beta^{P_4}-ln(P_3+\frac{1}{(\beta\gamma)^{P_5}})). \tag{3.1}$$

Here, $\beta$ and $\gamma$ represent the particle's velocity and Lorentz factor respectively, and $P_{1-5}$ are fit parameters. Figure 3.6 displays $\mathrm{d}E/\mathrm{d}x$ against particle momentum, demonstrating the separation between different particle species. At low momenta ($p \leq 1$ GeV/$c$), it is possible to identify particles on a track-by-track basis. For higher momenta, statistical separation is still feasible. As momentum increases, the Bethe-Bloch lines approach each other, making differentiation more challenging. Currently, it is possible to identify pions, kaons, and protons up to 50 GeV/$c$, which was limited to 20 GeV/$c$ before the upgrades. The resolution is approximately 5.5% and 7% for pp and Pb-Pb collisions, respectively.

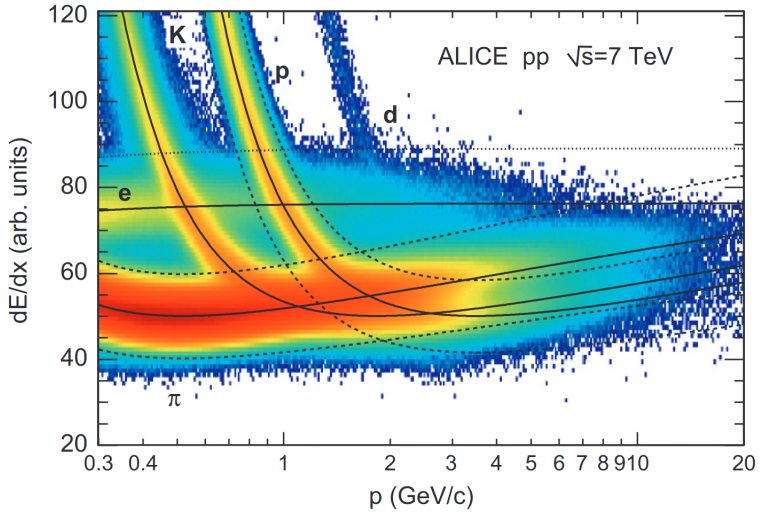


*Figure 3.6: Energyloss distributions calculated using Bethe-Bloch are shown with dark lines with the corresponding TPC parametrization from proton-proton collisions at $\sqrt{s}$ = 7 TeV [15].*

PID through energy loss is the primary method used in this thesis. However, there are other PID techniques used in ALICE, which are briefly explained below [58].

**Time-of-flight:** (TOF) performed in the aptly named Time Of Flight (TOF) detector, finds the velocity of a charged particle from the time $t$ the particle needs to move a distance $L$. Velocity depends on mass and momentum through

$$\beta = \frac{1}{\sqrt{(\frac{mc}{p})^2 + 1}}. \tag{3.2}$$

From this, mass can be calculated by measuring $L$, $t$, and $p$.

$$m = \frac{p}{c}\sqrt{\frac{c^2t^2}{L} - 1}. \tag{3.3}$$

**Cherenkov radiation:** Cherenkov radiation, detected by the FIT subdetector, results from a charged particle moving in a material with higher velocity than light moves in the same material. The radiation propagates at a given angle $\Theta$, depending only on particle velocity and refractive index $n$ of the material,

$$cos(\Theta) = \frac{1}{\beta n}.$$

A general Cherenkov detector, therefore, contains two things, a radiator where particles pass through and a photon detector.

**Transition radiation:** In Inhomogeneous media, transition radiation occurs when a charged particle crosses the boundary between media with different dielectric constants. Since the electric field from the particle changes in each medium, the difference is emitted as a photon. The energy loss depends on the Lorentz factor $\gamma = E/mc^2$ and can be used for particle discrimination in the Transition Radiation Detector (TRD).

**Electromagnetic calorimeter:** Calorimeters, such as the Electromagnetic Calorimeter (EMCal) and the Photon Spectrometer (PHOS), measure the energy of particles by initiating particle showers where the high-energy particle studied produces multiple new particles off lower energy levels. In the electromagnetic case, an electron, positron, or photon enters the calorimeter at high energies. Here photons interact via pair production, breaking up into electron-positron pairs. High energy positrons and electrons emit photons through bremsstrahlung. These two processes cascade until enough energy is depleted, and the processes can no longer occur. The energy of the original particle can then be determined from how large the particle shower inside the calorimeter becomes. This process absorbed the initial particle, meaning no further measurements are possible.

**Muon filter:** Since muons are similar to electrons in all aspects except mass, where muons outsize electrons by a factor of roughly 200. This means that they won't create electromagnetic showers inside of calorimeters, passing right through them instead. They can therefore be recognized in detectors outside of the calorimeters in specific muon detection detectors such as the Muon Tracking Champers (MCH), Muon Identifier (MID), and Muon Forward Tracker (MFT). All other charged particles will be absorbed in the calorimeter, making the muons easier to detect.

# Chapter 4

# Analysis tools and data selection

This chapter introduces the tools used to perform analysis and the data it was performed on. Furthermore, motivation for the various cuts and selection of data is shown. Secondly, a study on combining background constituents for signal extraction is presented. The cuts and background methods shown in this chapter are used for the analysis work done in chapter 5.

## 4.1 The Online-Offline framework

For Run 3 a new computing framework was developed to handle the requirements of data during continuous readout mode. The new computing framework from the ALICE Collaboration is called Online-Offline ($O^2$) [59] because of how it handles both the online data readout and the following offline processing. It draws from the original ALICE High-Level Trigger architecture [60] used during Run 1 and 2 as a message-passing system. $O^2$ consists of three different layers with specific tasks. The transport layer is implemented using the FairMQ [61] message-passing toolkit. It works by defining core blocks of the architecture as FairMQDevices (devices) which then can share a memory on the same computing node without copying information. The next component is the $O^2$ data model, a programming-language-agnostic used to describe the messages being exchanged. It handles various data formats, including some processes specific to different subdetectors. The main formats used are the Apache Arrow [62] columnar format and different ROOT [63] objects such as histograms. The last layer is the Data Processing Layer, introduced to hide the complexities of the first two layers. It serves as a translator of the user input and breaks it down into different computational problems that can be solved [64].

AliPhysics [65], the Run 2 analysis framework, structured its information in an object-oriented way, similar to classic C++ programming. It was designed to deal with arrays of structures, such as multiple events with different variables and sizes stored inside of them. These structures would then be stored inside of other structures causing a hierarchy. On the other hand, $O^2$ uses flat tables handled through the earlier mentioned package called Arrow. This package is widely used in data science and is not made by or specific to CERN. Instead of having arrays of structures, Arrow has structures of arrays. This allows for more convenient ways of dealing with said arrays, as they can be

interlinked significantly more efficiently and allow for faster data processing. An example of how the new flat tables structure works can be seen in table 4.1.

| Collision table | Vertex Z |
|---|---|
| Row 1 | 5.82 |
| Row 2 | 2.45 |
| Row 3 | -2.56 |

| Track table | Collision index | $p_T$ | $\phi$ | $\eta$ |
|---|---|---|---|---|
| Row 1 | 1 | 1.23 | 0.04 | -0.32 |
| Row 2 | 1 | 0.23 | 1.03 | 0.35 |
| Row 3 | 2 | 1.56 | -0.35 | -0.64 |
| Row 4 | 2 | 2.01 | 0.45 | 0.12 |
| Row 5 | 2 | 0.93 | -0.54 | -0.03 |
| Row 6 | 2 | 0.56 | 0.23 | -0.2 |
| Row 7 | 3 | 1.74 | 1.35 | 0.09 |

*Table 4.1: Example tables used to show the new flat table structure in $O^2$. It also shows the new index values that are used to link them together. All values are fabricated as they are only meant to be used as an example. In the collision table, vertex z info is shown. While $p_T$, $\phi$, and $\eta$ are shown in the track table.*

The table shows some arbitrary information about tracks and collisions. The new flat table structure of $O^2$ is dependent on an index number. The collision and track table can coexist separately without any links except these index values. In the example, tracks 1 and 2 would be linked to collision 1. The next four tracks are linked to collision 2 while the last track is linked to collision 3. This would normally require a lot of computational power to link up tracks and collisions using normal for-loops or other coding tools, but the Arrow package does it automatically and efficiently. The new way of indexing means that the access hierarchy is reversed. In Aliphysics, collisions contain tracks, in $O^2$ tracks will refer to the collisions instead. Some designs from the old system are still kept moving forward. ROOT files are still the I/O backend of the framework. Inside ROOT the data is stored in multiple TTrees in TFiles, and the new O2 AODs (AO2Ds) can still be inspected with the Tbrowser [66].

## 4.2 Data sample

After the start of Run 3, ALICE has been collecting data from proton-proton collisions in different periods. The total amount of data from each of these periods is shown in table 4.2.

| Period | Size(full) |
|---|---|
| 22m | 341 TB |
| 22o | 2 PB |
| 22p | 95 TB |
| 22q | 10 TB |
| 22r | 229 TB |
| 22t | 68 TB |
| Full PP datasets | 3 PB |

*Table 4.2: Table showing the total amount of PP data in all different periods [67].*

These datasets are currently too large to be looked at as a whole. Instead, the focus has been looking at smaller runs. This is done to get a better understanding of which data should be included when skimming larger datasets later and to get a better idea of the quality of the datasets themself.

Because of the large variance in quality between datasets, this thesis uses three different runs, skimmed by the Norwegian ALICE analysis group. These skims contain cuts that are at least as loose as the cuts introduced in the following section, meaning they will not impact the results. These runs also have premade post-calibrations that will be used. Consequently, the quality of these runs is ensured. Additionally, the amount of data that has been skimmed is more than what would have been possible to run locally.

From period 22r runs 529324 and 529341 contain 1.6e+07 events in total while from period 22m is Run 523308 used containing 1.1e+06 events. For the rest of this chapter period 22r will be used as the primary dataset because of its higher statistic while 22m is used in chapter 5 to show the signal extraction progress.

### Event selection

The number of events correlated to each Run is after a small correction from event selection to ensure good collision candidates from beam-beam collisions while rejecting beam-gas collisions. When the beams collide they come with a small angle in relation to each other, causing the primary vertex position to spread. In the transverse plane, this effect is negligible. However, it can affect the longitudinal plane along the beam direction with multiple centimeters. This will not be a problem unless it means that the events fall outside of the central barrel detector's geometrical acceptance. To be on the safe side a cut around the collision vertex position in the z-direction is used where z must be inside of the range [-10 cm, 10 cm].

## 4.3 Track selection

J/$\psi$-mesons that decayed via the di-electron channel are reconstructed using the electron and positron tracks from ITS and TPC in the central barrel. To select the best electron candidates and reduce the background, different cuts are made for the track selection. These selections are based on different requirements set on the kinematical quantities, the quality of the track reconstruction, and some particle identification-specific cuts. The cuts are summarized in table 4.3 and described in detail in the following subsections.

| Variable | cut |
|---|---|
| Kinematical cuts | |
| $\|\eta\|$ | <0.9 |
| $p_{\mathrm{T}}$ | >1 GeV/$c$ |
| Track quality cuts | |
| TPC $\chi^2$ | < 4.0 |
| TPC n clusters | > 70 |
| Is SPDany | Yes |
| Particle identification | |
| TPC n$\sigma$ electron | $\in$[-3,3] |
| TPC n$\sigma$ pion | >3 |
| TPC n$\sigma$ proton | >3 |

*Table 4.3: Table showing different cuts used on data to reduce the background tracks and other tracks that in some ways are considered unsatisfactory.*

### 4.3.1 Kinematical cuts

The kinematical cuts are set to ensure that the full acceptance of TPC is used and to reject background tracks. The central barrel accepts tracks with a polar angle $\theta$ between 45° and 135° which is equivalent with the pseudorapidity cut $|\eta|$ <0.9. The requirement for $p_{\mathrm{T}}$ to be above a certain threshold removes the background from soft particle contributions in the J/$\psi$ signal extraction. A cut at the lowest region for transverse momentum will not limit the J/$\psi$ reconstruction because the rest mass of J/$\psi$ requires at least a momentum transfer around 1.5 GeV/$c$ per electron candidate in its restframe. This means that the J/$\psi$ reconstruction down to zero transverse momentum is still possible despite a minimum $p_{\mathrm{T}}$ being applied for the electrons. The distribution of the remaining tracks $p_{\mathrm{T}}$ and $\eta$ values are shown in figure 4.1 after the mentioned cuts are applied. The $\eta$ distribution is supposed to look mirrored around 0 and expand uniformly out from there. The gathering of tracks around $\eta = 0.3$ is not expected. This can partly be explained by space charge distortions as shown in figure 5.16.

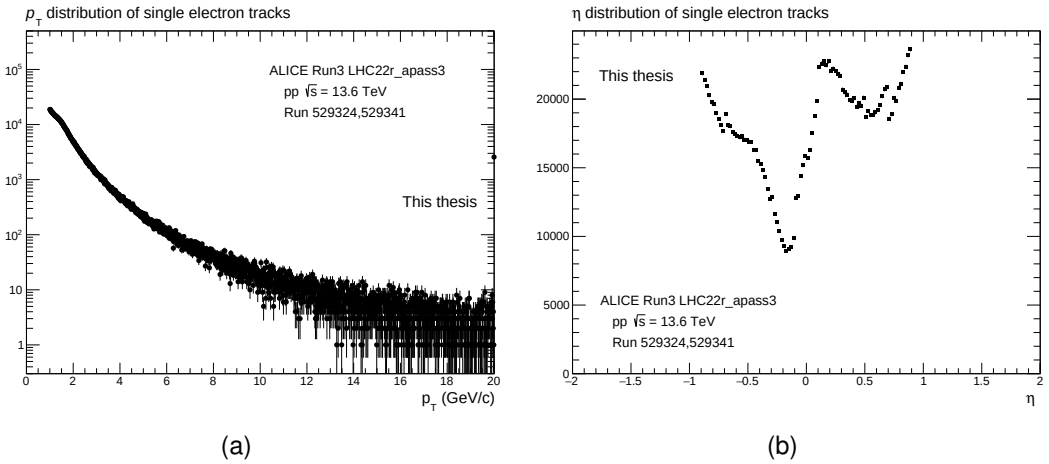


*Figure 4.1: (a) The track distribution for different $p_T$ values. All tracks with $p_T$ below one have been removed. (b) The track distribution for different $\eta$ values. All tracks with values outside of -0.9 and 0.9 have been removed.*

### 4.3.2 Track quality cuts

Tracks are reconstructed in the TPC by recognizing which clusters the particle moved through. Therefore, to ensure good track reconstruction, it is required that at least 70 of the 152 pad row clusters for each particle track is registered. The track is then checked for its $\chi^2$, where a value around 1 is preferred, but any value below four is accepted. Additionally, with the use of the SPDany requirement, the track has to have at least one hit in any of the two innermost layers of the ITS. This helps reduce the contributions from gamma conversions in the detector material. Figure 4.2 (a) shows how many clusters the different electrons are associated with, where most are located around 130 and the cut at 70 is shown. The corresponding $\chi^2$ of these tracks are distributed in figure 4.2 (b).

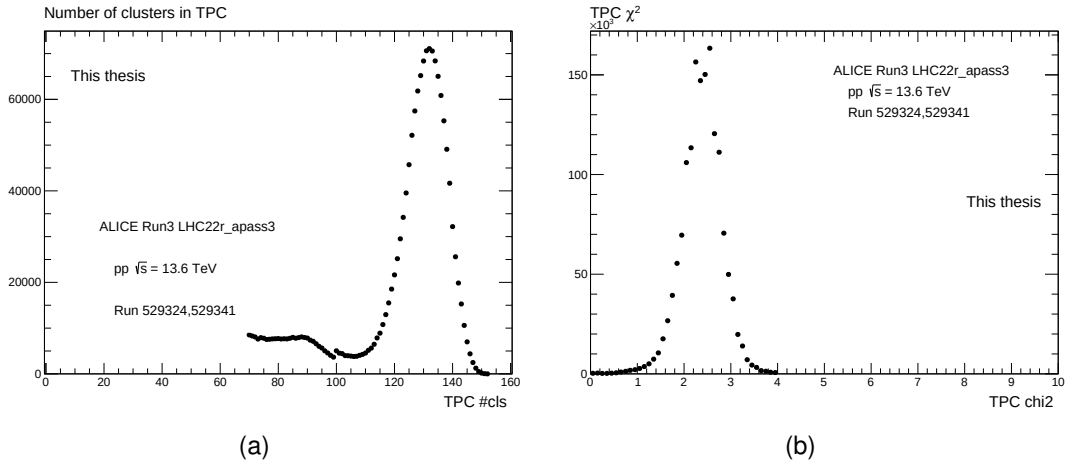


*Figure 4.2: (a) The track distribution for different amounts of clusters passed. All tracks with clusters below 70 have been removed. (b) The track distribution for different $\chi$ values. All tracks with values above four have been removed.*

### 4.3.3 Particle identification cuts

The energy loss in TPC is measured to identify the electron candidate tracks against all other possible particles. If the tracks deviate far from the expected energy loss calculated using the Bethe-Bloch formula given in equation 3.1, they are discarded. The deviation is measured using

$$n\sigma = \frac{(d\mathrm{E}/dx)_{\mathrm{meas}} - (d\mathrm{E}/dx)_{\mathrm{exp}}}{\sigma_{\mathrm{exp}}}. \tag{4.1}$$

Here, $(d\mathrm{E}/dx)_{\mathrm{meas}}$ is the energy loss measured while $(d\mathrm{E}/dx)_{\mathrm{exp}}$ is what Bethe-Bloch predicts. The denominator $\sigma_{\mathrm{exp}}$ comes from the energy loss measurement resolution. The PID selections are designed to keep electron candidates only using tracks with a maximum of three sigmas away from the electron line. At higher momenta, the separation between electrons, pions, and protons worsens, making the resolution worse. The tracks where the energy loss is less than three sigmas away from the pion or proton lines are also removed. The PID-related plots for LHC22r are shown in figure 4.3. The color represents the number of particles located at the given values. More particles located around the electron band give an indication that good candidates are selected.

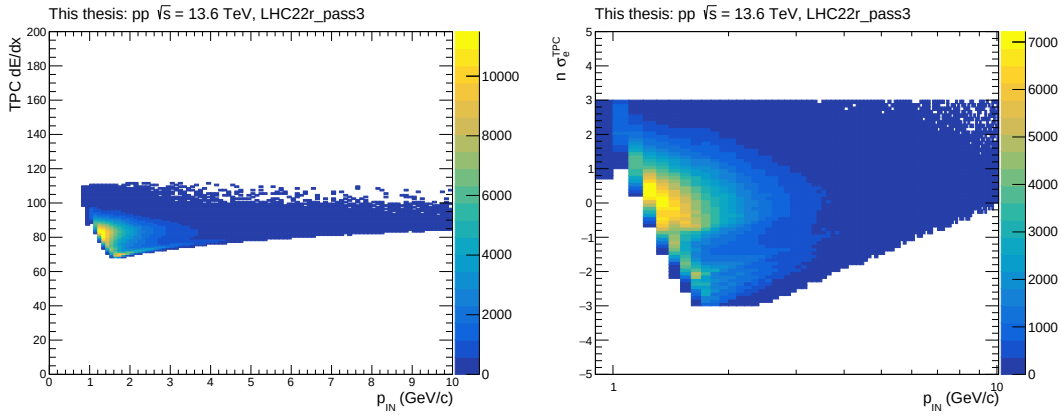


(a) (b)

*Figure 4.3: (a) The number of particles with a given momentum that lost a certain amount of energy inside the TPC. The plot is a heat map, meaning the color indicates the number of particles. The remaining particles are placed no more than 3 σ away from the electron line and no closer than 3 σ away from the pion and proton lines. (b) Electron nσ as a function of momentum in TPC plotted with a heat map.*

## 4.4 J/$\psi$ signal extraction

The J/$\psi$-meson decays too fast for direct measurements; instead, reconstruction of the invariant mass of electron-positron pairs is used. The distribution will contain the J/$\psi$ signal and different background contributions, which must be removed for precise signal extraction. The invariant mass from the decay of multiple constituents is given by

$$M^{inv} = \sqrt{\sum_{i=1}^{k} p_i^{\mu} p_{\mu}^{i}} = \sqrt{\sum_{i=1}^{k} (E_i)^2 - \sum_{i=1}^{k} (\overrightarrow{p}_i)^2}, \tag{4.2}$$

where $p_i^{\mu}$=$(E_i, \overrightarrow{p}_i)$ represents the four-momentum vector for a particle with index $i$. Finding the invariant mass of an electron pair with this formula looks like

$$m_{ee} = \sqrt{(E_{e_1} + E_{e_2})^2 - ((p_{e_1} + p_{e_2})^2}. \tag{4.3}$$

The indexes $e_1$ and $e_2$ indicate the different legs of the pair. The energy of the individual electron $E_e$ is given by

$$E_e = \sqrt{(\overrightarrow{p}_e)^2 + m_e^2}, \tag{4.4}$$

where the electron rest mass is constant $m_e = 0.511$ MeV/$c^2$. After the various cuts, the tracks are combined into $e^+e^-$ pairs. A signal peak around 3 GeV/$c^2$ would correspond to the J/$\psi$ resonance area. Most di-electron pairs come from different background sources, meaning the signal will be comparatively small against the background, even in the signal region. The background combines different $e^+e^-$ pairs without a common physical source, called the combinatorial background, and pairs originating from a common physical source, the residual background. Decay products from quarkonia or jet fragmentations are examples of different common physical sources from which electron pairs could emerge. To have a clear J/$\psi$ signal, a good way to determine the background is required.

### 4.4.1 Background subtraction

The J/$\psi$ resonance peak occurs when looking at opposite sign (OS) pairs from the same event (SE). To describe the background shape, several possible ways of combining the electron and positron pairs exist where the background without the signal peak is constructed. This is done using groups of particles with the same electric charge, called like sign (LS), and from taking electrons and positrons from different events together as pairs called mixed events (ME). The distributions of different pairmasses are shown for SE tracks in figure 4.4 and for ME tracks in 4.5. The peak only appears in SELS shown in figure 4.4 (a). However, the MEOS is not able to fully parametrize the SEOS background. After the subtraction, there is a residual background coming from the correlated background.

Because of the increased data-taking rate, many analysis algorithms are redone to be stricter about the required memory and computational time. Event mixing selects distinct collisions based on different values, such as their multiplicity, z-vertex, and iterations done over the tracks from the collisions. During Run 2, events were put in different buffers based on the considered properties, where pairs are combined randomly. The new Run 3 method uses a lazy generation of selected data elements and a binning policy. This means that only the different table types combinations and how they will be binned needs to be stored. Now it is allowed to use tuples of any size,

which includes any number of properties taken from any analysis table. The mixing of events and pairing of like signed tracks is then done inside of these tuples, ensuring that they are not completely incompatible [68].

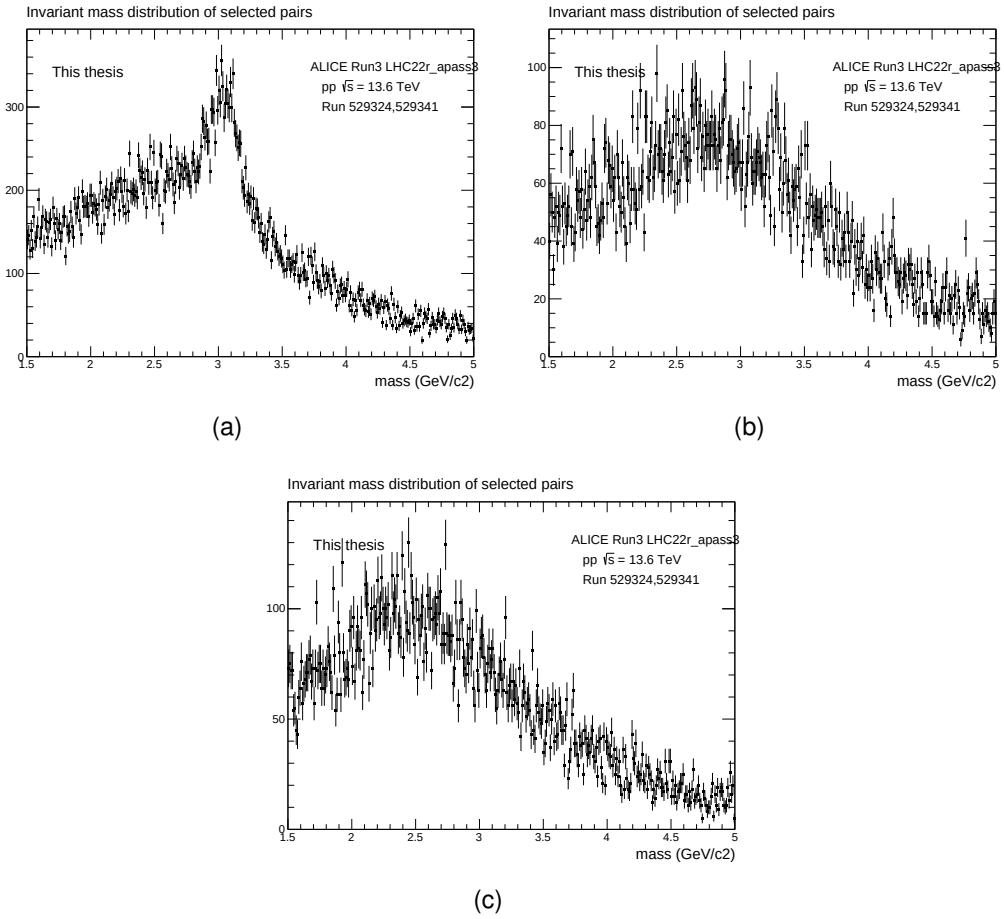


*Figure 4.4: (a) Pairmass of tracks with opposite sign. Total entries in the graph: 54752. (b) Pairs where both constituents are negative. Total entries in the graph:19474. (c) Pairs where both constituents are positive. Total entries in the graph: 22156. All pairs are made from the same events.*

The following subsections explain different ways of combining the different ME and SE pairings of different electric charges. In some cases, it is possible to do the same calculations by either combining histograms into new histograms or using the integrals of histograms as constant scaling factors to change the values of other histograms. This impacts both how the background distribution looks and its corresponding error. When a constant factor is used, an integral approach has been applied.

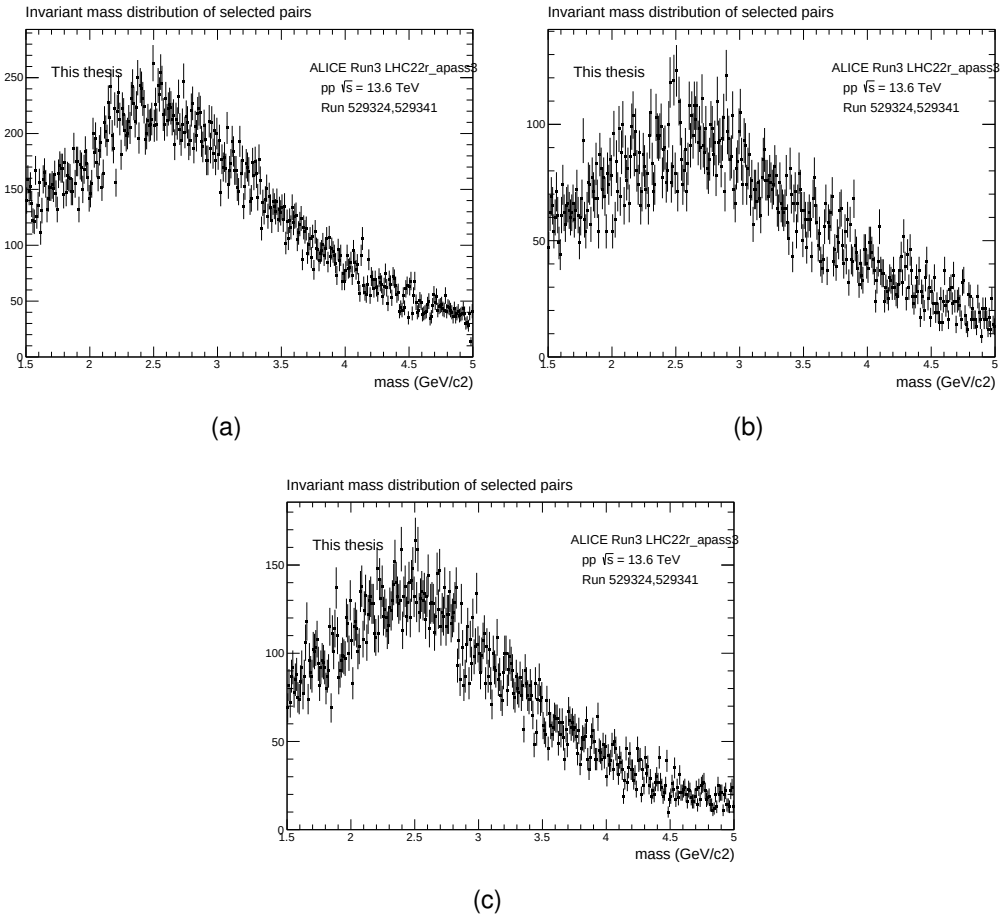


*Figure 4.5: (a) Pairmass of tracks with opposite sign. Total entries in the graph: 51077. (b) Pairs where both constituents are negative. Total entries in the graph: 28686. (c) Pairs where both constituents are positive. Total entries in the graph: 23024. All pairs are made from mixed events.*

The background combinations are made using common tools to calculate the mean. The arithmetic mean works around adding and dividing values, while the geometric mean multiplies together and takes the root of the product. The arithmetic mean is always higher than the geometric mean, but the latter is less affected by statistical outliers. Additionally, it is attempted to combine a background from MEOS and then scale with the ratio between SE and ME.

Different values are calculated using the backgrounds to compare the three methods. The number of J/$\psi$ candidates $N_{J/\psi}$ is calculated by taking the integral over the resonance area (from 2.92 GeV/$c^2$ to 3.16 GeV/$c^2$ is used here) for both the SEOS histogram and background histogram. $N_{J/\psi}$ is then given by subtracting the signal from the background, while the error is given by combining the integral errors from both using

$$N_{J/\psi error} = \sqrt{(\text{error}_{\text{SEOS}})^2 + (\text{error}_{\text{bkg}})^2}. \tag{4.5}$$

Next, the signal is compared with the background to find a ratio between them

$$\frac{S}{B} = \frac{\text{SEOS-bkg}}{\text{bkg}}. \tag{4.6}$$

Here $S$=SEOS-bkg=$N_{J/\psi}$ while $B$ is just the background. Another way to compare the signal strength with the background is to find the significance from

$$\text{significance} = \frac{S}{\sqrt{S-B}} \tag{4.7}$$

The different methods are explained in the following subsections, where calculating the correction factor as a histogram and an integral are both shown. The different methods are then compared in subsection 4.4.5.

### 4.4.2 Geometric mean

The geometric mean is calculated using the particle pairs with the same charge from the same event. They are combined by multiplying them together and then taking the root over the product. The exact formula is

$$\text{Bkg}_{\text{geo}} = 2 \times \sqrt{\text{SEPP} \times \text{SEMM}} \times \text{R}. \tag{4.8}$$

Here, SEPP and SEMM represent pairs from the same event, with P representing plus and M representing minus, which is the electric charge of the pair. There is a possibility that there will be a significant difference between the acceptance of LS and OS pairs. The R factor is a correction made by comparing the difference between LS and OS for mixed events.

$$\text{R} = \frac{\text{MEPM}}{2 \times \sqrt{\text{MEPP} \times \text{MEMM}}}, \tag{4.9}$$

where MEPM is MEOS while MEPP and MEMM are the two different possibilities for MELS. Because of how ALICE has full azimuthal coverage in its central barrel, the R factor is expected to be close to unity. The geometric mean is calculated by using the R factor as a histogram and an integral in figure 4.6 (a) and (b), respectively.

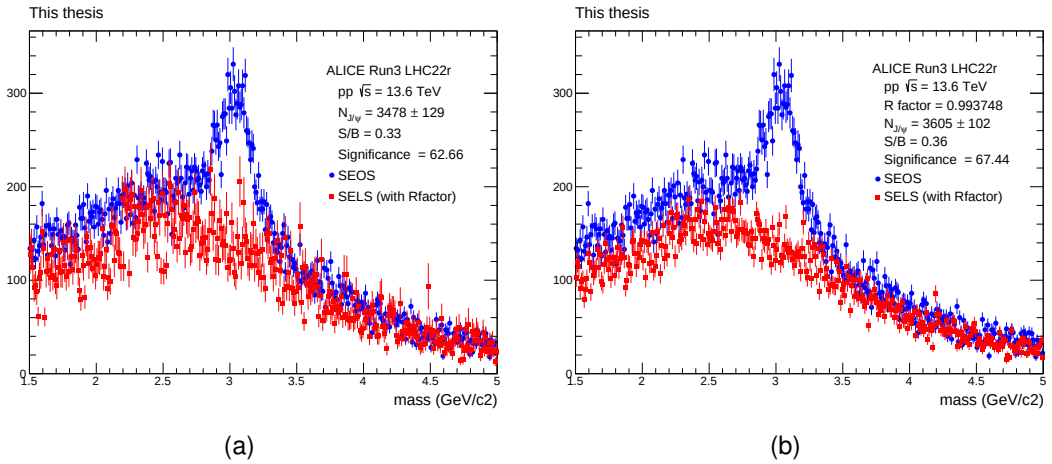


*Figure 4.6: (a) Signal extraction by using the geometric mean with the R factor calculation by using mixed events as histograms. (b) Signal extraction by using the geometric mean with the R factor calculation by taking the integral over mixed events.*

### 4.4.3 Arithmetic mean

The arithmetic mean starts with combining the like-signed pairs from the same event by adding them together and multiplying with the correction factor using

$$\mathrm{bkg}_{\mathrm{ari}} = (\mathrm{SEPP} + \mathrm{SEMM}) \times \mathrm{R}. \tag{4.10}$$

The correction factor takes into account the difference in acceptance between like sign and opposite sign tracks calculated using mixed events as

$$\mathrm{R} = \frac{\mathrm{MEPM}}{\mathrm{MEPP} + \mathrm{MEMM}}. \tag{4.11}$$

The arithmetic mean is calculated using the R factor as a histogram and an integral in figure 4.7 (a) and (b), respectively.

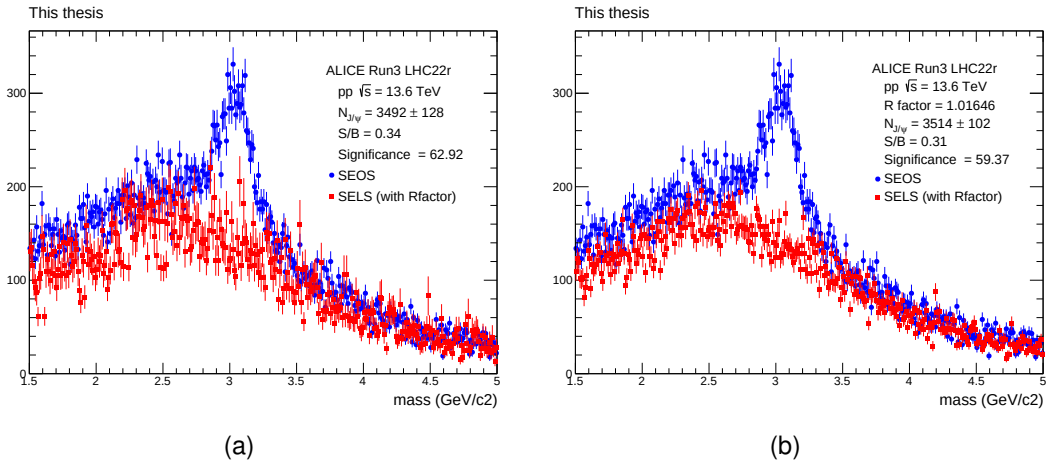


(a) (b)

*Figure 4.7: (a) Signal extraction by using the arithmetic mean with the R factor calculation by using mixed events as histograms. (b) Signal extraction by using the arithmetic mean with the R factor calculation by taking the integral over mixed events.*

### 4.4.4 Mixed event bkg

Building the mixed event background starts with assuming that the MEOS will be shaped in a similar way as SEOS except for in the signal region. To account for the possible differences in acceptance between SE and ME. The ME gets scaled using an R factor, meaning the background becomes

$$\text{mixbkg} = \text{MEPM} \times R. \tag{4.12}$$

The R factor is calculated using the ratio between the integral of the same events and integrals of mixed events outside of the signal extraction area.

$$\text{R} = \frac{\text{SE}}{\text{ME}} \tag{4.13}$$

The areas integrated over for both SE and ME are from (1 GeV/$c^2$, 2.5 GeV/$c^2$) and (3.72 GeV/$c^2$, 5.0 GeV/$c^2$) to ensure that no particles from the resonance area are included. The two integral values from the two areas are combined for SE and ME individually, then the ratio between them is used to scale. The background with and without scaling is shown in 4.8. The scale turns out to be insignificant because the acceptance between ME and SE are very similar.

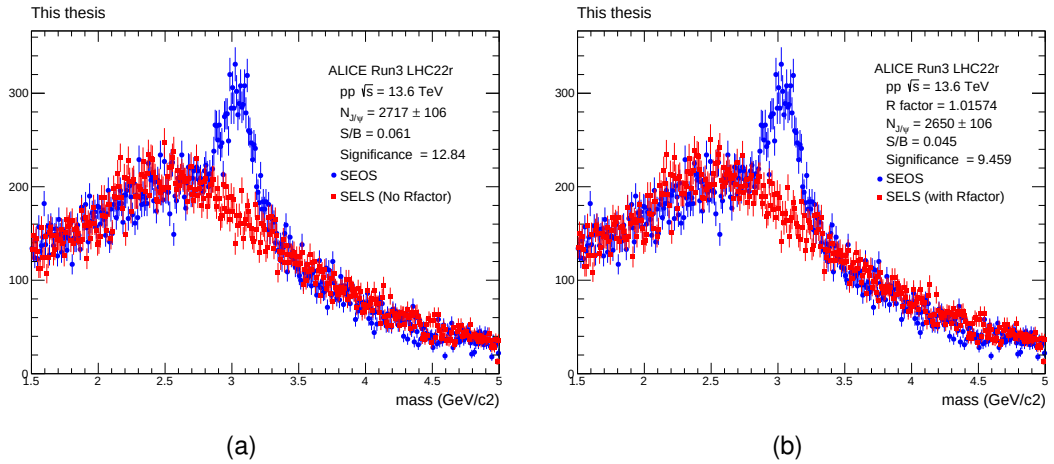


(a) (b)

*Figure 4.8: (a) Signal extraction by using the mixed event with the R factor calculation by using the ratio between SE and ME outside of the resonance area. (b) Signal extraction by using the MEOS for the background without any scaling factor. When using the R factor as a histogram, the uncertainty in each bin becomes larger*

### 4.4.5 Comparing the backgrounds

The R factor being close to unity means that there is a good acceptance rate between LS and OS, it is unnecessary to scale LS to get a good background estimation. When scaling bin for bin against a histogram, the background experience more variance between its data points, leading to larger uncertainty. This could be partly explained by the difference between acceptance between MEPP and MEMM, looking at the total amount of entries for the two. The significance is very similar for both geometric mean and arithmetic approaches, but when using mixed events, the measured $N_{J/\psi}$ is reduced by roughly 20%. The relevant values obtained by this study are shown in figure 4.4. Comparing the methods, the agreement between geometric and arithmetic means they are preferred over mixed event backgrounds. Using an R factor is not necessary since the histogram method just increases the error while the constant value is very close to unity. Another benefit of not calculating any scaling factors is that the only usage of mixed events in this thesis is removed. Therefore the computing power and time that is added to any analysis process for calculating mixed events are saved. The following chapter will thus combine SELS by adding the two constituents without any R factor correction.

| Background | $N_{J/\psi}$ | S/B | Significance | R factor |
|---|---|---|---|---|
| geohist | 3478 $\pm$ 129 | 0.33 | 62.66 | |
| geoconst | 3605 $\pm$ 102 | 0.36 | 67.44 | 0.99 |
| arihist | 3492 $\pm$ 128 | 0.34 | 62.92 | |
| ariconst | 3514 $\pm$ 102 | 0.31 | 59.37 | 1.01 |
| mixevntnor | 2717 $\pm$ 106 | 0.061 | 12.84 | |
| mixevwithr | 2650 $\pm$ 106 | 0.045 | 9.459 | 1.02 |

*Table 4.4: The relevant values used when comparing different methods of combining background.*

## 4.5 Residual background

The background can be divided into two parts from the $e^+e^-$ pairs origin. The combinatorial background consists of $e^+e^-$ pairs without a common physical source. This thesis estimates the combinatorial background using SELS tracks, as shown in the earlier subsections. The residual background is then the remaining $e^+e^-$ pairs with a common physical source such as the decay products of $c\bar{c}$ and $b\bar{b}$ or jet fragmentations. The remaining residual background can be estimated using an empirical fit after subtracting the combinatorial background, the data points after the subtraction is called Raw counts. The fit function used over the Raw counts assumes the remaining data is a combination of a linear background and a peak in the signal region that can be described as

$$f_{fit} = f_{bkg} + f_{peak}. \tag{4.14}$$

The linear background is described using a simple line equation such as $y = ax + b$ while the peak is described using a crystal ball function [69].

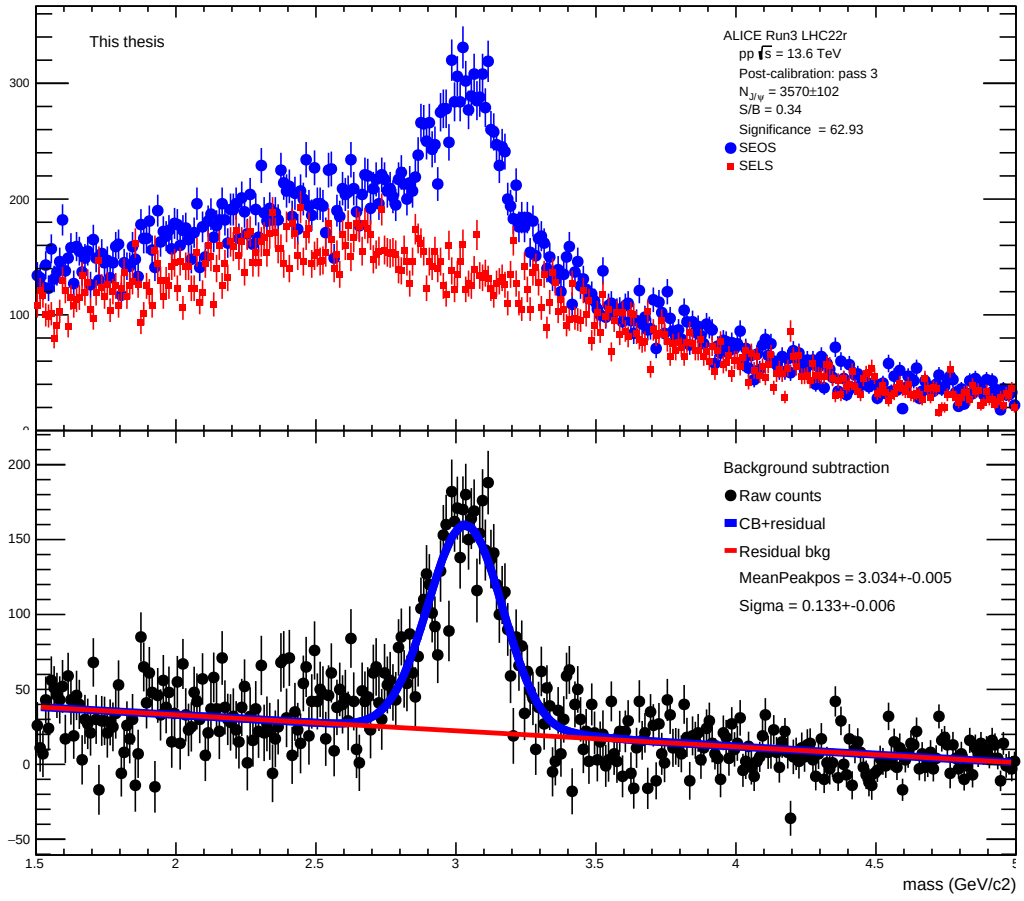


*Figure 4.9: The pair mass plot of LHC22r. The upper panel shows SEOS together with SELS used to describe the combinatorial background. The lower panel shows the data point from subtracting SELS from SEOS and creating a fit over the data to describe both the residual background and the peak.*

Using a fit such as in figure 4.9 means that the entire background is better described, but it also gives numerical values on properties of the peak region, such as the position and width (Sigma). When signal extraction is performed in chapter 5 it would be preferable to always include a fit for these reasons. The problem is that the fit usually does a very poor job of describing the data. Usually, the peak's fit shape is determined using Monte Carlo simulations. For Run 3, this is not available, and therefore some guesswork is used for the starting parameters. It could also be a problem with statistics or data quality. The fit assumes the peaks for Run 2 and Run 3 are similar, but as will be shown in chapter 5, they are not. Either way, a fit is not used to describe the remaining data shown in this thesis.

# Chapter 5

# Analysis in Run 3

This chapter showcases the analysis work performed in this thesis. Section 5.1 is focused on signal extraction and reproducing Run 2 results, while section 5.2 is impact parameter studies with a focus on the improvement in tracking performance.

## 5.1 Post-calibration

The work of reconstructing the J/$\psi$ signal using the LHC22m dataset is shown in figure 5.2. The signal region is extremely unclear, with the background nearly encapsulating the entire region, and it is very hard to tell where the region starts and ends. Another way to see the low quality of the data is by checking PID plots to ensure that the correct electrons are being analyzed as seen in figure 5.1.

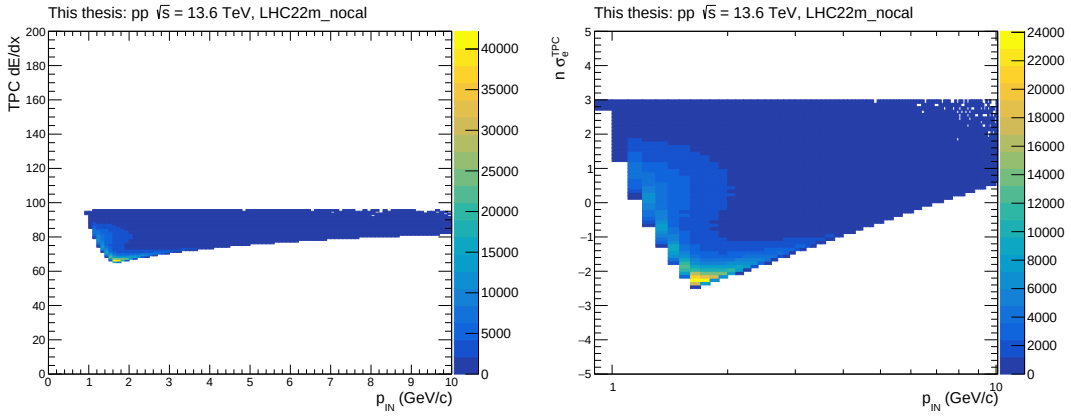


(a) (b)

*Figure 5.1: (a) The number of particles with a given momentum that lost a certain amount of energy inside the TPC. The small amount of particles located in the center means that few good electron candidates have been selected. (b) Electron n$\sigma$ as a function of momentum in TPC plotted with a heat map. Shows that most particles are located away from 0 $\sigma$ around the electron line.*

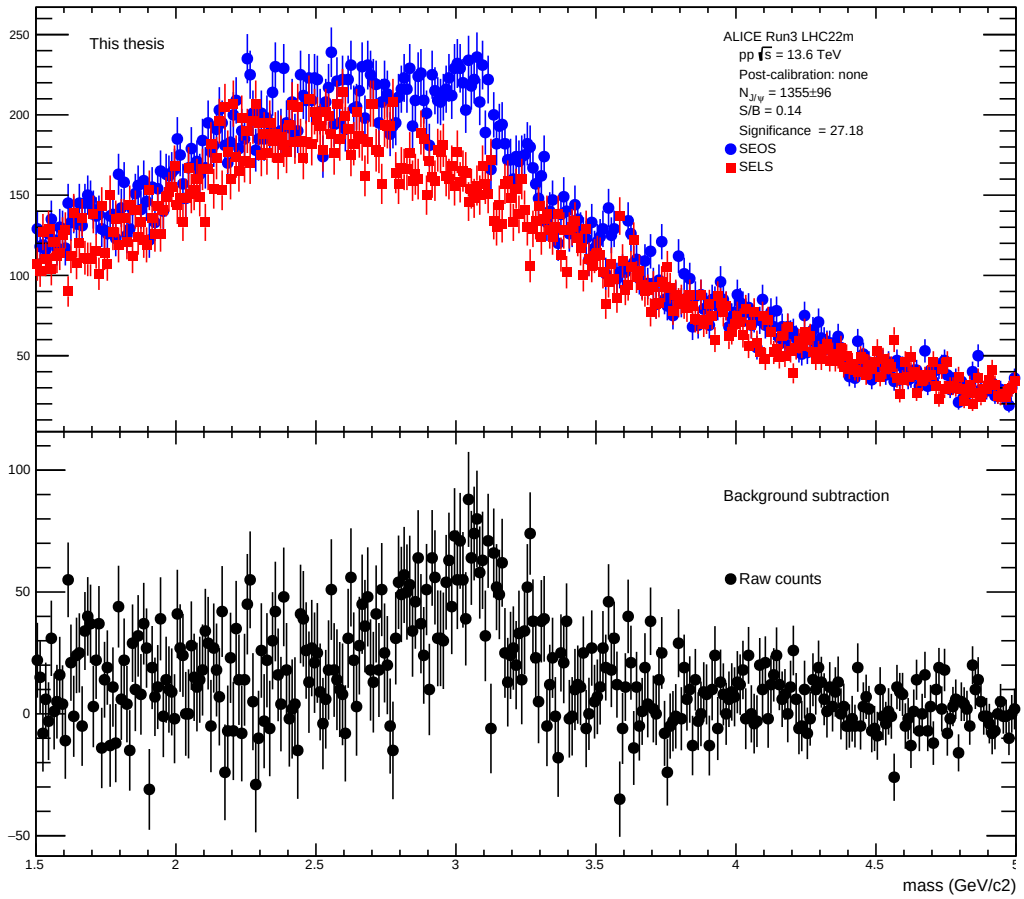


*Figure 5.2: Early signal extraction of the LHC22m dataset. No form of post-calibration was applied and the peak is nearly unrecognizable.*

The lack of particles in the electron band of the PID plots helps explain why the signal extraction for this dataset is much worse than for the optimized Run 2 data. The quality of a di-electron analysis depends a lot on the performance of the track PID. For this reason, post-calibration maps are made based on central calibration. These maps are made centrally, meaning that they do not need to be made by the user doing the analysis. The process starts in the V0 selector, where pure V0 particle samples are taken. Potential V0 candidates such as $K_0^S$, $\Lambda$, and photons are reconstructed from their decay topology. This means calculating the mass from their daughter tracks momentum and mass. An important aspect of this process is determining the Distance of Closest approach with the highest possible resolution as will be discussed in section 5.2.

The V0 sample could be electrons created from photons. These samples are then divided into specific cuts such as smaller number of clusters, $\eta$, or $P_{in}$ intervals. Next, the $n\sigma^{TPC}_{electron}$ is plotted and fitted in these intervals, with the intention of finding the mean and width. These values are now used to create the new $n\sigma$ values with the formula

$$n\sigma_{cor} = \frac{n\sigma - \text{mean}}{\text{width}}. \tag{5.1}$$

This equation moves the $n\sigma$ values towards 0, representing a better cut along the electron line. Next, the new calibration maps are then applied to improve PID performance.

This will lead to more background removal and a stronger signal in the J/$\psi$ resonance peak area.

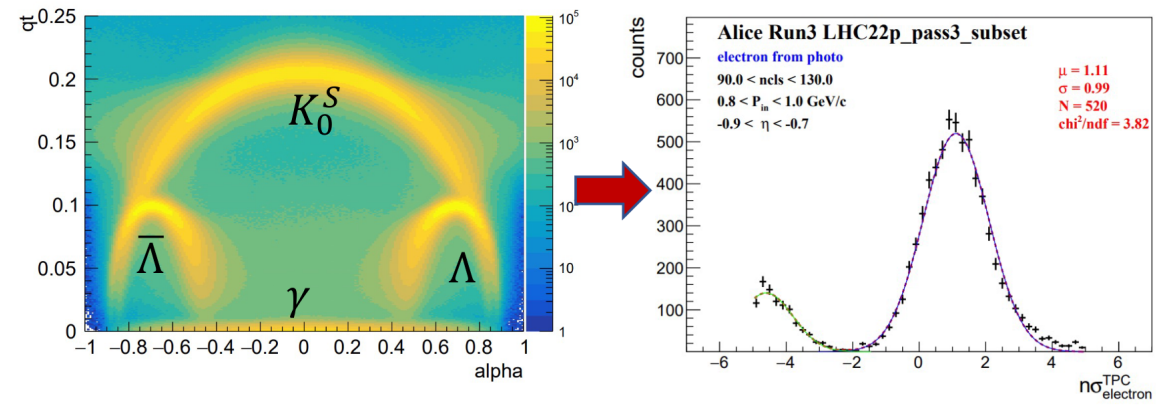


*Figure 5.3: Showing the process of making a post calibration. Starting from the left, the V0 selector finds electron samples from photons. A fit is created over n$\sigma$ to find the mean and width [16].*

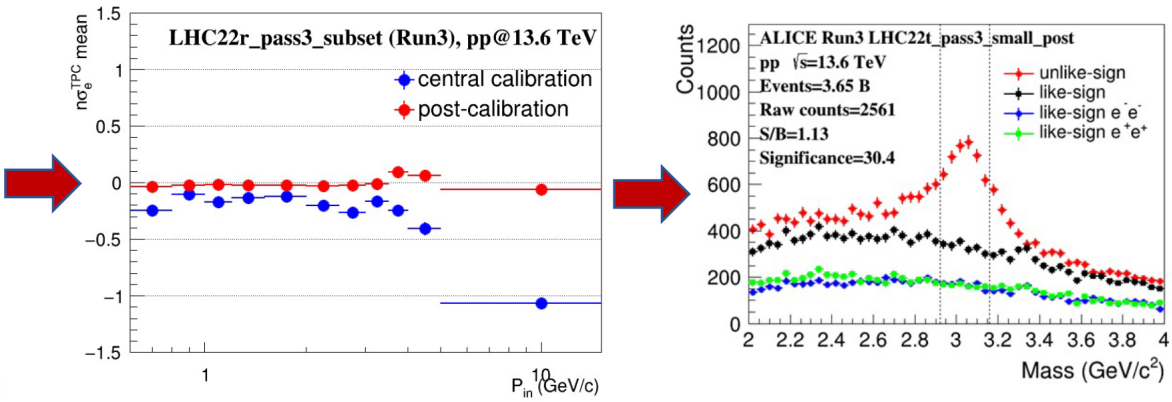


*Figure 5.4: A continuation of figure 5.3. The fit values are then used to improve PID by changing the n$\sigma$ values using equation 5.1. Applying the post-calibration can then be used to get a better signal extraction [16].*

The entire process of I) finding candidates, II) creating fits to find mean and width III) creating post-calibrations using equation 5.1, and IV) applying them to the data is shown in figure 5.3 and 5.4. These post-calibration maps for the different periods were an important aspect of the early work done on the new Run 3 datasets.

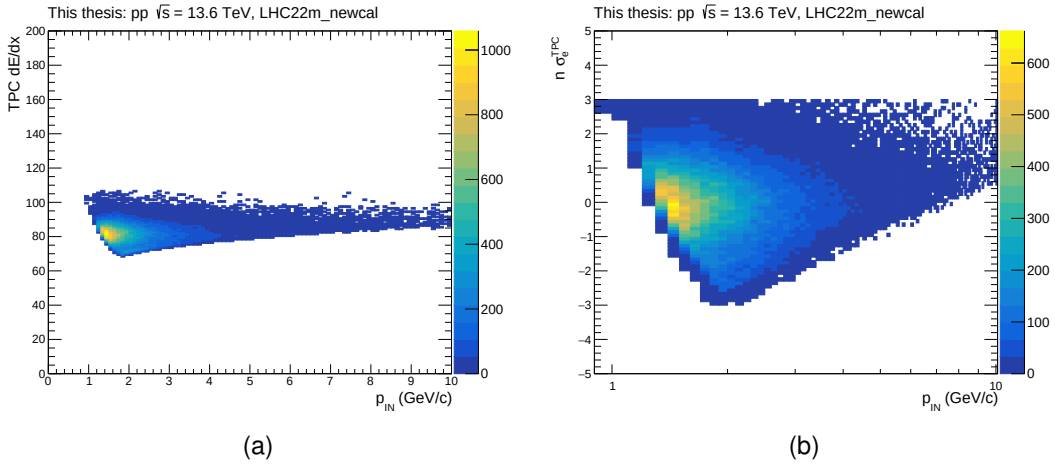


*Figure 5.5: (a) The number of particles with a given momentum that lost a certain amount of energy inside the TPC. A lot more of the particles are now located closer to the electron band (b) Showing the same as a) but using n σ. The main particle contributions are located around 0 σ from the electron band.*

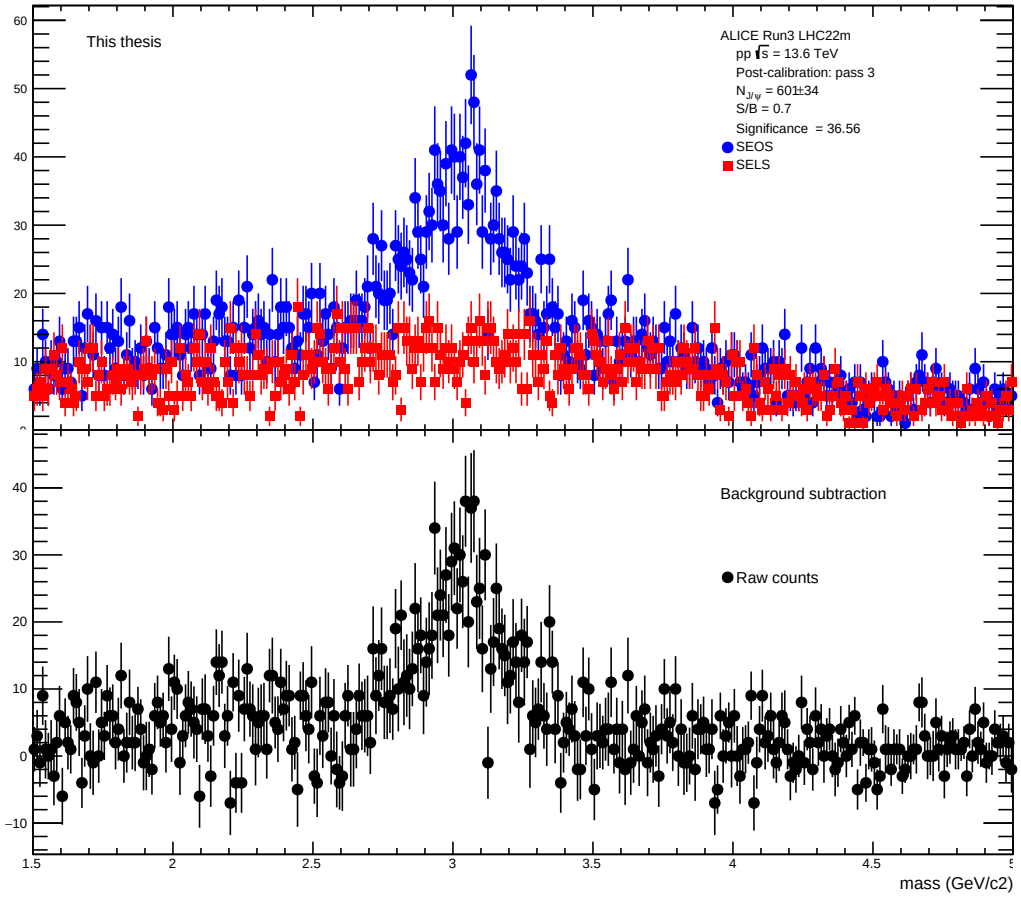


*Figure 5.6: The same LHC22 m dataset with equal cuts as before, but now with pass3 version of post-calibration applied.*

After running the post corrections over LHC22m data it is now possible to see a peak in the signal extraction area in figure 5.6. This corresponds with the much better PID

cuts shown in 5.5, where the main particle contributions now are well aligned with the electron band. This post-calibration has led to a heavy reduction in statistics of selected electron candidates, which should be background constituents if applied correctly. While the plot before the calibration says $1355 \pm 96$ in the raw count, more than twice that of the calibrated data at $601 \pm 34$, this is not to be trusted because of the large uncertainty in where the signal extraction area starts and ends. This also helps explain why the significance does not increase more between the two plots.

### 5.1.1 Smearing

When comparing early Run 3 data with Run 2, the peaks in the J/$\psi$ resonance areas are not similarly shaped. As mentioned in section 2.1, the decay channel of J/$\psi$ is tall and narrow. There is therefore a sharp dropoff from where the signal region ends when going toward a higher pair mass. There is a tail shape on the left side, when going towards lower pair mass, as a result of QED radiation leading to energy loss for some of the J/$\psi$ candidates. This is what can be seen in Run 2 data such as figure 5.7. However, for the early Run 3 data the signal region is spread over a larger area, with a smaller peak top as seen in both LHC22m from figure 5.6 and LHC22r from figure 4.7.

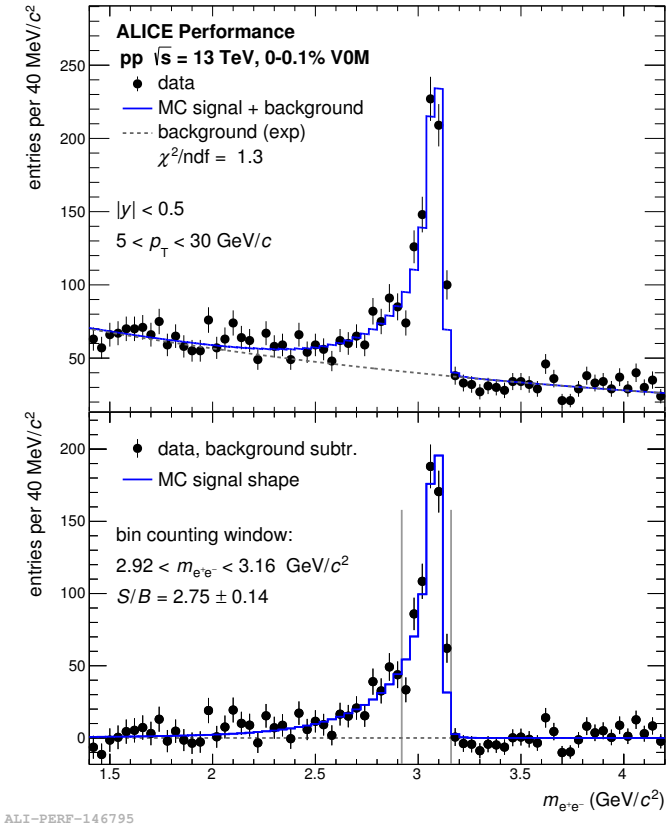


*Figure 5.7: Example of Run 2 signal extraction. Used to show how the peak in the resonance area is shaped taller and narrower than in current Run 3 data [17].*

The effect where the J/$\psi$ peak is spread over a larger mass distribution area is called smearing and is partly explained by problems with momentum resolution. This can be remedied by correcting for space charge distortions. During Run 3, the TPC works in continuous readout mode instead of a trigger-gating grid solution. A consequence of this is the backflow of ions from amplification in the GEM readout being present inside of the TPC. This leads to distortions in the otherwise uniform drift field and must be corrected for [70].

A correction for space charge distortions was applied together with the pass 4 reconstruction of the data and is shown in figure 5.8 where the sharp drop-off after the peak is now visible. This makes the signal region more narrow, and the peak therefore taller. The main reason for the poor momentum resolution is these distortions in the TPC. Distortions are small changes in the measured cluster position with respect to the true position due to space charges. The LHC22m dataset was used to test the first implementation of a space charge distortion correction.

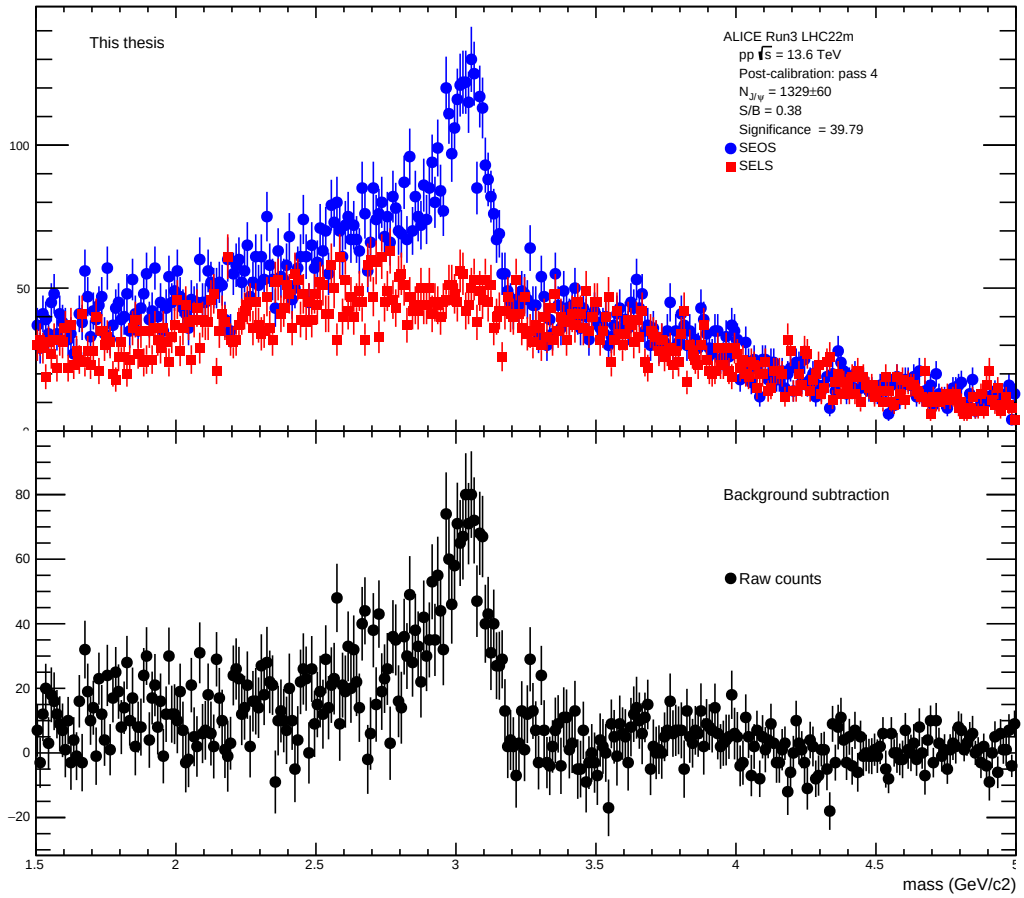


*Figure 5.8: LHC22m with an updated version of post-calibration called pass 4. The new version changes how the peak is shaped to look more like Run 2 data by introducing space charge distortion correction.*

These calibrations can be clearly seen by comparing the number of clusters and the $\chi^2$ for the respective tracks as shown in figure 5.9. The distributions show that more tracks

passed a larger amount of clusters with a lower $\chi^2$, both of which are indications of higher track quality.

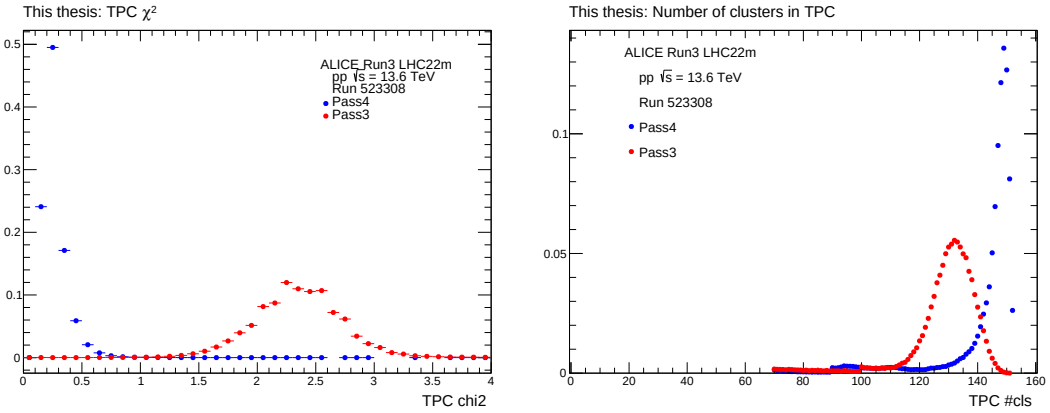


(a) (b)

*Figure 5.9: (a) The $\chi^2$ distribution of the selected tracks in LHC22m using pass3 and pass4 versions of post-calibration. Pass 4 is the version with space charge distortion corrections. (b) The distribution of the number of clusters that the selected tracks have activated in LHC22m with pass3 and pass 4 versions of post-calibration. To compare versions of post-calibration, the normalized count is used meaning all points are scaled using 1/(sum of all).*

### 5.1.2 Space charge distortion effects

Space charge distortions were introduced earlier to explain the smearing effect from a bad momentum resolution. In this section, some of the improvements from corrections to these distortions are showcased. In pass 3 roughly 90% of the tracks have zero hits in any of the ITS layers. This means that a large proportion of the statistics are removed when using the cut SPDany=true. Figure 5.10 shows the number of tracks not hitting any ITS clusters in red and tracks with a hit in at least one cluster in green, this color scheme is used for the entire section.

To create the plots used in this section, the same cuts are used as before with the exception of SPDany=true being removed. The cuts are then applied on all tracks with zero hits and then any hits separately in $O^2$ with the intention of getting a better understanding of the quality of these removed tracks, and where they originate from.

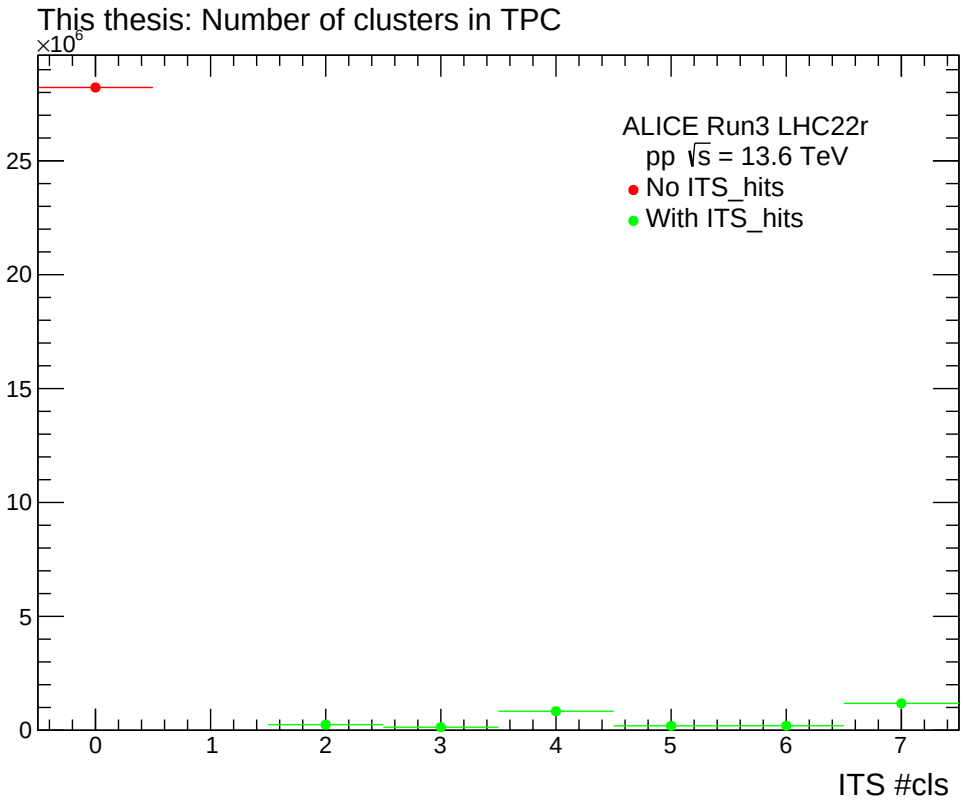


*Figure 5.10: The number of clusters in ITS per electron track before any cuts. All tracks without any hits are shown in red and are a large proportion of the total number of tracks. The tracks with at least one hit are shown in green.*

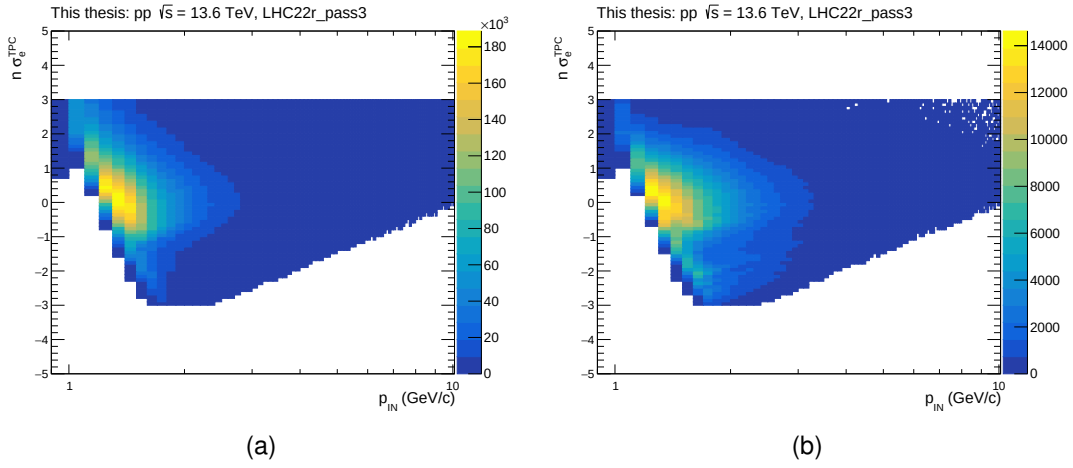


*Figure 5.11: (a) The energy loss of particles without any hits in ITS. Measured as the difference from the electron band in sigmas. (b) The energy loss of particles with at least one hit in ITS. Measured as the difference from the electron band in sigmas.*

The PID plots are shown in figure 5.11 where the tracks are identified as electrons when they reach the TPC for both cases. Therefore, it is possible that some J/$\psi$ candidates get removed. Figure 5.12 shows the pair mass plots of both tracks without and with hits in ITS.

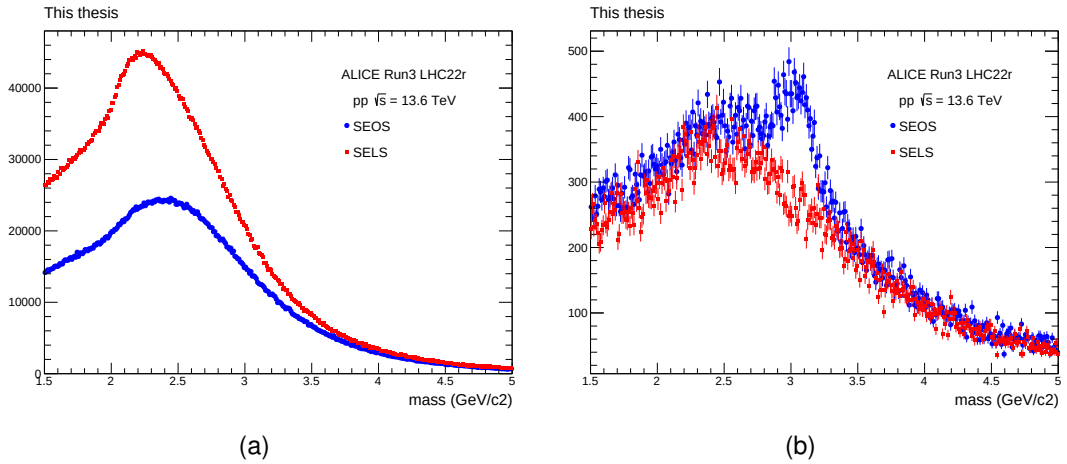


*Figure 5.12: (a) The pair mass distribution of tracks with opposite charge sign in blue and the same charge sign in red from the same events. The tracks are without hits in ITS. (b) The pair mass distribution of tracks with opposite charge signs in blue and the same charge sign in red from the same events. The tracks have at least one hit in ITS.*

Despite the PID plots showing that mostly electrons are being recognized in TPC, the quality of the data makes it impossible to find any J/$\psi$ candidates. As shown in figure 5.12 a), when looking at tracks without hits in ITS there is no visible peak in the resonance area and there is a large difference in acceptance between the LS and OS pairs. This difference in acceptance is the reason that the standard way of creating pair mass plots has not been used, as there is no real background to subtract. The acceptance difference between LS and OS is not there in tracks with at least one hit in ITS, which looks as expected for signal extraction with a peak around 3 GeV/$c^2$. The removal of tracks without a hit is therefore necessary and is not going to lead to a significant loss of good data. The tracks which do make it through ITS without hitting any clusters are still picked up in TPC where they can be studied further. The number of clusters and $\eta$ distributions is shown in figure 5.13.

The number of clusters distribution for tracks without hits in ITS shows a significant decrease in TPC hits when compared with tracks that have at least one hit in ITS. It seems there exists a correlation between the quality of tracks measured in TPC and ITS when measured by the number of clusters.

There is also a larger dependence on $\eta$ positioning for tracks without hits than is seen with at least one hit. A significant contribution of the bad tracks emerges from an $\eta$ rapidity around [0.6 - 0.9]. The same $\eta$ dependence is shown in figure 5.14, where the number of tracks with a given $\eta$ and $\phi$ is shown. The largest amount emerges from said $\eta$ positioning, but a similar dependence on $\phi$ does not emerge.

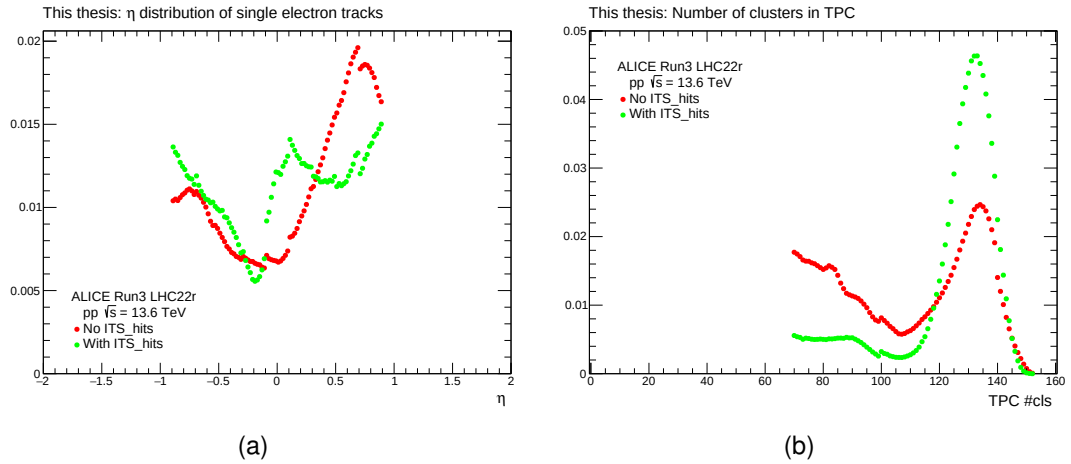


*Figure 5.13: (a) The η distribution of the different particle tracks without any hits in ITS is shown in red, while the particles with at least one hit are shown in green. (b) The tracks are distributed by the number of clusters in TPC where tracks without hits in ITS are shown in red and tracks with at least one hit are shown in green.*

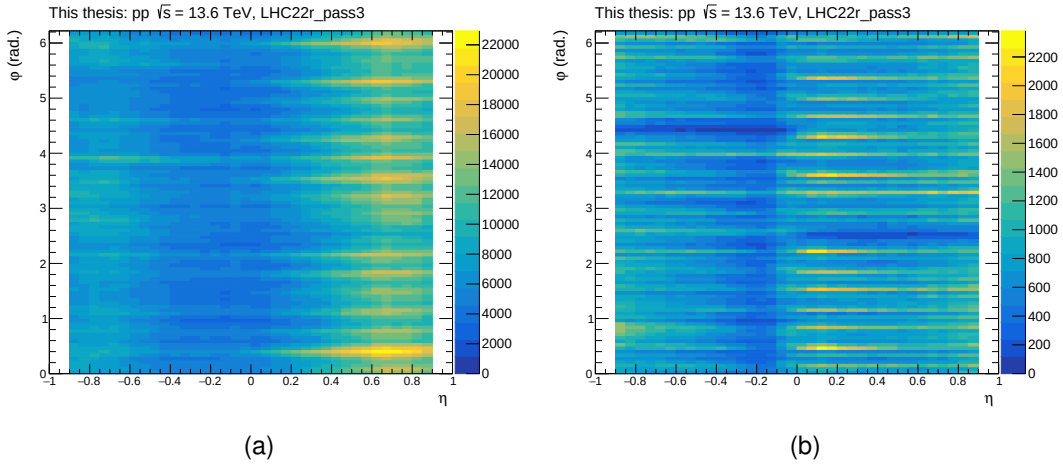


*Figure 5.14: (a) The number of tracks with a given position measured in ϕ and η directions, without any hits in ITS. (b) The number of tracks with a given position measured in ϕ and η directions, with at least one hit in ITS.*

The tracks without hits in ITS are most likely a result of space charge distortions as it leads to tracks being attributed to wrong collisions. When using the pass 4 reconstruction and including space charge distortion corrections in figure 5.15 a), the ratio between good and bad tracks is significantly improved when compared with figure 5.10. In pass 4 the bad tracks that do remain are now uniformly distributed for $\eta$ as seen in figure 5.15 b).

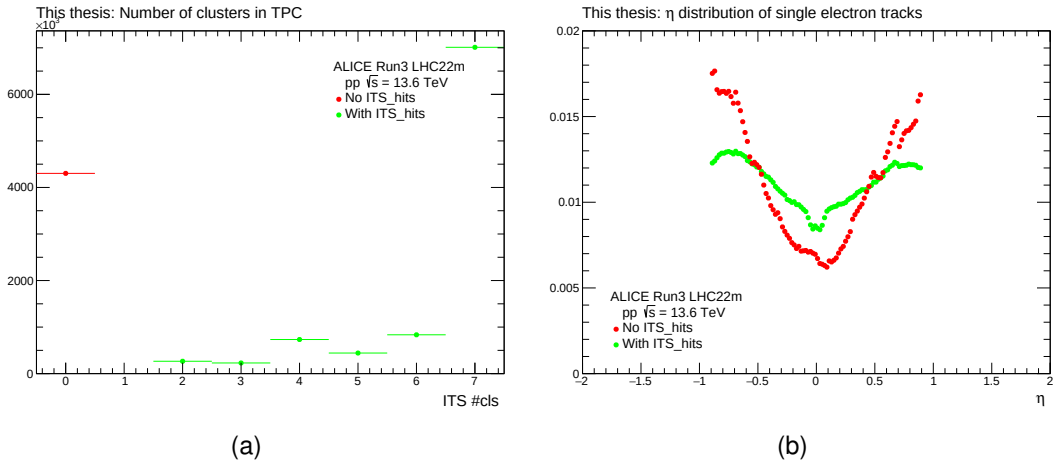


*Figure 5.15: (a) The distribution of tracks with a given amount of ITS clusters in LHC22m when using space charge distortion corrections. Tracks without hits are shown in red while tracks with at least one hit in ITS are shown in green. (b) The distribution of tracks with a given $\eta$ distribution in LHC22m when using space charge distortion corrections. Tracks without hits are shown in red while tracks with at least one hit in ITS are shown in green.*

The $\eta$ distribution shown in figure 5.15 (b) is not only more uniformly distributed for the tracks without any hits when compared with pass 3. There were problems with the $\eta$ distribution for the good tracks as well, which is unrelated to the number of hits in ITS. The space charge distortion corrections play a central role as seen in figure 5.16 where the large gathering of tracks with $\eta = 0.3$ is gone and the distribution is closer to being mirrored around 0. The small jumps that remain are a result of the post-calibrations binning being larger than the binning of the distribution itself. The pass 4 $\eta$ distribution is otherwise uniform and much closer to the expected distribution. The $\eta$ distribution is much closer to the $\eta$ distribution seen in Run 2, shown in figure 5.17, where the blue points indicating AliPhysics are the most relevant to compare with.

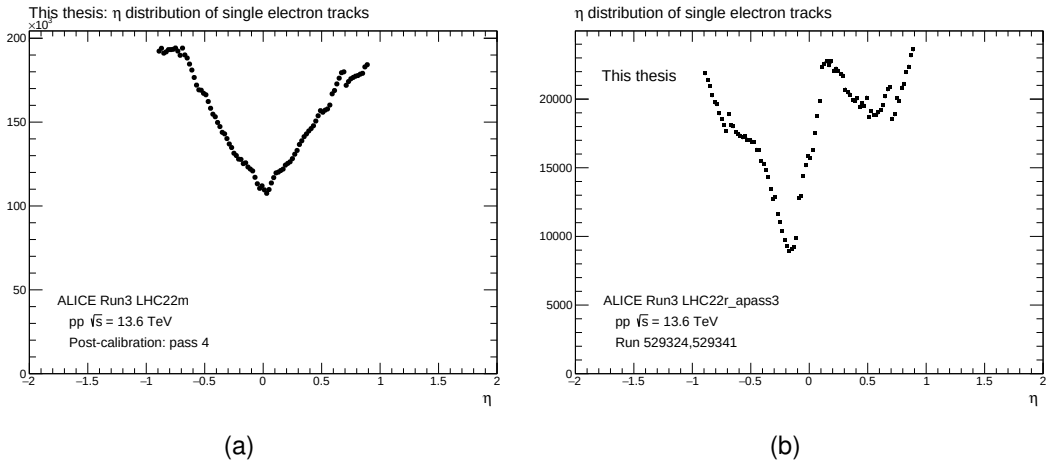


*Figure 5.16: (a) The distribution of tracks with a given η distribution in LHC22m when using space charge distortion corrections. (b) The distribution of tracks with a given η distribution in LHC22r without space charge distortion corrections.*

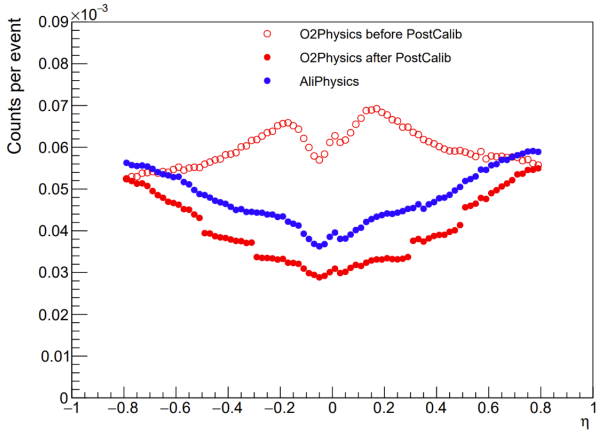


*Figure 5.17: The η distribution for Run 2 data. Here the Run 2 data have been analyzed using AliPhysics and $O^2$ with and without post-calibration, where the AliPhysics analysis in blue is the most relevant to compare with Run 3 data [18].*

## 5.2 Impact parameter studies

The measured inclusive J/ψ yield is the sum of different constituents divided into prompt and non-prompt, as discussed in section 2.1. The latter is recognized by the relatively long lifetime of beauty hadrons allowing them to travel away from the collision vertex before decaying, first into J/ψ which then decay into leptons. This allows for the separation between prompt and non-prompt through the recognition of secondary vertices. An important motivation behind the new inner tracking system is a significant improvement in resolution when looking at the Distance of Closest Approach (DCA). During track reconstruction, the paired tracks do not always end at the exact same position when traced all the way back to their origin. DCA, also called Impact Parameter (IP), is a crucial component in reconstructing secondary vertices because of the uncertainty it introduces in deciding secondary vertex positions. Figure 5.18 shows the paired tracks of opposite charges which never meet at the same origin. Instead, the

DCA is used to determine the secondary vertex, here shown displaced from the primary vertex with a distance R.

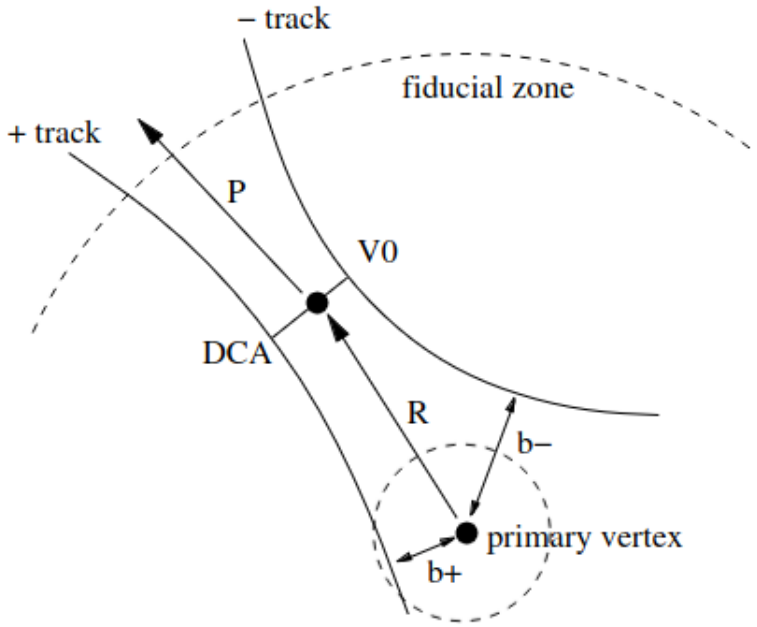


*Figure 5.18: The secondary vertex shown by the DCA between paired particle tracks away from the primary vertex [19].*

### 5.2.1 Resolution determination

The DCA can be measured in the transverse plane (xy) and along the beam axis (z). The resolution is given by

$$d_0(r\phi) = \rho - \sqrt{(x_V - x_0)^2 + (y_V - y_0)^2} \tag{5.2}$$

and

$$d_0(z) = z_{\text{track}} - z_V \tag{5.3}$$

respectively. Here, $\rho$ and ($x_0$,$y_0$) are the radius and position of the track projection center in the transverse plane. The primary vertex position is given by ($x_V$, $y_V$, $z_V$), while $z_{\text{track}}$ is the z position of the secondary vertices found using DCA in the transverse plane. Therefore, the total $d_0$ resolution is a combination of both the resolution in the track position and the resolution of the primary vertex position. The process of reconstructing secondary vertices uses a variable called pseudo proper decay length x, whose resolution depends strictly on the DCA resolution in the transverse plane. The DCA distributions are divided into different $p_{\text{T}}$ ranges and fitted using a Gaussian shape for the primary track contributions, while the long-range distribution tail populated by secondary tracks is described using a symmetrical exponential.

$$f(d_0^{xy}) = p_0\left(\frac{p_4}{\sqrt{2\pi}p_2}e^{-\frac{(d_0^{xy}-p_1)^2}{2p_2^2}} + \frac{1-p_4}{2p_3}e^{-\frac{|x-p_1|}{p_3}}\right). \tag{5.4}$$

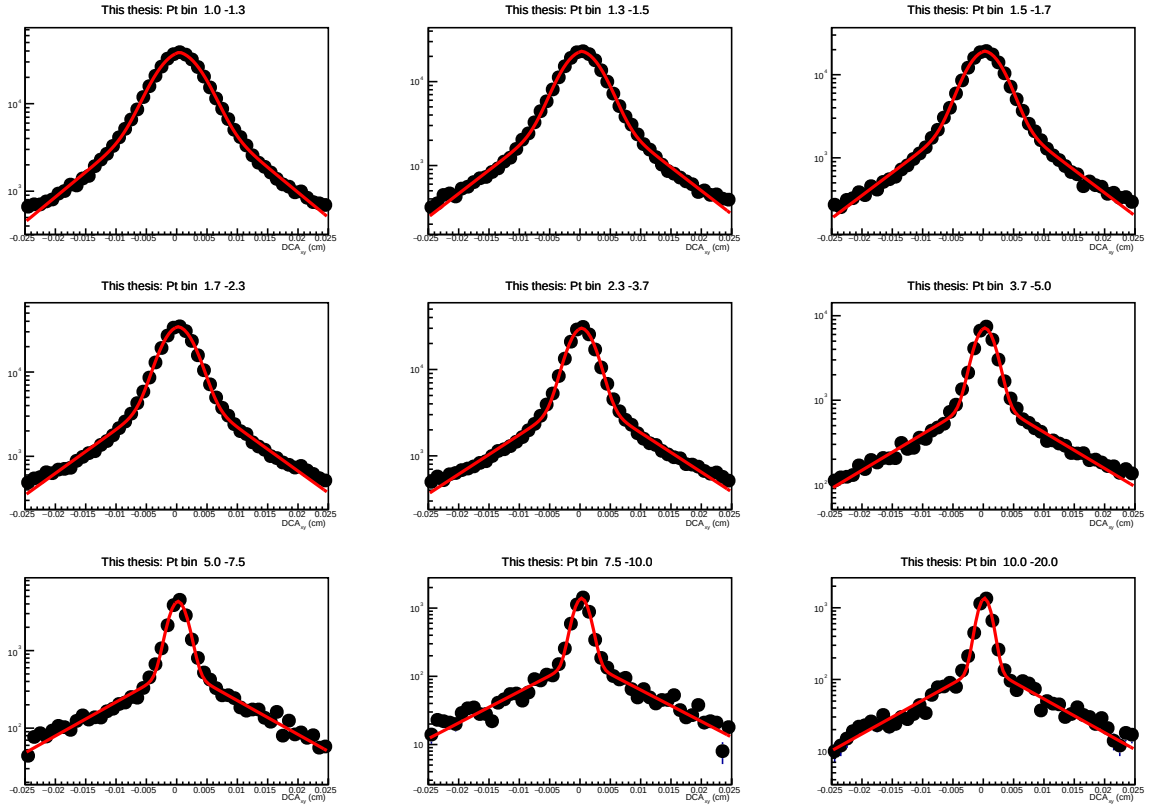


*Figure 5.19: DCA distribution in selected $p_T$ bins are fitted using a combination of a Gaussian and a symmetric exponential.*

From the fit, it is possible to approximate the resolution (RMS) and the average DCA values in the given $p_{\mathrm{T}}$ ranges. To properly measure the resolution, the DCA bins must be smaller than the resolution that is studied. From the fits of the DCA distributions, it is possible to approximate the resolution (RMS) and the average DCA values in the given $p_{\mathrm{T}}$ ranges. Smaller $p_{\mathrm{T}}$ ranges give a better $p_{\mathrm{T}}$ differential description of the values. Due to the available statistics which decrease moving towards high $p_{\mathrm{T}}$ , the widths of the $p_{\mathrm{T}}$ intervals can be smaller at low $p_{\mathrm{T}}$ .

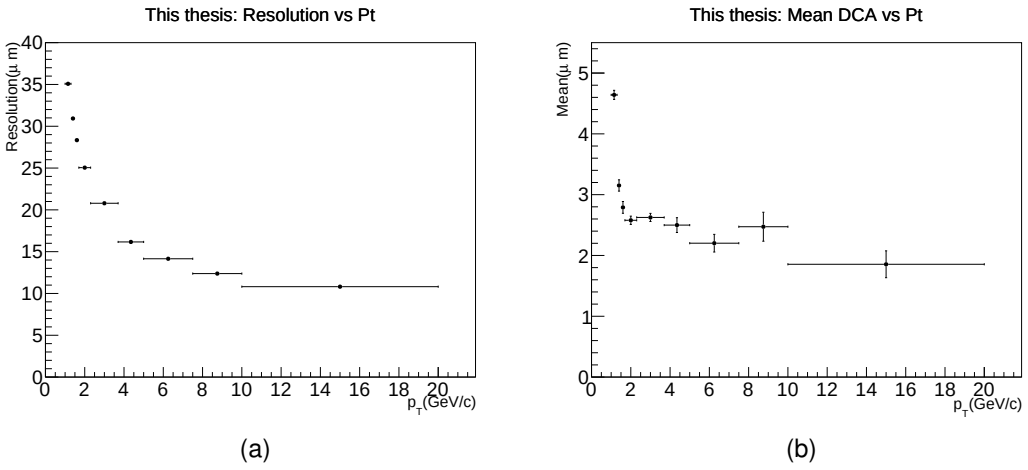


*Figure 5.20: (a) The RMS dependence on $p_T$ in the xy direction for LHC22r. (b) The mean values of DCAXY for the distributions shown in 5.23.*

The right panel of figure 5.20 shows the $p_{\mathrm{T}}$ dependent mean value for the DCA, which is expected to decrease with increasing $p_{\mathrm{T}}$. However, due to lacking statistics, it is not clear from the points in the current binning. One possible solution could be merging bins such as from 5 GeV/$c$ to 10 GeV/$c$ together into one $p_{\mathrm{T}}$ bin. It is also possible that the fit parameters are not optimized for Run 3 data, some work was done trying to tune them in this thesis, but no better alternatives to the parameters used in Run 2 were found.

The left panel of figure 5.20 shows the resolution in cm with a much more clear dependence on $p_{\mathrm{T}}$. The resolution is the highest at 1 GeV/$c$ and quickly lowers for increasing $p_{\mathrm{T}}$. This relationship is primarily attributed to Coulomb multiple scattering, mainly affecting low-momentum tracks. This is the value that is the most interesting when studying secondary vertices, as it tells us more about the quality of the data. One way to check this specific dataset is by comparing it with a run from another period, LHC22m. Because of this run's low statistic, it is impossible to use the same $p_{\mathrm{T}}$ bins as used over when looking at LHC22r runs. Instead, the bins [1,2],[2,3],[3,4], and [4,5] are used for both in the comparison shown in figure 5.21.

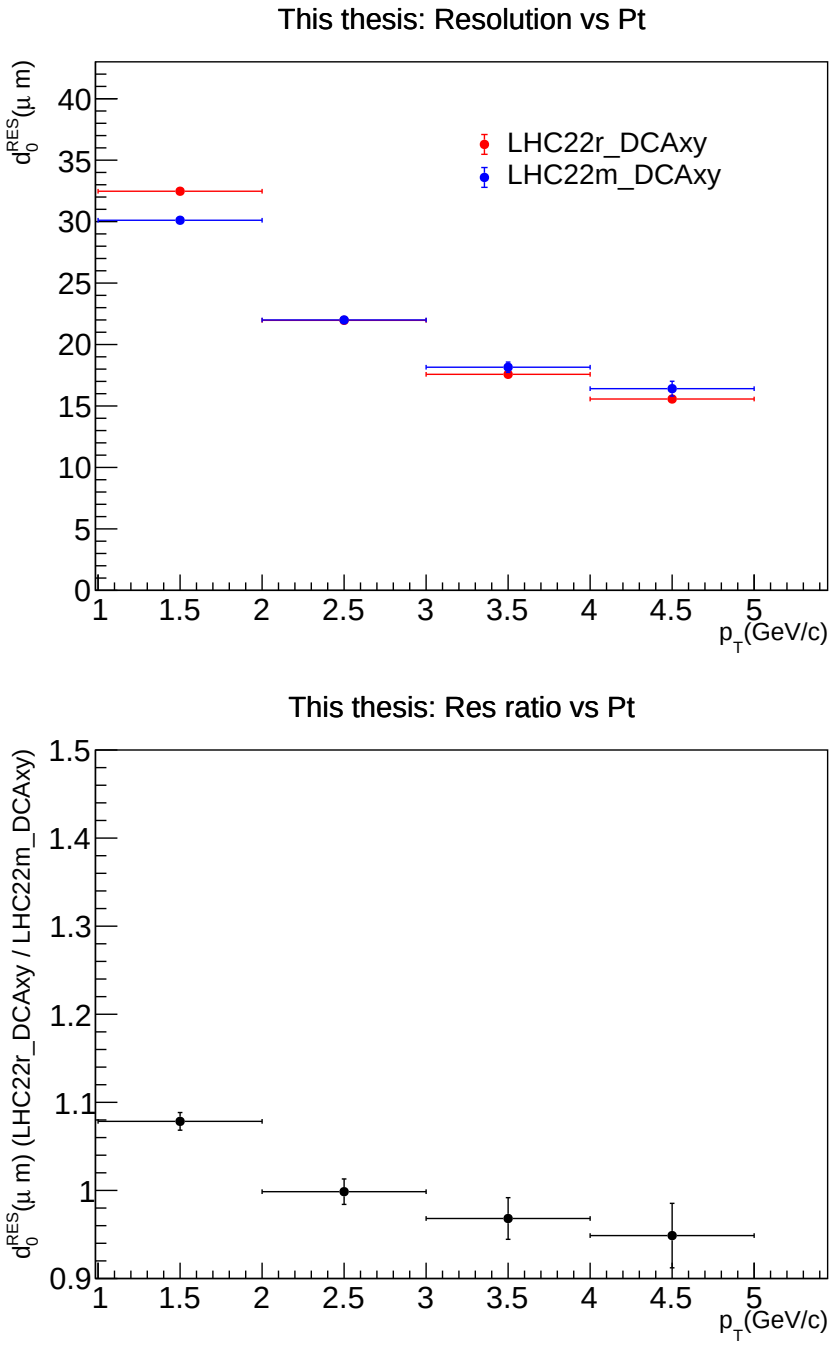


*Figure 5.21: Comparing the DCAxy resolution between the LHC22r and LHC22m datasets. The upper window compares them by showing both together, while the lower shows the ratio between them. The fit distributions used in this figure can be found in figure A.9 and A.11.*

One should note that the analyzed runs in LHC22r and LHC22m is merely a small subset of the total statistics, and one would need to include the full statistics for more accurate studies. Also, the fluctuations in mean values shown in figure 5.20 could potentially be because of problems with the fits that have been performed, increasing the inaccuracy of the found RMS values. Yet, the high amount of agreement between LHC22m and LHC22r datasets indicates that the found RMS values are in the right ballpark and that the performance of the new ITS2 can still be demonstrated using the

found RMS values in figure 5.20.

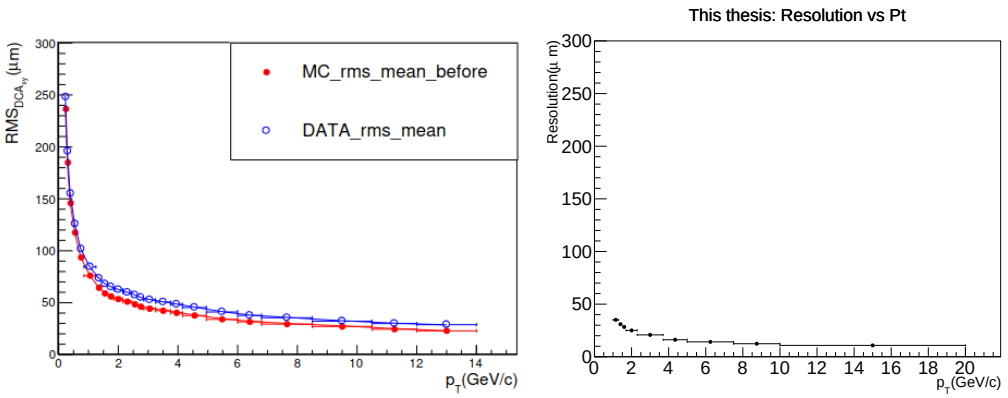


*Figure 5.22: (a) The RMS values taken from all Run 2 periods were used to compare data with monte carlo simulations [20]. (b) The RMS values of the LHC22r runs used in this thesis show the improvement in resolution compared to Run 2 data. It is the same data shown in figure 5.21 (a), but the y-axis values have been changed to be equal to the values used in the Run 2 figure.*

When comparing with the Run 2 data in figure 5.22, there are some differences in starting values (for this study, there is a $p_{\mathrm{T}}$ >1 GeV/$c$ selection, while the Run 2 study looked at charged particles above 0 GeV/$c$) and upper value (14 GeV/$c$ instead of 20 GeV/$c$). At low $p_{\mathrm{T}}$ around 1 GeV/$c$, the Run 2 RMS is around 70-80 $\mu m$ while the RMS in Run 3 is at 35 $\mu m$, roughly half of the Run 2 value. When looking at higher $p_{\mathrm{T}}$ it is slightly harder to read exact values but it is possible to say that in the area around 8 GeV/$c$ to 10 GeV/$c$, the Run 2 data is above 30 $\mu m$ while Run 3 is below 15 $\mu m$, meaning the relationship of halving the earlier resolutions is at least maintained, if not improved at higher $p_{\mathrm{T}}$. Determining the resolution values is easier to do using figure 5.20, which shows the same data. The y-axis has been changed in figure 5.22 (b) to be equal to the y-axis shown in (a).

### 5.2.2 DCAz distribution contribution

All DCA distributions looked at so far have been in the transverse plane from the beam direction (xy), but studies in the z direction are also possible. This is often ignored as the contribution in Pb-Pb collisions because the resolution is insignificant compared to the xy resolution. This is not true when looking at pp collisions, meaning the $DCA_z$ resolution contributes to the total uncertainty in vertex position.

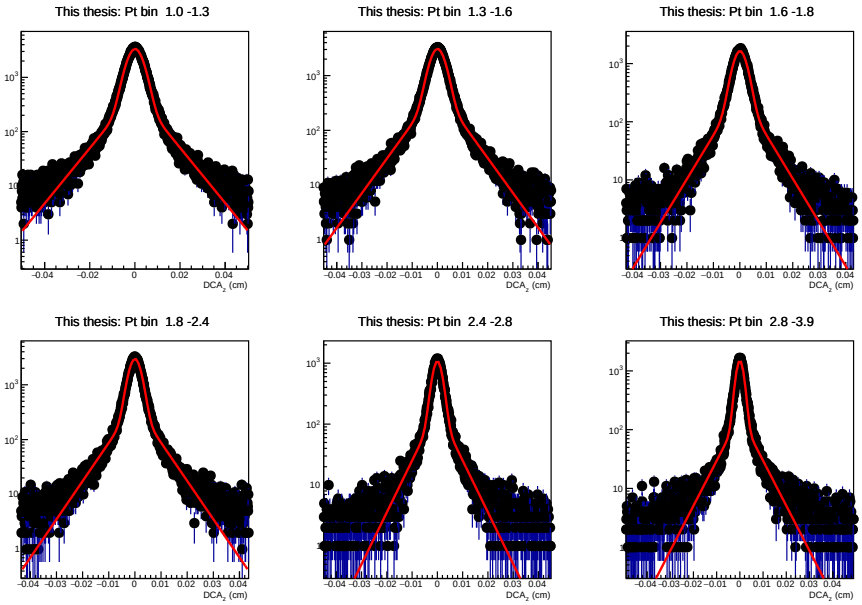


*Figure 5.23: The track distribution for DCA along the beam axis (z) for LHC22r.*

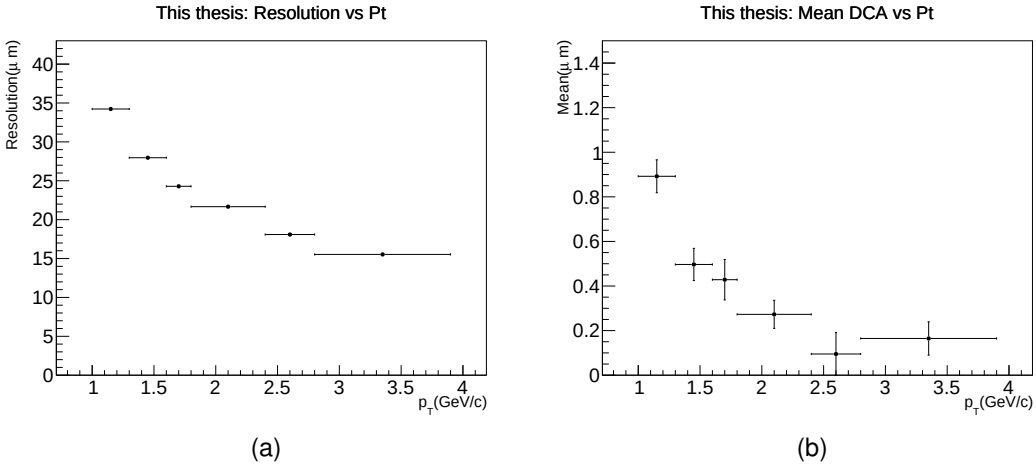


*Figure 5.24: (a) The RMS dependence on $p_T$ in the z direction for LHC22r. (b) The mean values of DCA for the distributions shown in 5.23.*

The distributions shown in figure 5.23 were created using a higher amount of binnings than in DCAxy studies for the different $p_T$ bins to do a fit while keeping the bins small enough to determine the dependence of the resolution on $p_T$ as shown in figure 5.24. The increase in binning gives a wider tail distribution, making it harder for the fit to describe it fully. The difficulty in creating fits made it harder to compare LHC22r and LHC22m to check if the resolution is consistent, as it requires the same $p_T$ bins to be fitted. Still, the two $p_T$ bins that are looked at in figure 5.25 at least shows good agreement between the two datasets.

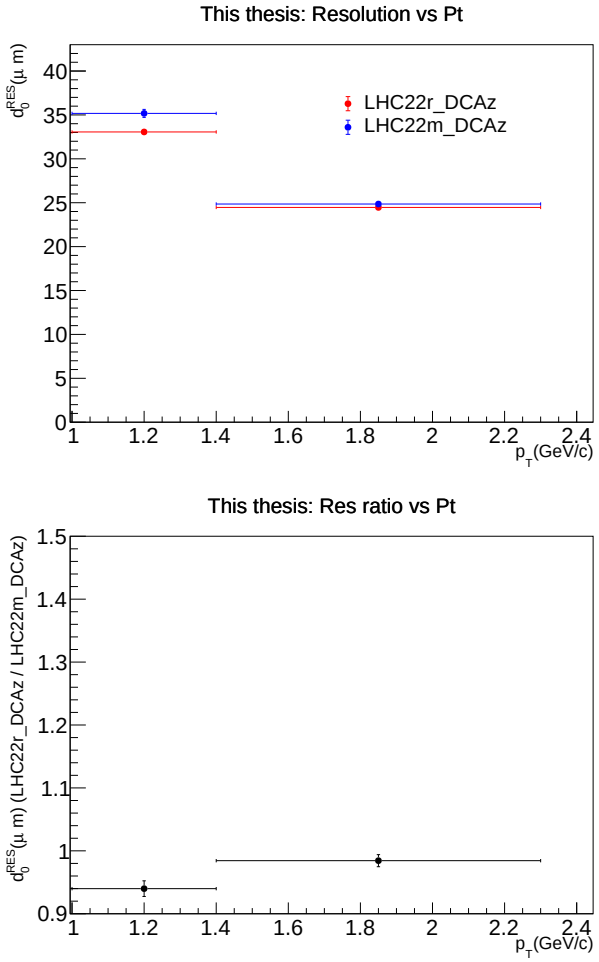


*Figure 5.25: The $DCA_z$ resolution for both LHC22r and lhc22m compared. The upper panel shows them both together, while the lower panel shows the ratio between them. The fit distributions used in this figure can be found in figure A.13 and A.15.*

### 5.2.3 DCA resolution results

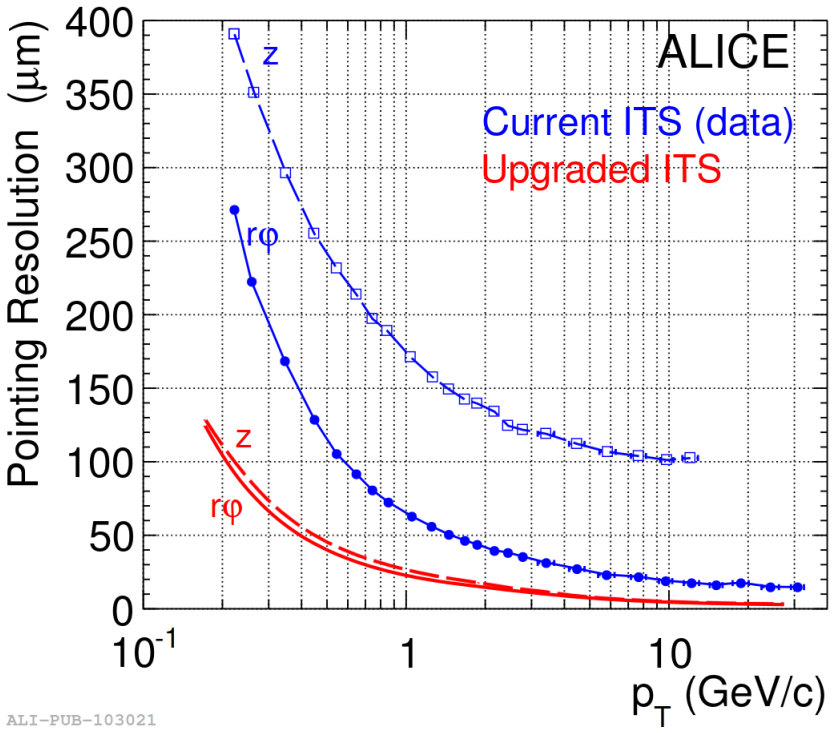


*Figure 5.26: Impact parameter resolution in both transverse plane (full lines) and longitudinal directions (dashed lines) as a function of $p_T$. The resolution for the upgraded ITS is projections created before Run 3. The upgraded ITS is shown in red, old ITS is shown in blue [21].*

Figure 5.26 shows the projected resolution from before Run 3 started. It predicts that the upgraded ITS resolution in the transverse plane should be roughly half of the old equivalent ITS values. This is in agreement with the results shown in figure 5.22. At 1 GeV/$c$, the projected DCA is around 25 $\mu$m which is lower than the roughly 35 $\mu$m found in this thesis for the LHC22r dataset.

The size of the $p_T$ bins plays a role in accurately determining the resolution for a given $p_T$, making it difficult to compare the resolution in the z-direction. Another prediction for the upgraded ITS is that the difference in resolution between the xy plane and the z direction is reduced significantly. Starting with LHC22r, the comparison shown in figure 5.27 a) shows that there is a relationship between the resolutions with a difference around 10% for low $p_T$ and the difference increasing to around 20% at the highest. This is a larger difference than what the projections show, and it was predicted higher resolution for the z direction, opposite of what is found here. The z values are much closer to the projected data, indicating that the found xy resolution is too high.

The same fit parameters are used for the LHC22m dataset in figure 5.27 b) but with different $p_T$ bins. As projected, the relationship is closer than what is found in the LHC22r dataset. Still, both xy and z resolutions are higher than the predicted 25 $\mu$m for 1 GeV/$c$.

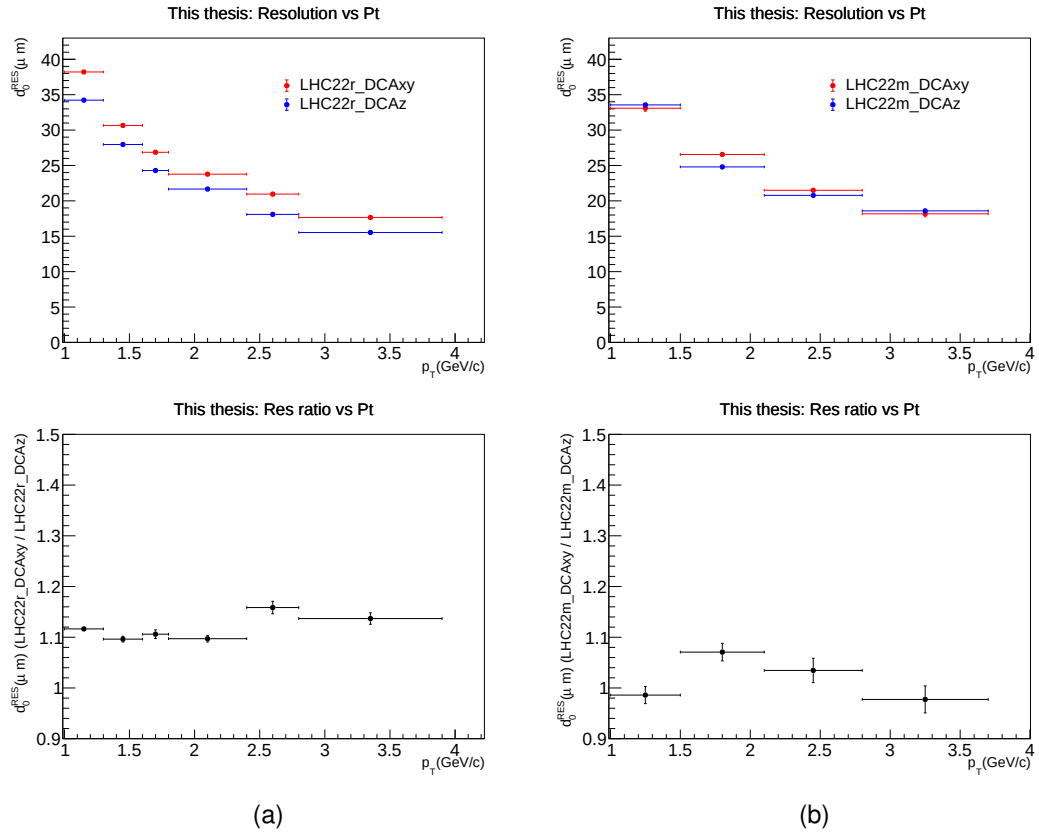


*Figure 5.27: (a) The comparison between LHC22r DCA in the xy and z directions. The upper panel shows both xy and z together, while the lower panel shows the ratio between them. The fit distributions used in this figure can be found in figure A.17 and A.19. (b) The comparison between LHC22m DCA in the xy and z directions. The upper panel shows both xy and z together, while the lower panel shows the ratio between them. The fit distributions used in this figure can be found in figure A.21 and A.23.*

# Chapter 6

# Results and Outlook

## 6.1 Result summary

This section will summarize the results of the analysis work presented in the thesis. In the outline of the thesis presented in section 1.3, the motivations were outlined. It describes some of the most relevant upgrades made to the ALICE experiment that have been tested.

- The new $O^2$ framework is designed to perform both the recording and later processing of the data. While not directly tested, it is the framework used for analysis in this thesis and some of its functionalities have been showcased.
- Can the new TPC handle the massive increase in data per second with its new GEM technology?
- The ITS2 is designed to significantly increase tracking performance. Is this improvement reflected in the impact parameter resolution?

The $O^2$ analysis framework is used to produce all Run 3 data shown in this thesis. While being downloaded locally it is able to assimilate both changes made centrally such as post-calibrations and user-specific changes such as the cuts for zero hits in ITS or increasing the binning in the DCAz plots that were made in this thesis. When running an analysis, it is capable of doing multiple cut settings simultaneously, useful when wanting to compare something such as hits and no hits in ITS or comparing different reconstruction passes and the application of post-calibrations.

The understanding of how the ALICE experiment handles the increase in data from LHC is presented by comparing it with similar Run 2 data. In particular, signal extraction of the J/$\psi$ meson because of its importance as a testing probe. For the data first presented it is not possible to determine anything because of the data quality. Post-calibrations were designed to improve PID and corrections for space charge distortions were applied to reduce the distortion effects caused by the new GEM system.

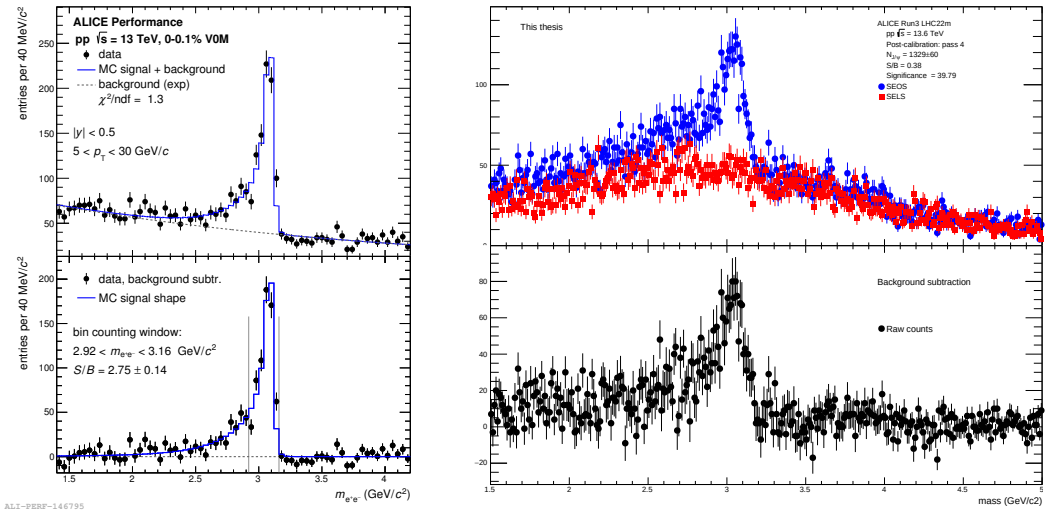


(a) (b)

*Figure 6.1: (a) Run 2 signal extraction [17]. The same plot is shown in figure 5.7. (b) Run 3 signal extraction. The same plot is shown in 5.8.*

The J/$\psi$ resonance area is supposed to be tall and narrow around 3 GeV/$c^2$, with a sharp dropoff towards higher pair masses, and a tail distribution towards lower. When comparing Run 2 and 3 data in figure 6.1 this can be seen for both. The Run 3 data is still more affected by smearing. The peak is wider, with a less steep dropoff on both sides. Still, the early work shows that reconstructing J/$\psi$ is possible with the new data. Correction to space charge distortions also led to improvement in the $\eta$ distribution and ITS number of cluster plots that were abnormal for Run 3 data. The number of clusters in TPC is significantly increased and the tracks having lower $\chi^2$ values are also shown.

The tracking performance of ITS2 has been tested using impact parameter studies. Both LHC22m and LHC22r were used to show the agreement between the found resolution of the datasets. Run 2 and Run 3 are then compared in figure 5.22, where the resolution is shown to be roughly half in ITS2. This is well aligned with the projected resolution shown in figure 6.2 (a). Here both DCA z and xy for LHC22r are shown and the axes of (b) are changed to be equal for both plots.

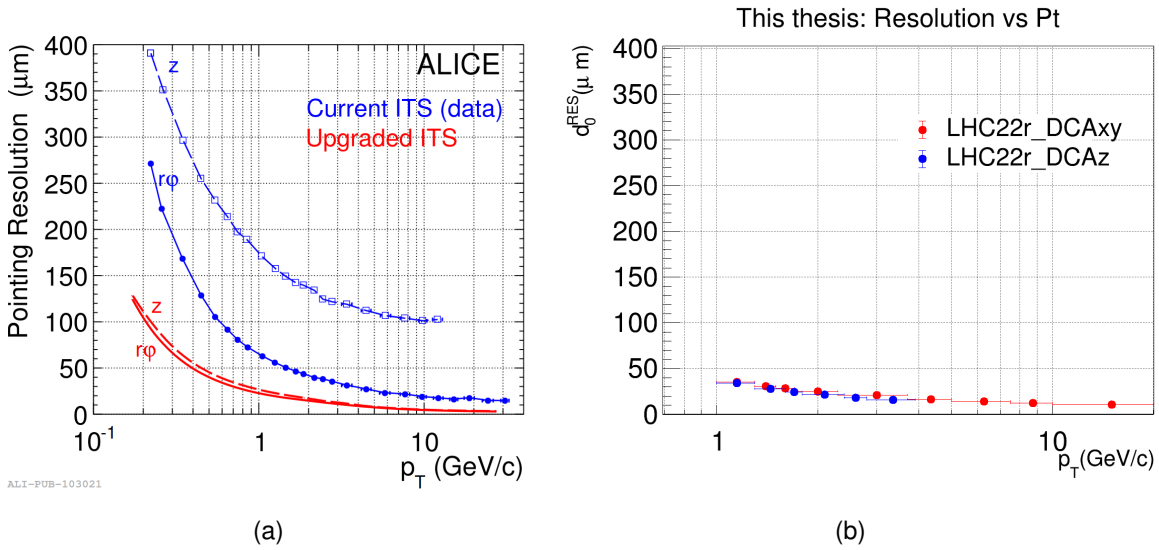


*Figure 6.2: (a) The projected DCA resolution for Run 3. (b) DCA resolution for LHC22r. The data is the same as shown in the left sides of figure 5.20 and 5.24 but here the Y and X axis has been changed to be equal to the axis shown for the projected data.*

The predicted resolution goes from around 25 $\mu$m at 1 GeV/$c$ to below 10 $\mu$m at 10 GeV/$c$, while the measured resolution goes from 35 $\mu$m to roughly 10 $\mu$m in the same interval. This means that the resolution is below expected, but still greatly improved from Run 2. The DCAz and DCAxy that were significantly different in Run 2 are now as predicted, nearly equal.

## 6.2 Conclusion and Outlook

Currently, a data skimming campaign is ongoing in order to reduce the amount of data stored from the 2022 data taking. An online selection of specific events is performed by triggering on physical observables such as the J/$\psi$. This is done to make room for the upcoming data taking in the following years. J/$\psi$ are triggered for collisions where at least two tracks pass an open electron cut selection. Solid knowledge of which electrons to keep is therefore important. This requires a good understanding of the data and detector performance, especially with regard to PID and momentum resolution. Post-calibrations and space charge distortion corrections play a key role here. The PID after post-calibration is compatible with what was achieved during Run 2. However, there is still room for further improvements to achieve a momentum resolution similar to what was achieved during Run 2.

When it comes to statistics, the full data collected during 2022 is already larger than the full Run 2 pp data sample, and it is therefore expected that the results from Run 3 will have significantly improved statistical uncertainties. One also expects to be able to perform analysis of new observables requiring more statistics than what was available during Run 2. Examples of such observables are the $\psi$ (2S) cross section measured at mid-rapidity and measuring the J/$\psi$ polarization at mid-rapidity.

The upgrade of the ITS now provides better resolution than what was achieved during Run 2. Further studies of the IP with the full available statistics are needed to give an accurate estimate of the improvement. This is important later when the data is compared with MC. The MC simulations will undergo a smearing procedure to better describe the data that is based on the estimated resolutions. These MC samples can then be used to accurately describe the $J/\psi$ signal shape used for fitting as discussed in section 4.5.

When the full statistics are fully understood and available for Run 3 it will provide deeper insights into high-density QCD for both heavy and light collisions. Here are some physics goals where ALICE and its upgrades play a central role. A much more detailed discussion of future physics goals can be found in the LHC report [71] and the ALICE collaboration note [72].

- Further insights into QGP properties such as the temperature in early stages are measured with much higher precision because of the reduced background from charm decays and photon conversions in ITS2.
- The constituents of QCD matter such as partons can be investigated at higher precision to further gain insight into their nature and length scales. Quarkonium measurements play a key role here, as their production gives insight into mechanisms such as melting and regeneration.
- During Run 3 it will be possible to study observables in both light and heavy collision systems at the same multiplicity because of the increase in luminosity and high-multiplicity pp collisions. This is an important step in unifying the current understanding of QCD particle production in light and heavy collision systems.

# Appendix A

# DCA figures

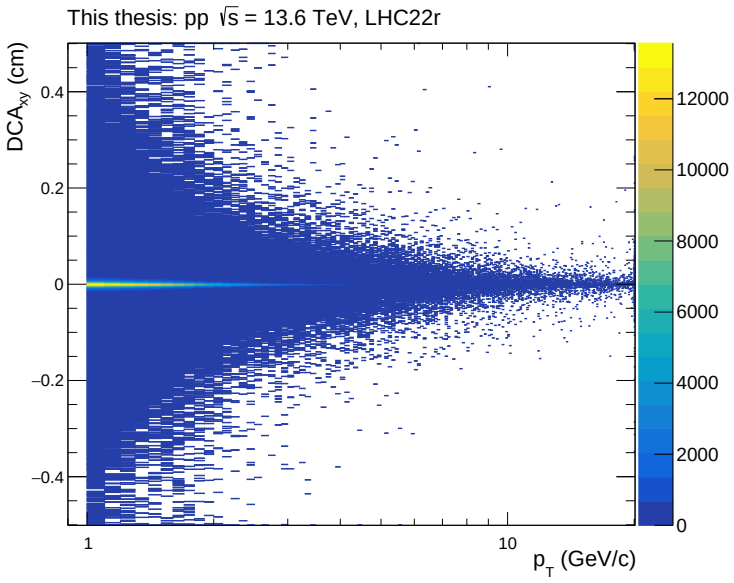


*Figure A.1: DCAxy distribution against $p_T$ for LHC22r with low binning.*

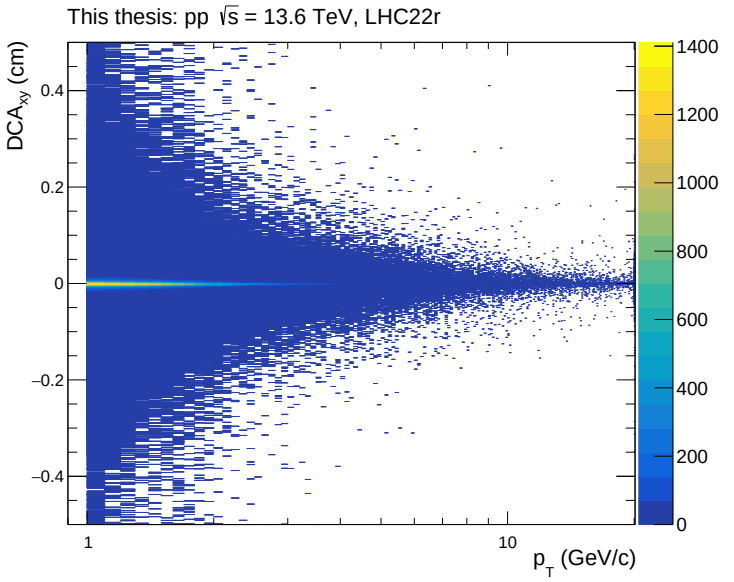


*Figure A.2: DCAxy distribution against $p_T$ for LHC22r with high binning.*

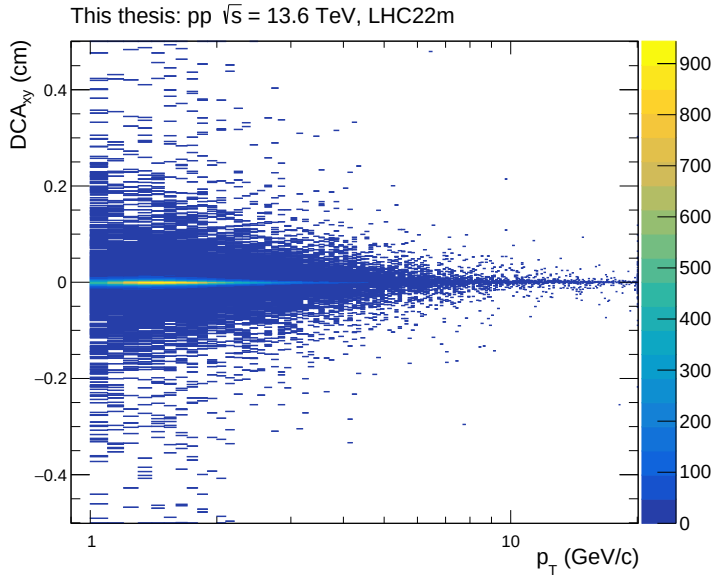


*Figure A.3: DCAxy distribution against $p_T$ for LHC22m with low binning.*

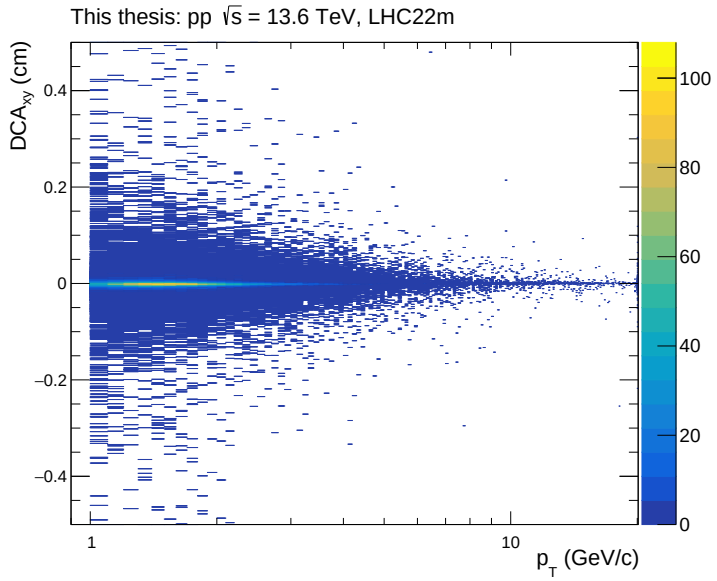


*Figure A.4: DCAxy distribution against $p_T$ for LHC22m with high binning.*

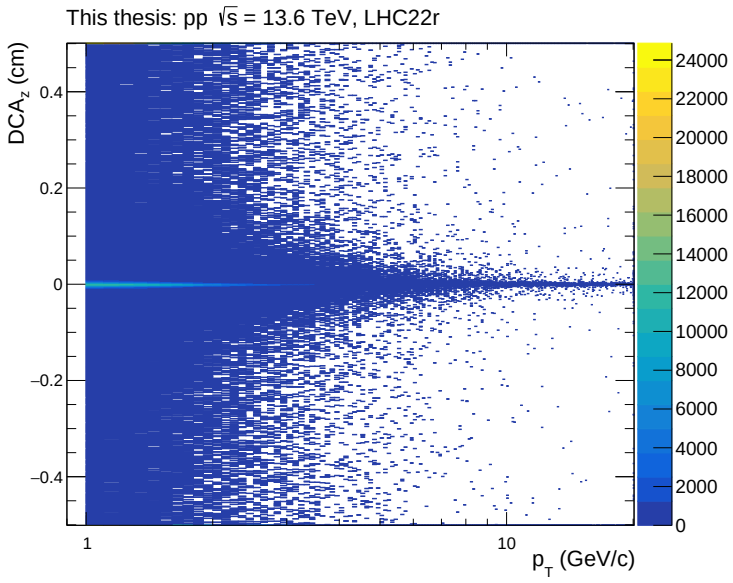


*Figure A.5: DCAz distribution against $p_T$ for LHC22r with low binning.*

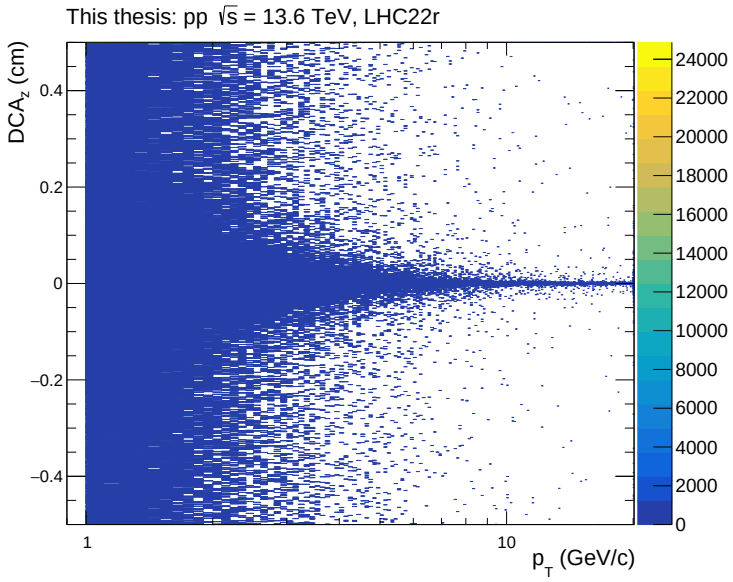


*Figure A.6: DCAz distribution against $p_T$ for LHC22r with high binning.*

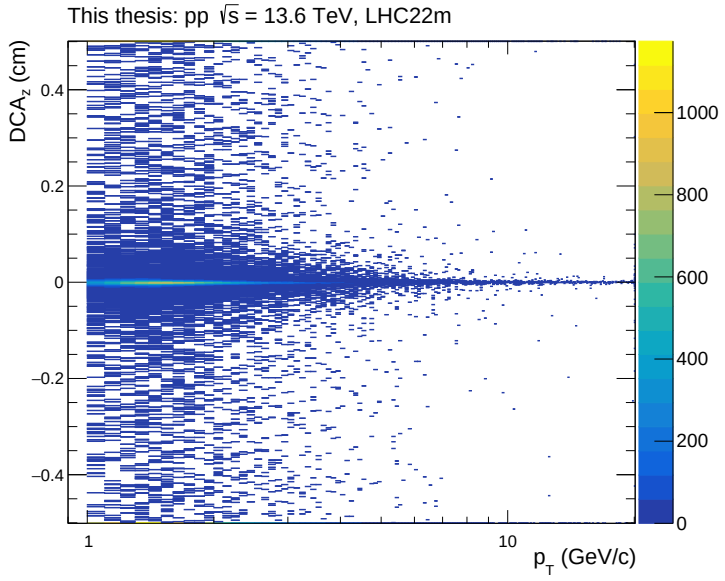


*Figure A.7: DCAz distribution against $p_T$ for LHC22m with low binning.*

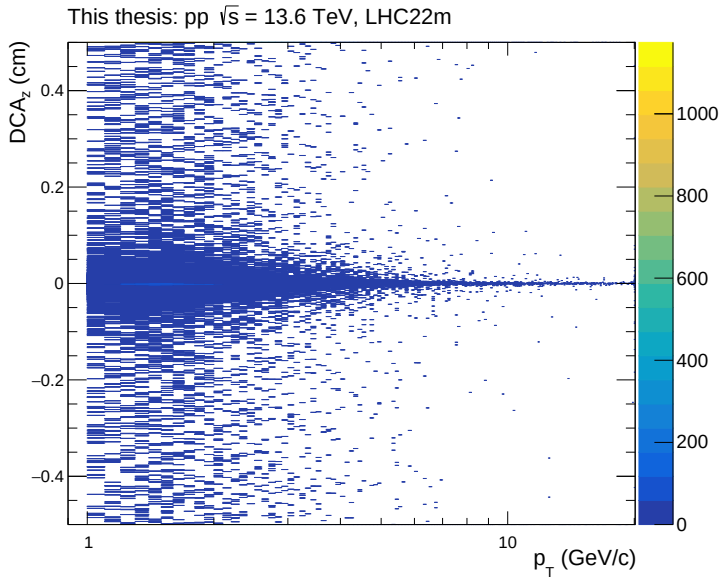


*Figure A.8: DCAz distribution against $p_T$ for LHC22m with high binning.*

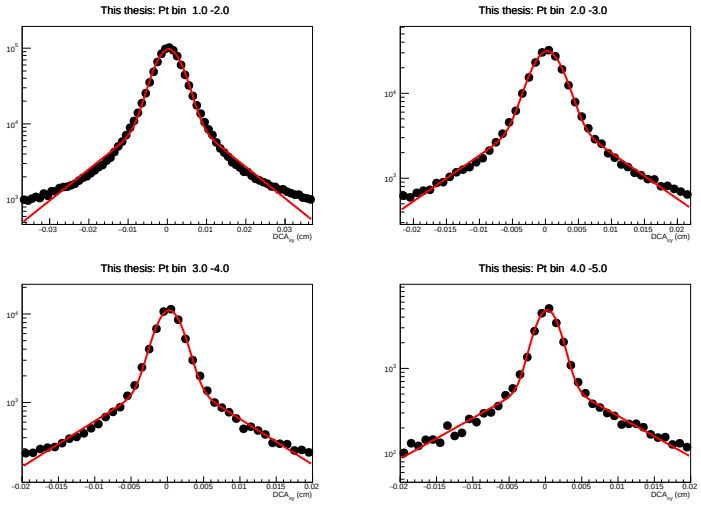


*Figure A.9: Fits of DCAxy distributions of LHC22r used in 5.21*

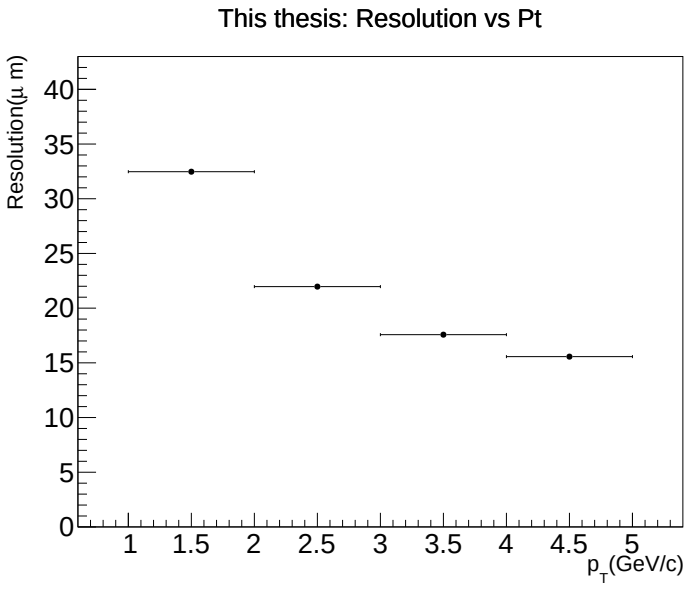


*Figure A.10: RMS of the fitted LHC22r DCAxy distributions used in 5.21*

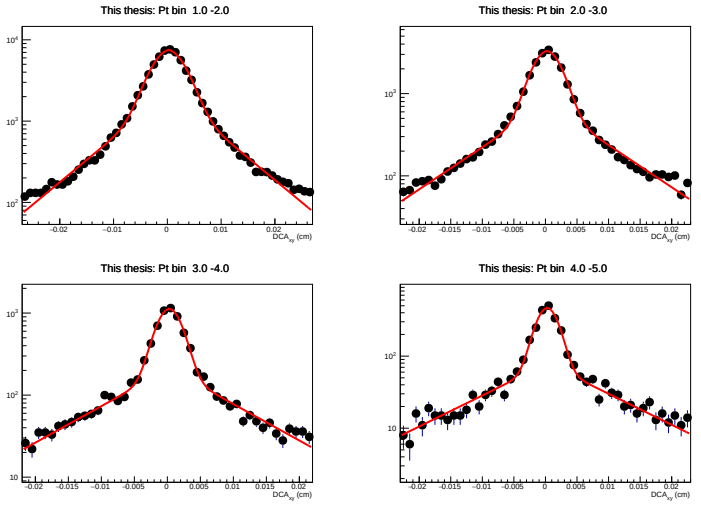


*Figure A.11: Fits of DCAxy distributions of LHC22m used in 5.21*

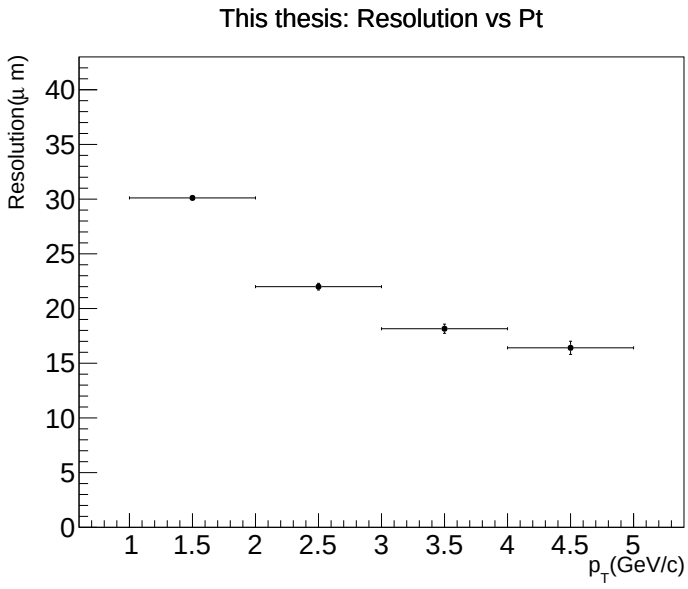


*Figure A.12: RMS of the fitted LHC22m DCAxy distributions used in 5.21*

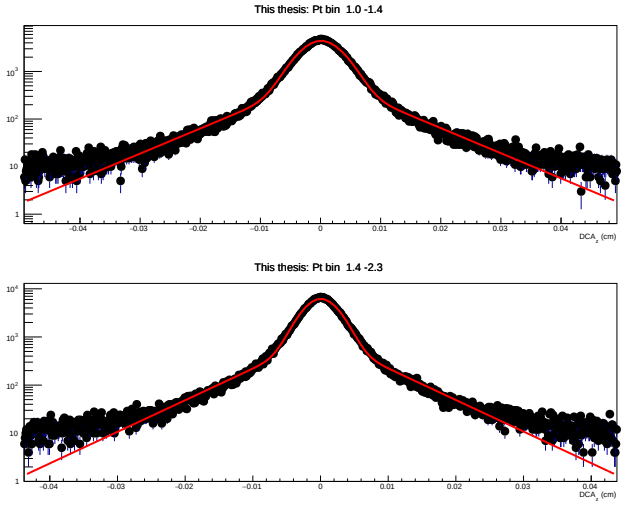


*Figure A.13: Fits of DCAz distributions of LHC22r used in 5.25*

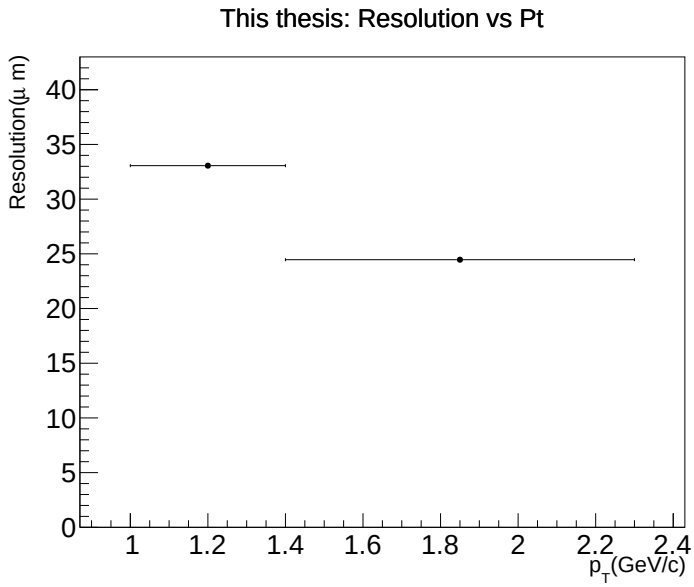


*Figure A.14: RMS of the fitted LHC22r DCAz distributions used in 5.25*

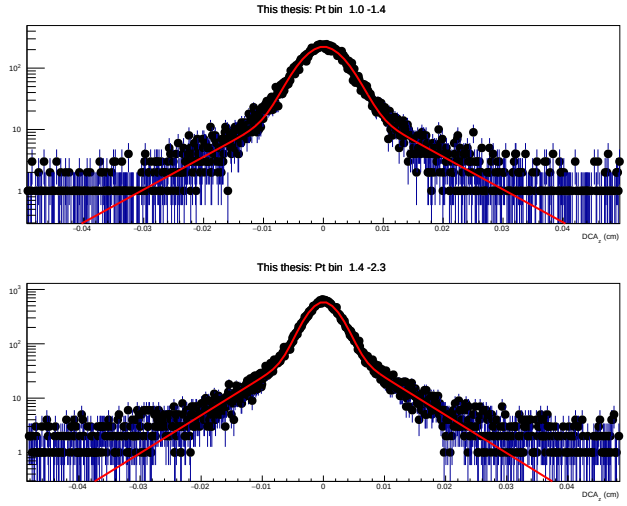


*Figure A.15: Fits of DCAz distributions of LHC22m used in 5.25*

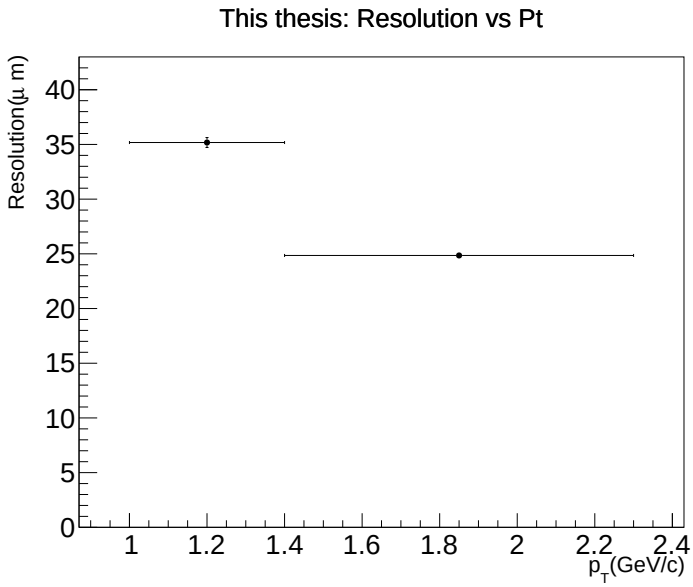


*Figure A.16: RMS of the fitted LHC22m DCAz distributions used in 5.25*

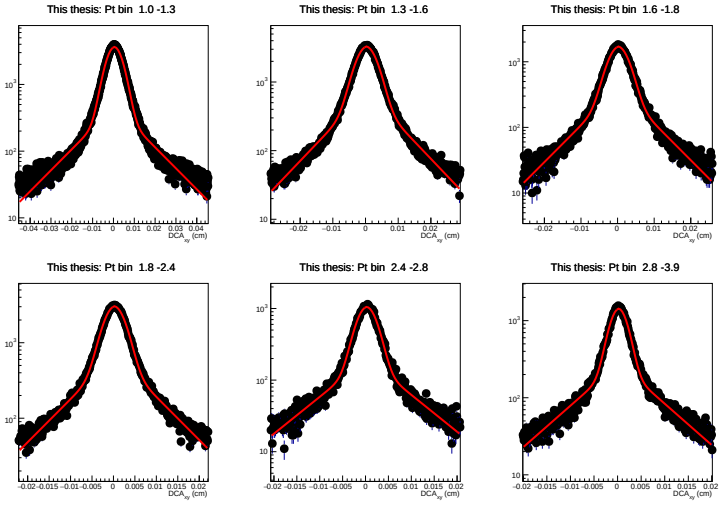


*Figure A.17: Fits of DCAxy distributions of LHC22r used in 5.27 a)*

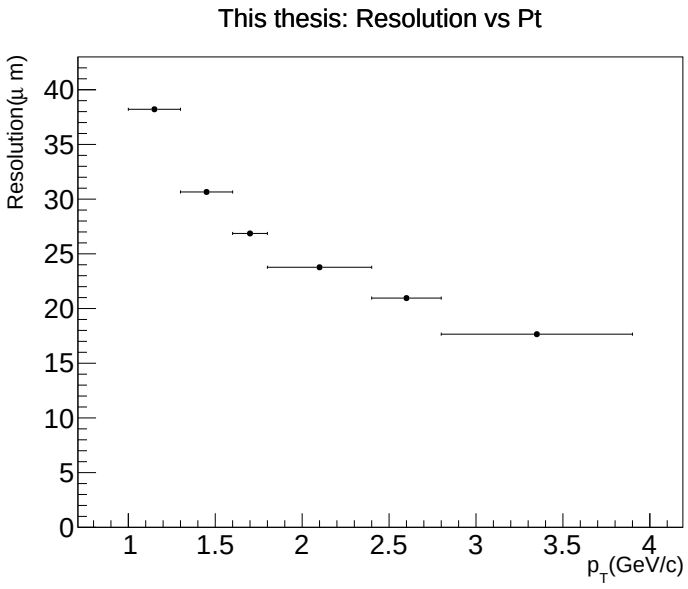


*Figure A.18: RMS of the fitted LHC22r DCAxy distributions used in 5.27 a)*

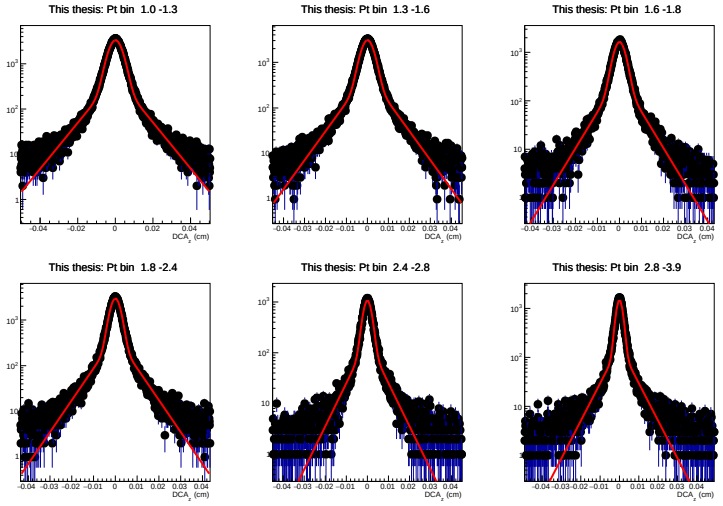


*Figure A.19: Fits of DCAz distributions of LHC22r used in 5.27 a)*

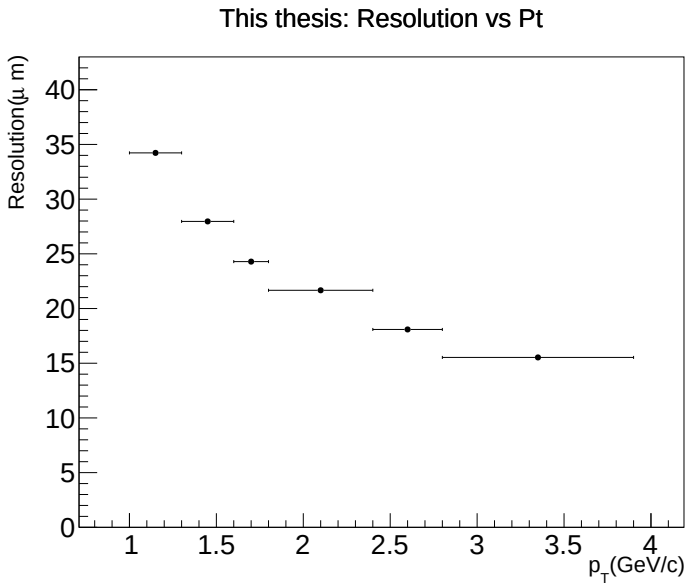


*Figure A.20: RMS of the fitted LHC22r DCAz distributions used in 5.27 a)*

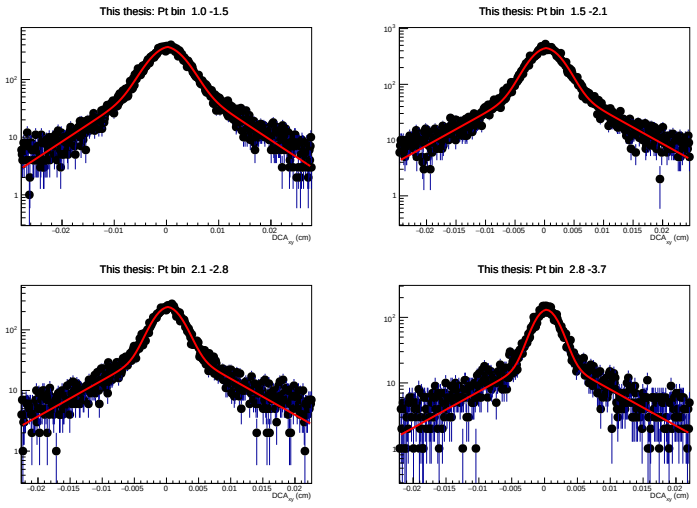


*Figure A.21: Fits of DCAxy distributions of LHC22m used in 5.27 b)*

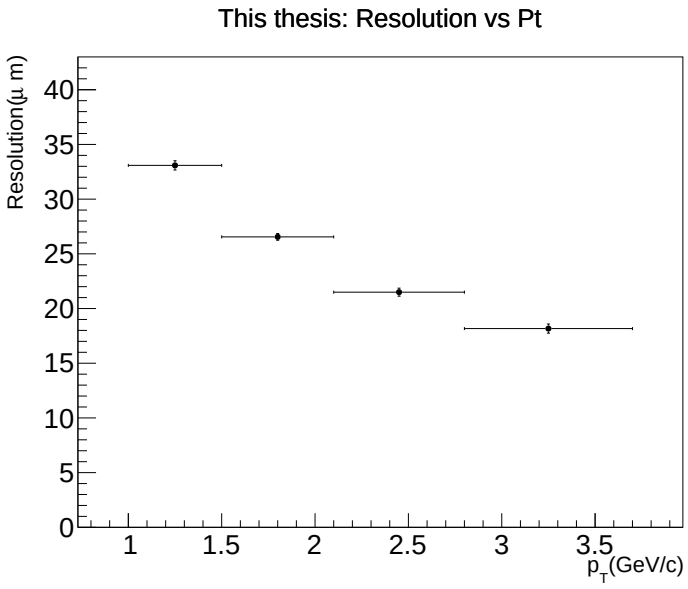


*Figure A.22: RMS of the fitted LHC22m DCAxy distributions used in 5.27 b)*

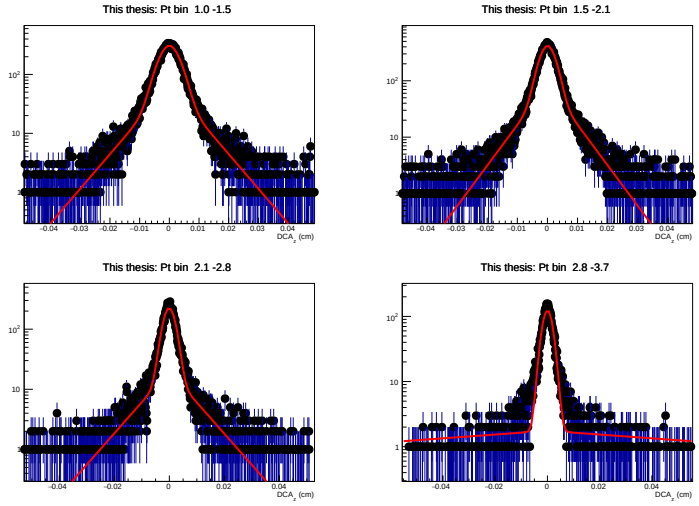


*Figure A.23: Fits of DCAz distributions of LHC22m used in 5.27 b)*

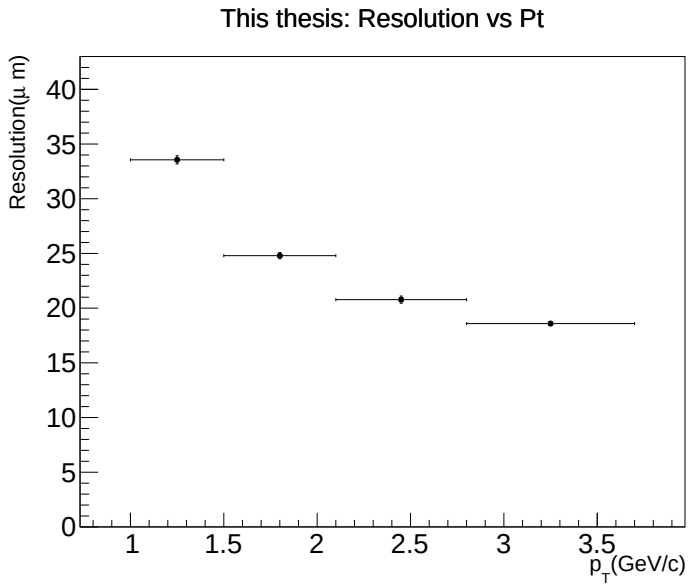


*Figure A.24: RMS of the fitted LHC22m DCAz distributions used in 5.27 b)*

# Bibliography


[1] R. L. Workman *et al.*, "Review of Particle Physics," *PTEP*, vol. 2022, p. 083C01, 2022.

[2] J. Greensite, "An introduction to the confinement problem," *Lect.Notes phys*, vol. 821, pp. 1–211, 2011.

[3] R. S. Bhalerao, "Relativistic heavy-ion collisions," in *1st Asia-Europe-Pacific School of High-Energy Physics*, 2014, pp. 219–239.

[4] ALICE, "The ALICE experiment – A journey through QCD," *CERN-EP-2022-227*, 11 2022.

[5] C. Brenner Mariotto, M. B. Gay Ducati, and G. Ingelman, "Soft and hard QCD dynamics in hadroproduction of charmonium," *Eur. Phys. J. C*, vol. 23, pp. 527–538, 2002.

[6] H.-S. Shao, "Heavy Quarkonium Production Phenomenology and Automation of One-Loop Scattering Amplitude Computations," Ph.D. dissertation, Peking U., Cham, 2016.

[7] S. Acharya *et al.*, "Energy dependence of forward-rapidity $J/\psi$ and $\psi(2S)$ production in pp collisions at the LHC," *Eur. Phys. J. C*, vol. 77, no. 6, p. 392, 2017.

[8] B. B. Abelev *et al.*, "Measurement of quarkonium production at forward rapidity in $pp$ collisions at $\sqrt{s} = 7$ TeV," *Eur. Phys. J. C*, vol. 74, no. 8, p. 2974, 2014.

[9] J. Adam *et al.*, "Differential studies of inclusive $J/\psi$ and $\psi(2S)$ production at forward rapidity in Pb-Pb collisions at $\sqrt{s_{NN}} = 2.76$ TeV," *JHEP*, vol. 05, p. 179, 2016.

[10] J.-L. Caron, "LHC layout. Schema general du LHC," 1997, aC Collection. Legacy of AC. Pictures from 1992 to 2002. [Online]. Available: https://cds.cern.ch/record/841573

[11] A. collabiration, "3d alice schematic run3 -with description," 2017, last accessed 24 May 2023. [Online]. Available: https://alice-figure.web.cern.ch/node/11220

[12] D. Colella, "ALICE Inner Tracking System Upgrade: Construction and Commissioning," *Springer Proc. Phys.*, vol. 250, pp. 485–488, 2020.

[13] J. Adolfsson *et al.*, "The upgrade of the ALICE TPC with GEMs and continuous readout," *JINST*, vol. 16, no. 03, p. P03022, 2021.

[14] S. Bysiak, "The Fast Interaction Trigger Upgrade for ALICE," *PoS*, vol. LHCP2020, p. 251, 2021.

[15] W. Yu, "Particle identification of the ALICE TPC via dE/dx," *Nucl. Instrum. Meth. A*, vol. 706, pp. 55–58, 2013.

[16] Z. X. Pengzhong Lu, "Dq v0 selector and post-calibration," 2023, last accessed 15 May 2023. [Online]. Available: https://indico.cern.ch/event/1267433/contributions/5382150/attachments/2637658/4564042/DQV0AndPostCal.pdf

[17] A. collaboration, "Invariant mass spectrum for di-electrons with pt > 5 gev/c," 2023, last accessed 15 May 2023. [Online]. Available: https://alice-figure.web.cern.ch/node/12966

[18] Y. Zhang, "Comparison between aliphysics and o2physics using converted data for j/$\psi$ to ee at mid-rapidity," 2023, last accessed 26 May 2023. [Online]. Available: https://indico.cern.ch/event/1286018/contributions/5415961/attachments/2651305/4590521/ali_vs_o2p.pdf

[19] C. W. Fabjan *et al.*, "ALICE: Physics Performance Report," *J. Phys. G*, vol. 32, pp. 1295–2040, 2006.

[20] J.-A. Sætre, ""prompt and non-prompt j/$\psi$ cross-sections in proton-proton collisions at $\sqrt{s}$ = 5.02 tev with alice"," Master's thesis, University of Bergen, https://hdl.handle.net/1956/20400, 2019.

[21] "ALICE upgrade physics performance studies for 2018 Report on HL/HE-LHC physics," *ALICE-PUBLIC-2019-001*, 2019.

[22] W. J. Marciano and H. Pagels, "QUANTUM CHROMODYNAMICS," *Nature*, vol. 279, pp. 479–483, 1979.

[23] A. Deur, S. J. Brodsky, and G. F. de Teramond, "The QCD Running Coupling," *Nucl. Phys.*, vol. 90, p. 1, 2016.

[24] N. Brambilla and A. Vairo, "Quark confinement and the hadron spectrum," in *13th Annual HUGS AT CEBAF (HUGS 98)*, 5 1999, pp. 151–220.

[25] S. Borsanyi, Z. Fodor, C. Hoelbling, S. D. Katz, S. Krieg, and K. K. Szabo, "Full result for the QCD equation of state with 2+1 flavors," *Phys. Lett. B*, vol. 730, pp. 99–104, 2014.

[26] W. Busza, K. Rajagopal, and W. van der Schee, "Heavy Ion Collisions: The Big Picture, and the Big Questions," *Ann. Rev. Nucl. Part. Sci.*, vol. 68, pp. 339–376, 2018.

[27] J.-L. Kneur and A. Neveu, "Renormalization Group Optimized Perturbation: $\alpha_S$ from $f_\pi$," *Nucl. Part. Phys. Proc.*, vol. 258-259, pp. 59–62, 2015.

[28] J. J. Aubert *et al.*, "Experimental Observation of a Heavy Particle *J*," *Phys. Rev. Lett.*, vol. 33, pp. 1404–1406, 1974.

[29] J. E. Augustin *et al.*, "Discovery of a Narrow Resonance in $e^+e^-$ Annihilation," *Phys. Rev. Lett.*, vol. 33, pp. 1406–1408, 1974.

[30] N. Brambilla *et al.*, "Heavy Quarkonium: Progress, Puzzles, and Opportunities," *Eur. Phys. J. C*, vol. 71, p. 1534, 2011.

[31] J. P. Lansberg, "$J/\psi$, $\psi$ ' and $\Upsilon$ production at hadron colliders: A Review," *Int. J. Mod. Phys. A*, vol. 21, pp. 3857–3916, 2006.

[32] G. T. Bodwin, E. Braaten, and J. Lee, "Comparison of the color-evaporation model and the NRQCD factorization approach in charmonium production," *Phys. Rev. D*, vol. 72, p. 014004, 2005.

[33] J. F. Amundson, O. J. P. Eboli, E. M. Gregores, and F. Halzen, "Quantitative tests of color evaporation: Charmonium production," *Phys. Lett. B*, vol. 390, pp. 323–328, 1997.

[34] C. E. Carlson and R. Suaya, "Hadronic Production of psi/J Mesons," *Phys. Rev. D*, vol. 14, p. 3115, 1976.

[35] R. Baier and R. Ruckl, "Hadronic Production of J/psi and Upsilon: Transverse Momentum Distributions," *Phys. Lett. B*, vol. 102, pp. 364–370, 1981.

[36] V. Papadimitriou, "Inclusive $J/\psi$, $\psi$ (2S) and $b$ quark production in $\bar{p}p$ collisions at $\sqrt{s}$ = 1.8-TeV," *AIP Conf. Proc.*, vol. 272, pp. 1086–1092, 2008.

[37] N. Brambilla *et al.*, "Heavy quarkonium physics," *CERN-2005-005*, 12 2004.

[38] G. T. Bodwin, E. Braaten, and G. P. Lepage, "Rigorous QCD analysis of inclusive annihilation and production of heavy quarkonium," *Phys. Rev. D*, vol. 51, pp. 1125–1171, 1995, [Erratum: Phys.Rev.D 55, 5853 (1997)].

[39] T. Matsui and H. Satz, "$J/\psi$ Suppression by Quark-Gluon Plasma Formation," *Phys. Lett. B*, vol. 178, pp. 416–422, 1986.

[40] F. Karsch and H. Satz, "The Spectral analysis of strongly interacting matter," *Z. Phys. C*, vol. 51, pp. 209–224, 1991.

[41] S. Digal, P. Petreczky, and H. Satz, "Quarkonium feed down and sequential suppression," *Phys. Rev. D*, vol. 64, p. 094015, 2001.

[42] A. Andronic, P. Braun-Munzinger, K. Redlich, and J. Stachel, "The thermal model on the verge of the ultimate test: particle production in Pb-Pb collisions at the LHC," *J. Phys. G*, vol. 38, p. 124081, 2011.

[43] X. Zhao and R. Rapp, "Medium Modifications and Production of Charmonia at LHC," *Nucl. Phys. A*, vol. 859, pp. 114–125, 2011.

[44] K. Zhou, N. Xu, Z. Xu, and P. Zhuang, "Medium effects on charmonium production at ultrarelativistic energies available at the CERN Large Hadron Collider," *Phys. Rev. C*, vol. 89, no. 5, p. 054911, 2014.

[45] E. G. Ferreiro, "Charmonium dissociation and recombination at LHC: Revisiting comovers," *Phys. Lett. B*, vol. 731, pp. 57–63, 2014.

[46] "LHC Machine," *JINST*, vol. 3, p. S08001, 2008.

[47] N. Dinmore, "How to train your magnets," 2021, last accessed 9 Feb 2023. [Online]. Available: https://home.cern/news/news/accelerators/how-train-your-magnets

[48] W. Herr and B. Muratori, "Concept of luminosity," in *CERN Accelerator School and DESY Zeuthen: Accelerator Physics*, 9 2003, pp. 361–377.

[49] S. Fartoukh *et al.*, "LHC Configuration and Operational Scenario for Run 3," *CERN-ACC-2021-0007*.

[50] G. Aad *et al.*, "The ATLAS Experiment at the CERN Large Hadron Collider," *JINST*, vol. 3, p. S08003, 2008.

[51] S. Chatrchyan *et al.*, "The CMS Experiment at the CERN LHC," *JINST*, vol. 3, p. S08004, 2008.

[52] A. A. Alves, Jr. *et al.*, "The LHCb Detector at the LHC," *JINST*, vol. 3, p. S08005, 2008.

[53] K. Aamodt *et al.*, "The ALICE experiment at the CERN LHC," *JINST*, vol. 3, p. S08002, 2008.

[54] B. B. Abelev *et al.*, "Performance of the ALICE Experiment at the CERN LHC," *Int. J. Mod. Phys. A*, vol. 29, p. 1430044, 2014.

[55] B. Abelev *et al.*, "Technical Design Report for the Upgrade of the ALICE Inner Tracking System," *J. Phys. G*, vol. 41, p. 087002, 2014.

[56] C. Lippmann, "Upgrade of the ALICE Time Projection Chamber," *CERN-LHCC-2013-020, ALICE-TDR-016*, 3 2014.

[57] E. Garcia-Solis, "The Fast Interaction Trigger Upgrade for ALICE," *PoS*, vol. ICHEP2016, p. 241, 2016.

[58] C. Lippmann, "Particle identification," *Nucl. Instrum. Meth. A*, vol. 666, pp. 148–172, 2012.

[59] P. Buncic, M. Krzewicki, and P. Vande Vyvre, "Technical Design Report for the Upgrade of the Online-Offline Computing System," *CERN-LHCC-2015-006, ALICE-TDR-019*, 4 2015.

[60] M. Krzewicki and V. Lindenstruth, "ALICE HLT Run 2 performance overview," *J. Phys. Conf. Ser.*, vol. 898, no. 3, p. 032056, 2017.

[61] M. Al-Turany, D. Bertini, R. Karabowicz, D. Kresan, P. Malzacher, T. Stockmanns, and F. Uhlig, "The FairRoot framework," *J. Phys. Conf. Ser.*, vol. 396, p. 022001, 2012.

[62] A. Arrow, "A cross-language development platform for in-memory analytics," 2021, last accessed 3 May 2023. [Online]. Available: https://arrow.apache.org/

[63] R. Brun and F. Rademakers, "ROOT: An object oriented data analysis framework," *Nucl. Instrum. Meth. A*, vol. 389, pp. 81–86, 1997.

[64] A. Alkin, G. Eulisse, J. F. Grosse-Oetringhaus, P. Hristov, and M. Kabus, "ALICE Run 3 Analysis Framework," *EPJ Web Conf.*, vol. 251, p. 03063, 2021.

[65] A. collaboration, "Aliphysics," last accessed 3 May 2023. [Online]. Available: https://github.com/alisw/AliPhysics

[66] D. D. Chinellato, "Introduction to framework," 2023, last accessed 15 May 2023. [Online]. Available: https://indico.cern.ch/event/1267433/contributions/5359448/attachments/2634427/4557168/DDChinellato-Tutorial-Introduction-04.pdf

[67] A. D. P. Group, "Run 3 a brave new world," 2023, last accessed 15 May 2023. [Online]. Available: https://indico.cern.ch/event/1267433/contributions/5359449/attachments/2634428/4557169/DDChinellato-Tutorial-Run3-01.pdf

[68] M. Kabus, "A novel algorithm of event mixing for alice run 3," 2023, last accessed 15 May 2023. [Online]. Available: https://indico.cern.ch/event/895086/contributions/4723734/attachments/2420447/4142924/2022-03-29-Quark\20Matter\20Maja\20Kabus.pdf

[69] D. A. Romanov, "Crystal ball function," 2009, last accessed 23 May 2023. [Online]. Available: https://www.jlab.org/primex/weekly_meetings/slides_2009_07_17/dmitry/crystalball.html

[70] S. Gorbunov *et al.*, "Deep neural network techniques in the calibration of space-charge distortion fluctuations for the ALICE TPC," *EPJ Web Conf.*, vol. 251, p. 03020, 2021.

[71] Z. Citron *et al.*, "Report from Working Group 5: Future physics opportunities for high-density QCD at the LHC with heavy-ion and proton beams," *CERN Yellow Rep. Monogr.*, vol. 7, pp. 1159–1410, 2019.

[72] "Future high-energy pp programme with ALICE," 2020.